

NASA _____
NASA CR- 105666

PSI-2093/TR-1143

AEROTHERMODYNAMIC RADIATION STUDIES

Contract No. NAS9-18172

Prepared by:

K. Donohue, W.G. Reinecke, D. Rossi, W.J. Marinelli, R.H. Krech and G.E. Caledonia
Physical Sciences, Inc.
20 New England Business Center
Andover, MA 01810

Final Report

Prepared for:

Lyndon B. Johnson Space Center
Space & Life Sciences Procurement Branch
Houston, TX 77058

September 1991

PHYSICAL SCIENCES INC.

20 New England Business Center, Andover, MA 01810, U.S.A.



181-1700

Handwritten notes and signatures at the bottom of the page.

Handwritten text at the bottom right corner.

FIGURES

<u>Figure No.</u>		<u>Page</u>
1	Aerothermal shock tube schematic	5
2	Arc driver overview	6
3	Detail of NASA Ames arc driver	6
4	Layout of arc driver in shock tube laboratory.	7
5	Side view sketch of arc driver, capacitor bank, and cart	8
6	Power system layout	8
7	Capacitor bank control panel	9
8	Capacitor bank	10
9	OMA/monochromator configuration	12
10	$N_2(B)$ radiometer vibrational temperature sensitivity	13
11	$N_2^+(B)$ radiometer vibrational temperature sensitivity	13
12	$N_2^+(B)$ rotational temperature measurement ratio: 467.5 nm/470. nm at bandpass	14
13	Radiometer configuration	16
14	Radiometer calibration setup	17
15	871.4 nm radiometer-calibration factor vs PMT voltage	21
16	645 nm radiometer-calibration factor vs PMT voltage	21
17	470.5 nm radiometer-calibration factor vs PMT voltage	22
18	469.0 nm radiometer-calibration factor vs PMT voltage	22
19	467.5 nm radiometer-calibration factor vs PMT voltage	23
20	454.6 nm radiometer-calibration factor vs PMT voltage	23
21	Experimental configuration for OMA calibration	24
22	Relative calibration broad band OMA	27
23	Relative calibration narrowband OMA.	27
24	Calibration spectrum narrow band OMA31	
25	Pure N_2 equilibrium temperature behind a normal shock vs shock velocity	32
26	Pure N_2 equilibrium density	33
27	Pure N_2 equilibrium species concentration vs shock velocity, $P=0.1$ torr	34
28	Pure N_2 equilibrium species concentration vs shock velocity, $P=1$ torr	35

FIGURES (Continued)

<u>Figure No.</u>	<u>Page</u>
29	Pure N ₂ equilibrium species concentration vs shock velocity, P=10 torr 36
30	Equilibrium air temperature vs shock velocity 37
31	Equilibrium air temperature vs shock velocity 38
32	Equilibrium air species vs shock velocity 39
33	Equilibrium air species vs shock velocity, P=1 torr 40
34	Equilibrium air species vs shock velocity, P=10 torr 41
35	Radiometers signal vs time for the 391.4 and 645 bands 43
36	Radiometers signal vs time for the 391.4 and 645 bands 43
37	Radiometers signal vs time for the 391.4 and 645 bands 44
38	Observed values of t_p and $t_{0.1}$ from the present measurements contrasted with the earlier AERI data 46
39	Case A shock data and spectral fit 47
40	Case B shock data and spectral fit 48
41	Case C shock data and spectral fit 48
42	Case D shock data and spectral fit 49
43	Case E shock data and spectral fit 50
44	Case F shock data and spectral fit 50

TABLES

<u>Table No.</u>		<u>Page</u>
1	Calculated Shock Tube Performance	11
2	Radiometer Calibration Specifications	17
3	Calibrated Data for Radiometer 1	18
4	Calibrated Data for Radiometer 2	18
5	Calibrated Data for Radiometer 3	19
6	Calibrated Data for Radiometer 4	19
7	Calibrated Data for Radiometer 5	20
8	Calibrated Data for Radiometer 6	20
9	OMA Diagnostic Specifications	24
10	Adjusted Irradiance Values	26
11	Summary of Shock Test Conditions	33
12	Ratio of Peak Non-equilibrium to Equilibrium Intensities	44
13	Relative Intensities I_p , I_e at 645 nm vs Velocity	45

PROJECT SUMMARY

We have built and made operational a 6 in. electric arc driven shock tube which allows us to study the non-equilibrium radiation and kinetics of low pressure (0.1 to 1 torr) gasses processed by 6 to 12 km/s shock waves. The diagnostic system allows simultaneous monitoring of shock radiation temporal histories by a bank of up to six radiometers, and spectral histories with two optical multi-channel analyzers.

A data set of eight shots was assembled, comprising shocks in N_2 and air at pressures between 0.1 and 1 torr and velocities of 6 to 12 km/s. Spectrally resolved data was taken in both the non-equilibrium and equilibrium shock regions on all shots. The present data appear to be the first spectrally resolved shock radiation measurements in N_2 performed at 12 km/s. The data base has been partially analyzed with salient features identified.

1. INTRODUCTION

The purpose of this project was to build an electric arc driven shock tube to be used to develop a data base for the non-equilibrium radiation signatures of low pressure air shock-heated to velocities of 6 to 12 km/s. The concept was to provide a marriage between the shock tube technology of the 1960's-1970's and state-of-the-art optical diagnostics, such as optical multi-channel analyzers (OMA's), to provide a quantum jump in the quality of the radiation signature base for shock heated air. This data base is critical for the validation of computer models used to predict radiational levels behind high altitude hypersonic bow shocks.

Up until very recently the only source of measurements of non-equilibrium radiation signatures behind 6 to 12 km/s air shocks at low pressure was that developed at the AVCO Everett Research Laboratory (AERL) in the early 1960's¹⁻⁴. These seminal experiments were performed using filtered radiometers which unfortunately introduced uncertainties in the data interpretation because of the unknown impact of contaminants. In 1988 PSI demonstrated that OMA's could be used in the laboratory to provide spectrally resolved signatures over narrow time gates behind incident shocks⁵. These measurements were performed for a shock speed of 4 km/sec and an ambient pressure of 1 torr in N₂. Since that time the NASA Ames group has published detailed spectral measurements (using an OMA) for non-equilibrium radiation at two shock conditions: 6.4 km/s in one torr N₂⁶ and 10 km/s in 0.1 torr air⁷. Although the spectra in this work was similar to the AERL observations, the characteristic temperatures, i.e., vibrational and rotational, deduced from a spectral analysis of the data is quite different from that determined in the earlier work. To the best of the authors knowledge, the data presented in this report are the only other modern measurements available on shock velocities above 5 km/s.

We provide a detailed description of our 6 in. electric arc driven shock tube in the next section. This includes the details of the diagnostics and the calibration. The protocol for the testing out of this new shock tube system is provided in Appendix A. The new data base and respective analysis is presented in Section 3. Unfortunately, given the lengthy development time for the shock tube, the data base is limited. It is composed of shakedown measurements which suggested improvements in the diagnostics. Nonetheless some useful information is provided.

The report summary is provided in Section 4.

2. FACILITY DESCRIPTION

2.1 Shock Tube Facility

The Aerothermal Radiation shock tube facility is composed of a 6-in. ID shock tube which can be driven by either a pressure driver or an electric arc driver. The pressure driver, using hydrogen as the driver gas results in shock speeds of ≤ 4 km/s. This facilitated initial testing of the tube and optical diagnostics. Higher speeds were achieved using the arc driver.

Figure 1 is a schematic of the shock tube facility with the pressure driver. The optical diagnostics are omitted here for simplicity. The tube is pumped out via a pumping manifold consisting of a 2-in. diffusion pump (Varian) and a mechanical pump (Alcatel 2033) which acts as a fore pump for the diffusion pump as well as the roughing pump for the tube. Ultimate vacuum levels in the tube were 2×10^{-6} torr; measured with an ion gauge (Granville Phillips). Test gas fill pressures were measured with a Convector gauge situated slightly upstream of the test section. The pressure driver was evacuated with a mechanical pump and filled with hydrogen from a remote filling station. Fill pressures, typically 1500 psig were monitored using a Matheson test gauge.

2.2 Electric Arc Driver

PSI designed and fabricated an arc driver to increase significantly the performance of our 6-in. shock tube. To minimize both the risk and cost, the driver is patterned after the arc driver operating at the NASA Ames Research Center and described in Refs. 8 through 11. The Ames driver described in these references is shown schematically in Figures 2 and 3.

We made certain changes to the driver components to bring it up to more modern mechanical design practice (the original design dates from the 1960's) and to simplify it, but the basic design concept was retained. The tube is driven by a bank of twelve $50 \mu\text{F}$ capacitors

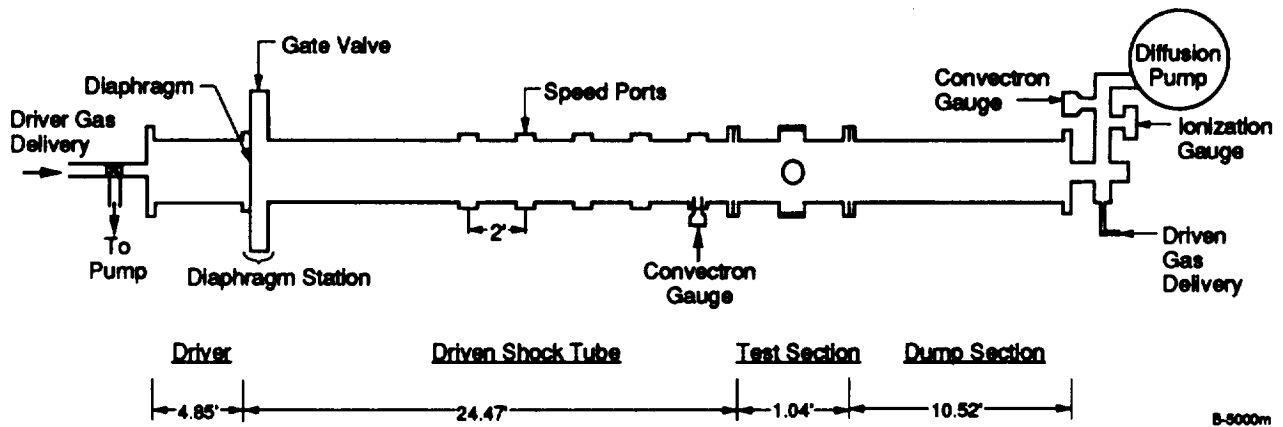
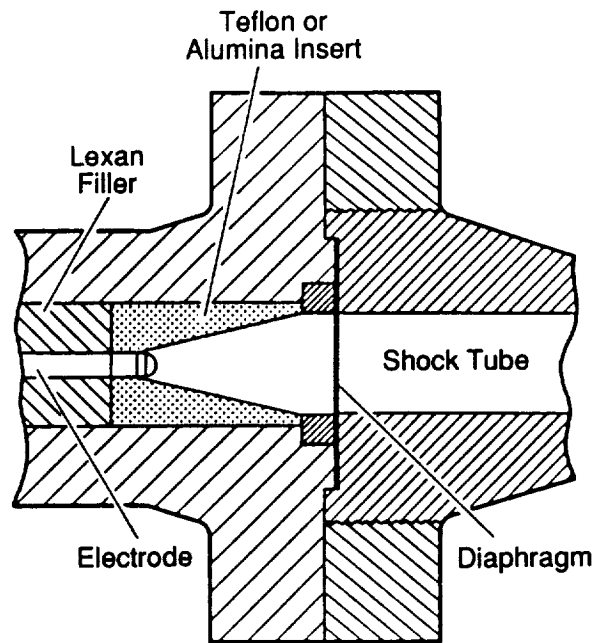


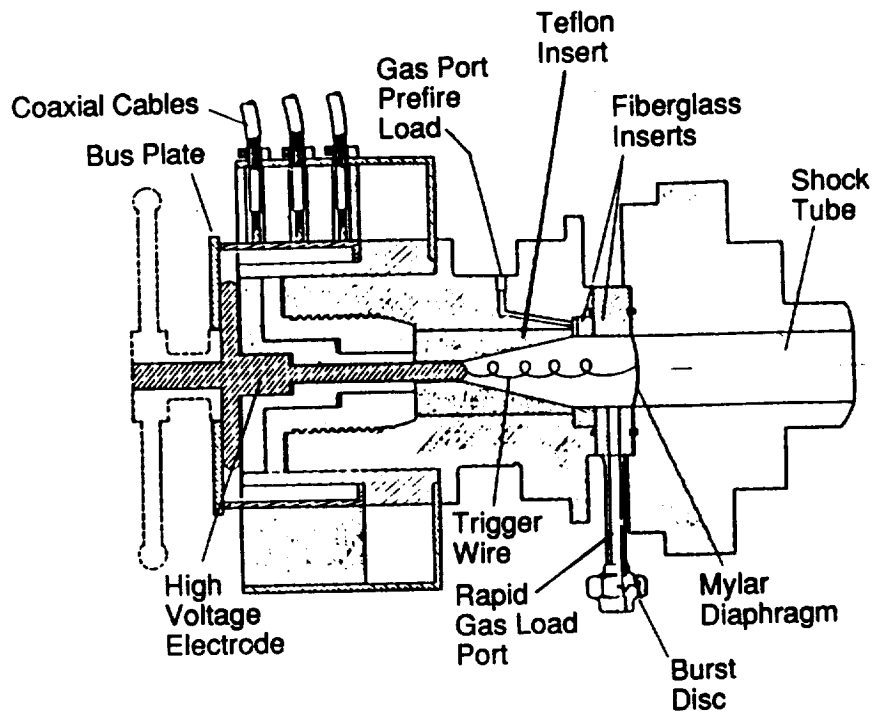
Figure 1. - Aerothermal shock tube schematic.



Dannenberg, AIAA, 10, 1972, 1692-94

A-9041

Figure 2. - Arc driver overview.



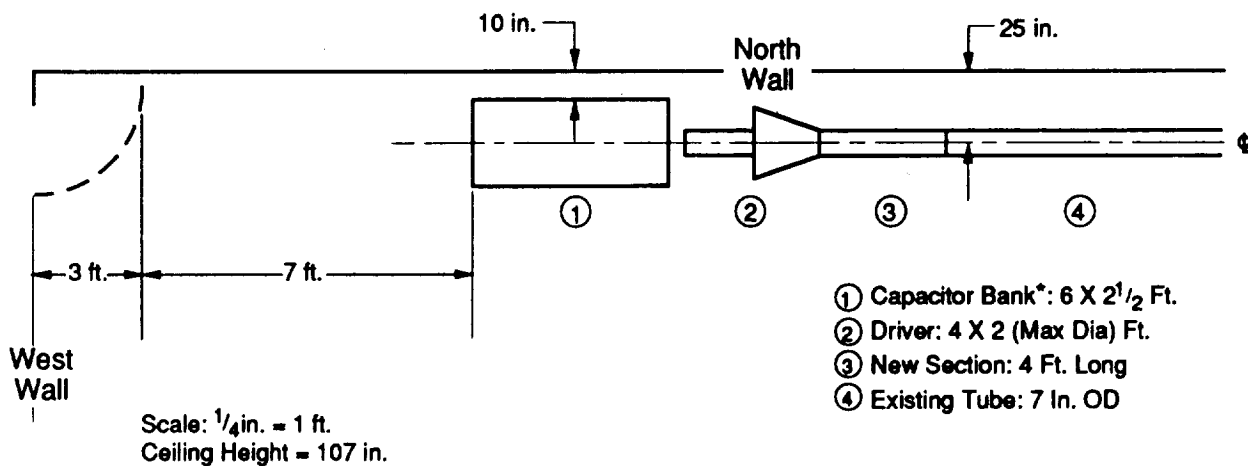
A-9042

Figure 3. - Detail of NASA Ames arc driver (Dannenberg and Slapnicar, AIAA, 14, 1976, 1183-88.

charged to a maximum of 20 kV, yielding a maximum stored energy of 120 kJ. The general layout of the arc driver in the PSI Shock Tube Laboratory is shown in Figure 4. The capacitors are mounted rigidly to the driver on a moveable carriage to allow the driver to be opened. Mounting the capacitors on the carriage does away with the complexity, cost, and impedance of flexible cables. The driver frame and capacitors are shown in Figure 5. The carriage uses steel wheels running in steel tracks. The power supply system is shown in Figures 6, 7, and 8. The detailed testing procedure for these components is contained in Appendix A.

We made a preliminary performance calculation for the driver assuming that 100 kJ of energy are delivered to 12 atm of room temperature helium driver gas at constant volume. The constant volume heating of the helium results in driver conditions of 17,500 K and 700 atm and a diaphragm pressure ratio of 53,200. PSI's shock tube code "SHOCK PSI" was used to calculate the resulting shock wave for initial pressures of 0.1, 1 of nitrogen. The calculated equilibrium nitrogen conditions behind the shock are shown in Table 1. The mixture is dominated by neutral and singly ionized nitrogen atoms and electrons.

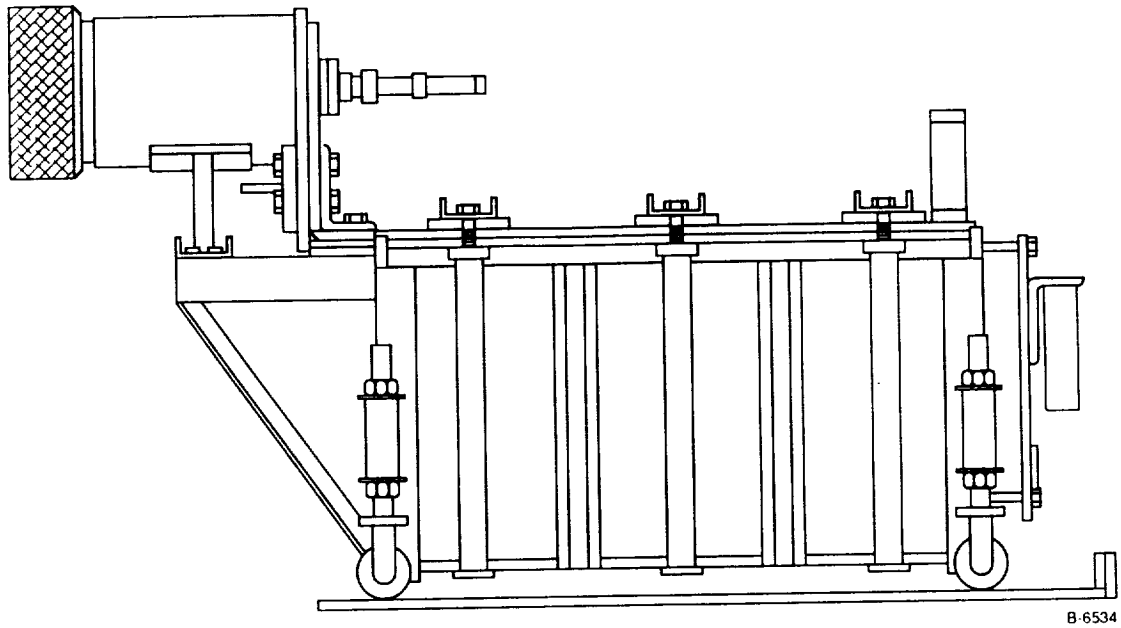
The arrangement of the monochromators with respect to the tube is shown in Figure 9. The monochromators view the same point in the shock front from ports located on opposing sides of the shock tube. Imaging optics are provided to map the field of view on to the f/5.4 optics of the monochromators. Sharma and Gillespie⁶ were required to use 200 ns gating times on their OMA system in order to obtain adequate signal levels. This system provides a single, somewhat temporally blurred picture of the emission signatures. To enhance our ability to measure the time history of the emission signals we have provided some high speed radiometers. These are described in the next section.



*Capacitors Are Standing Upright In 4 X 3 Or 6 X 2 Array
On Trolley Rigidly Attached To Driver

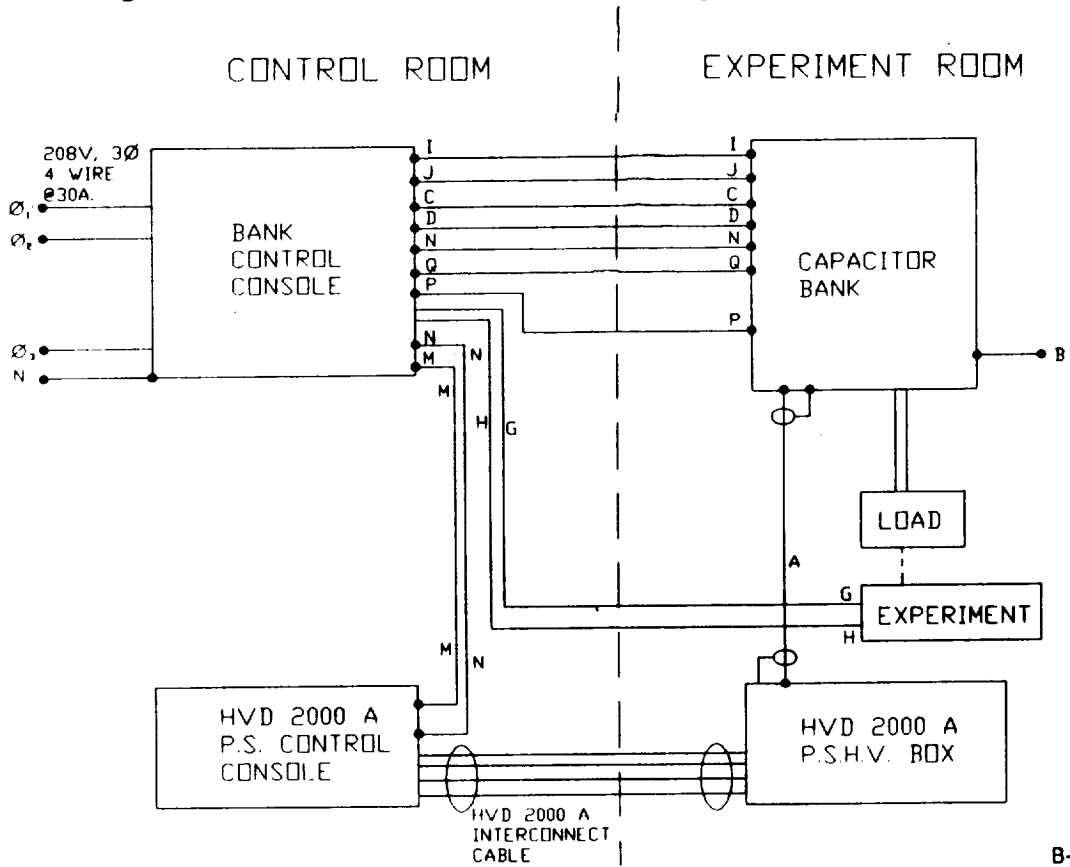
B-5787

Figure 4. - Layout of arc driver in shock tube laboratory.



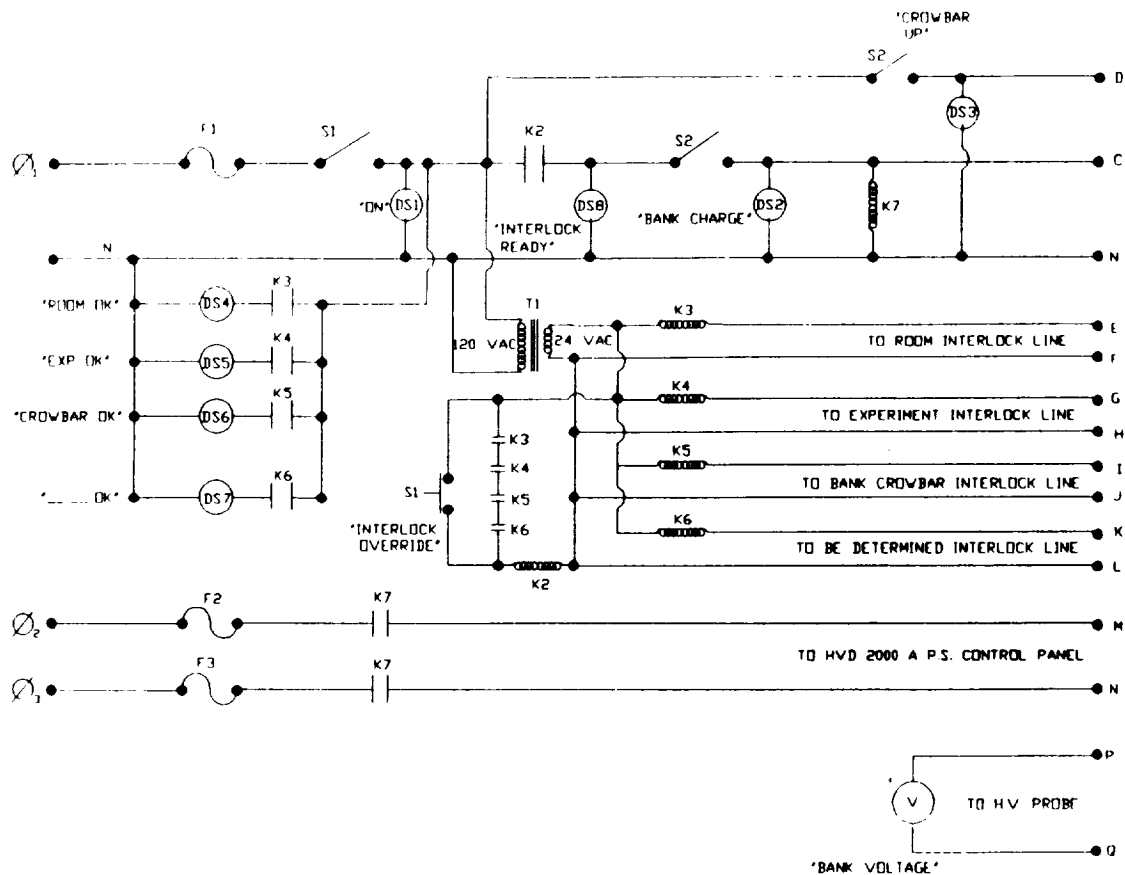
B-6534

Figure 5. - Side view sketch of arc driver, capacitor bank, and cart.



B-6535

Figure 6. - Power system layout.



B-6536

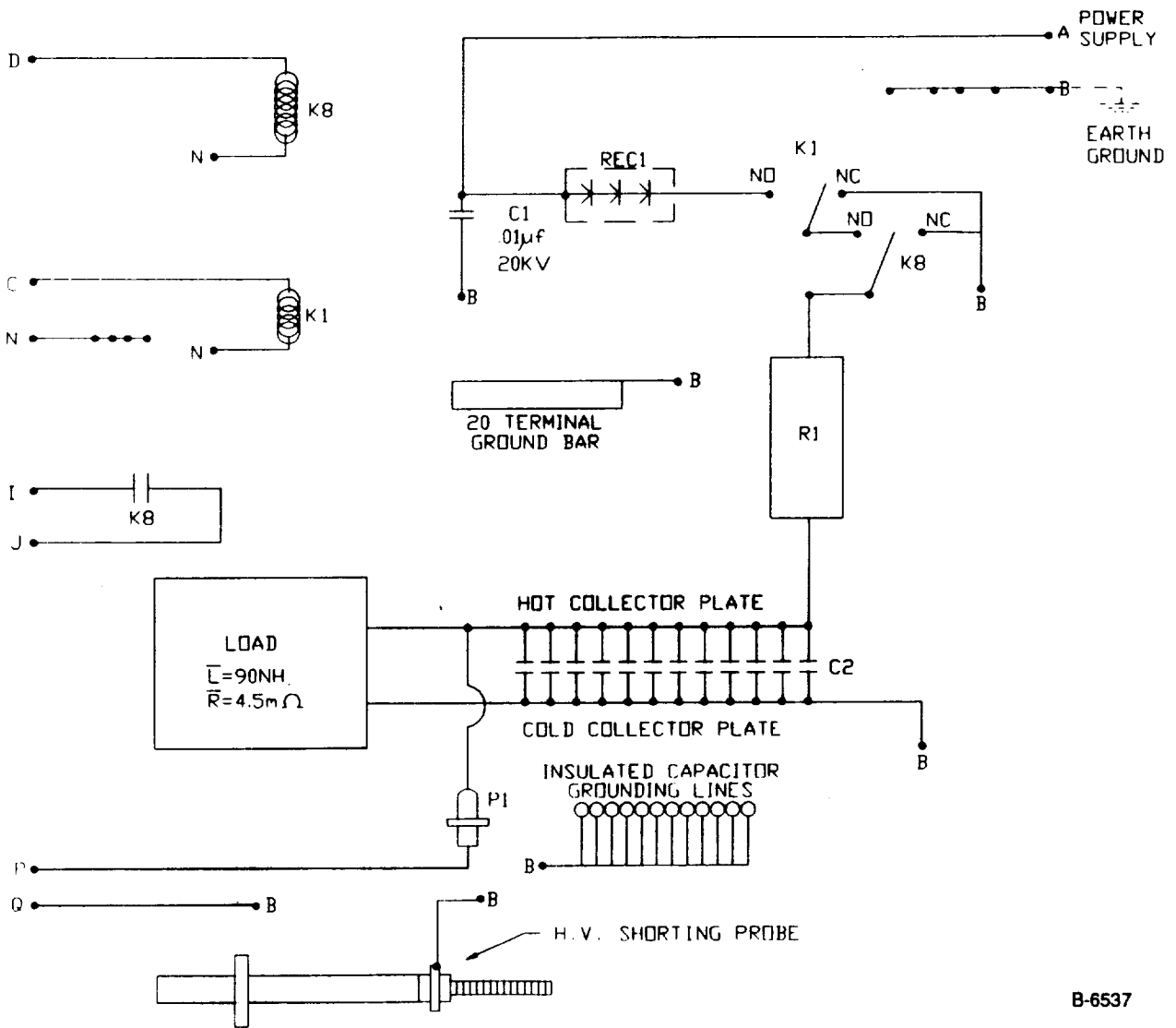
Figure 7. - Capacitor bank control panel.

2.3 Optical Diagnostics

In this section we discuss the configuration of the shock tube optical diagnostics. The diagnostics are divided into three distinct subsystems: passive resolved emission measurements using monochromators and optical multichannel analyzers (OMA), time-resolved radiometric measurements of emission in bandpasses selected to provide information about specific vibration-rotation states of key electronic emitters, and Raman spectroscopic measurements of ground state vibrational distributions. The configuration of the monochromator/OMA and radiometer systems will be discussed below.

2.4 Resolved Emission Measurements

Resolved emission in the region from 200 to 800 nm is detected using two identical monochromator/OMA systems. The system is comprised of two image-intensified optical multichannel analyzers (Princeton Instruments Model IRY-700G/RB) capable of being gated to times as short as 10 ns. The OMA systems are interfaced to two 0.32m monochromators/spectrographs (Instruments SA Model HR-320). A single computer controlled interface allows the OMA systems to be triggered simultaneously or independently, as required.



B-6537

Figure 8. - Capacitor bank.

TABLE 1. CALCULATED SHOCK TUBE PERFORMANCE: INITIAL PRESSURE, 1 torr

TABLE 1a. CALCULATED SHOCK TUBE PERFORMANCE: INITIAL PRESSURE, 1 TORR

	T(K)	P(atm)	ρ (g/cc)	H(erg/g)	Z(mole)	US,USR(cm/s)	U2,U3(cm/s)	PD(atm)
	2.700E+04	6.283E+00	2.434E-05	2.259E+12	3.265E+00	2.128E+06	1.997E+06	6.989E+02
MOL	N2 2.611E-06	N 8.550E-01	N + 1.025E+00	N + + 1.19tE-01	N + + + 1.036E-06	N2 + 2.221E-06	E 1.265E+02	
M.F.	7.999E-07	2.619E-01	3.141E-01	3.664E-02	3.173E-07	6.802E-07	3.874E-01	
AMA	5.058E-08	1.665E-02	1.997E-02	2.329E-03	2.017E-08	4.324E-08	2.462E-02	

TABLE 1b. CALCULATED SHOCK TUBE PERFORMANCE: INITIAL PRESSURE, 0.1 TORR

	T(K)	P(atm)	ρ (g/cc)	H(erg/g)	Z(mole)	US,USR(cm/s)	U2,U3(cm/s)	PD(atm)
	2.888E+04	9.740E-01	2.349E-06	3.508E+12	4.901+00	2.653E+06	2.484E+06	7001E+02
MOL	N2 2.663E-08	N 2.293E-01	N + 6.401E-01	N + + 1.130E+00	N + + + 1.898E-04	N2 + 3.898E-08	E 2.901E+00	
M.F.	5.433E-09	4.679E-02	1.306E-01	2.306E-01	3.872E-05	7.952E-09	5.920E-01	
AMA	5.005E-11	4.310E-04	1.203E-03	2.125E-03	3.567E-07	7.326E-11	5.454E-03	

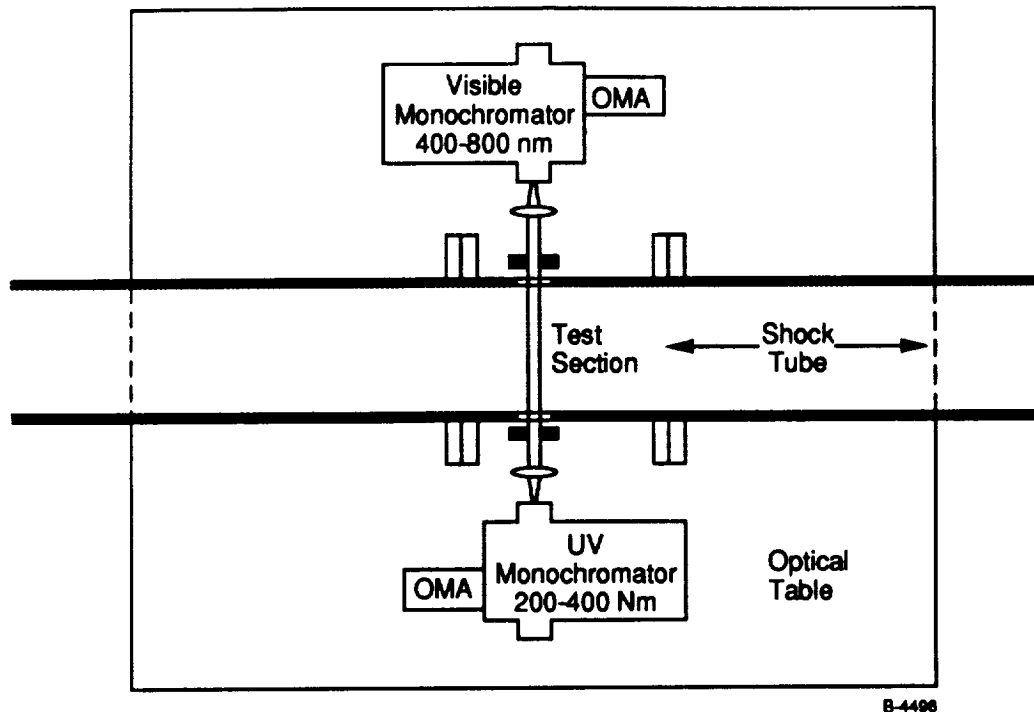


Figure 9. - OMA/monochromator configuration.

The two systems are used to determine emission levels in the regions 300 to 800 nm, respectively, through the use of appropriate order-sorting filters. Gratings have been specified for the monochromators which will disperse these entire wavelength regions on to the active region of the OMA detectors.

2.5 Radiometer System

The radiometer system is designed to follow the temporal history of the vibrational and rotational temperatures of selected N_2 electronic states throughout the non-equilibrium and equilibrium stage of the shock. The vibrational temperatures are determined from the ratio of the populations in different vibrational levels of the same excited state: where $E_{v'-v''}$ is the difference in energy between vibrational levels v' and v'' . We have selected vibronic

$$\frac{[N_{v'}]}{[N_{v''}]} = e^{\frac{-(E_{v'} - E_{v''})}{kT}} \quad (1)$$

bands to measure the vibrational temperature of the $N_2(B^3\pi_g)$ state via the B-A transition, and the $N_2^+(B^2\Sigma)$ state via the B-X transition. The ratio of the $N_2(B-A)$ 2-1 to 8-5 transitions used to measure the B-state temperature. Figure 10 shows how the intensity ratio for these bands varies with vibrational temperature. The $N_2^+(B-X)$ 0-2 and 3-5 transitions are used to determine the N_2^+ B-state temperature. This sensitivity with temperature is shown in Figure 11. These bands have been chosen to have maximum sensitivity to

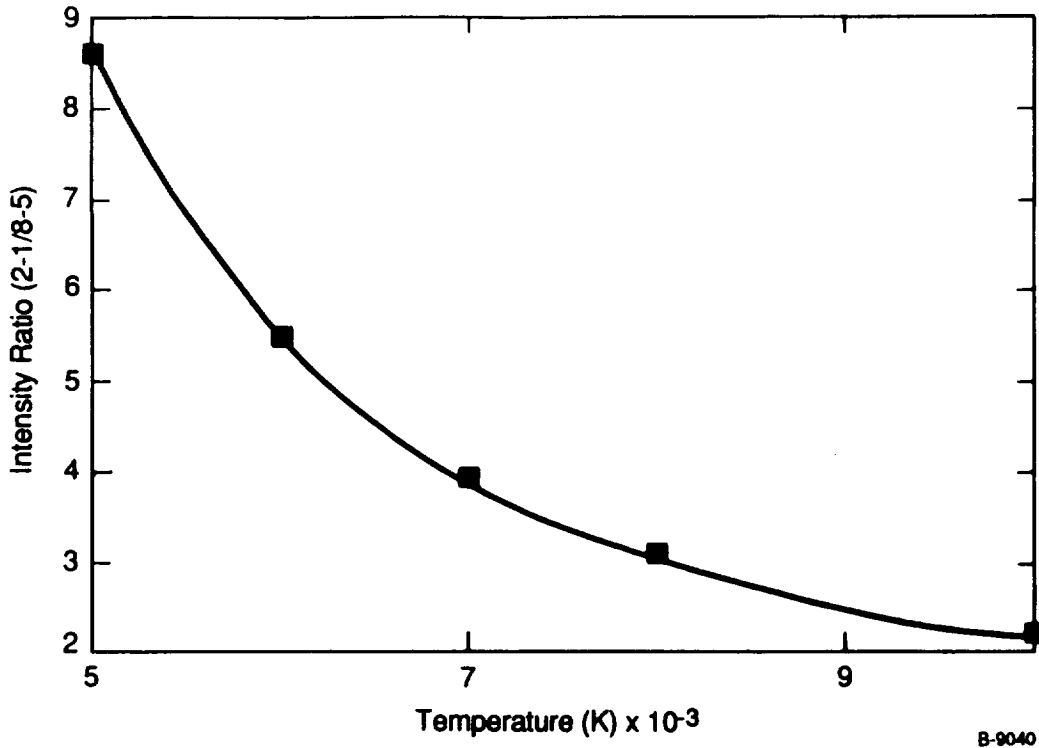


Figure 10. - N₂(B) radiometer vibrational temperature sensitivity.

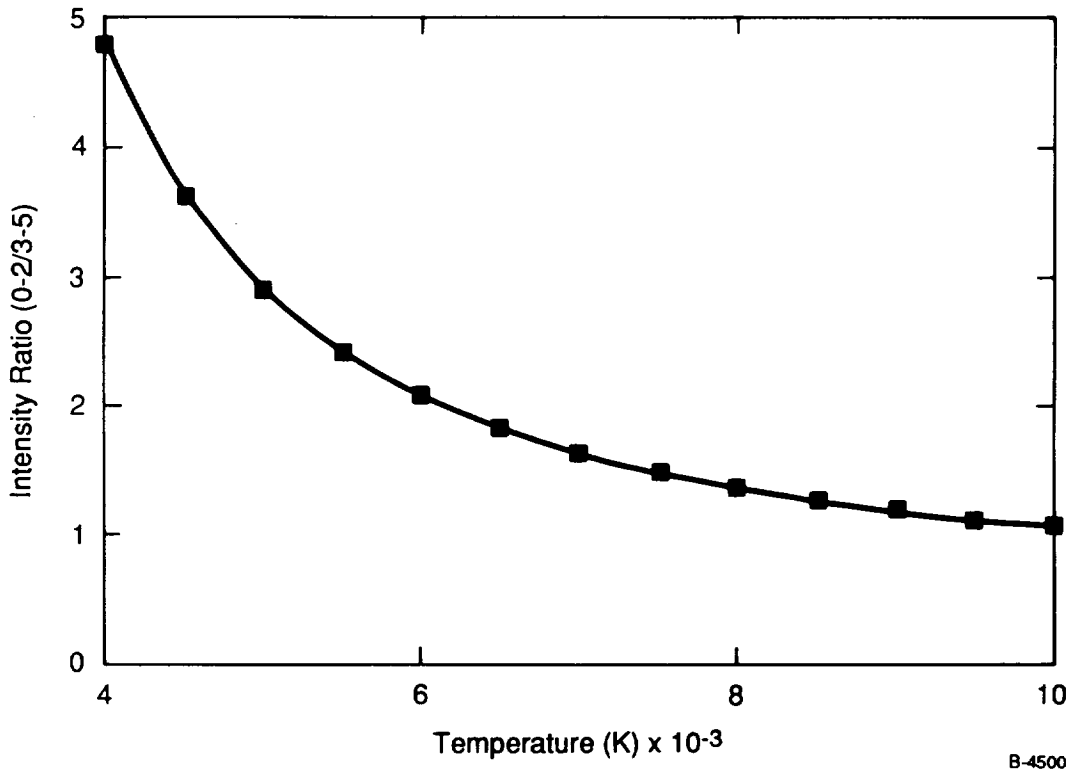


Figure 11. - N₂⁺(B) radiometer vibrational temperature sensitivity.

temperature changes in the region near 7000 K. They also should not be subject to interferences from other N_2 transitions and especially CN(B-X) and CN(A-X) impurity emissions.

The rotational temperature is measured by observing the intensity of a band head and band tail in the N_2^+ (B-X) 0-2 transition. Figure 12 shows how the ratio of intensities of the band head (470.5 nm, 1 nm FWHM) to tail (467.5 nm, 1 nm FWHM) scales with rotational temperature. These bandpasses are free of interferences from CN(B-X) emission and other N_2 bands.

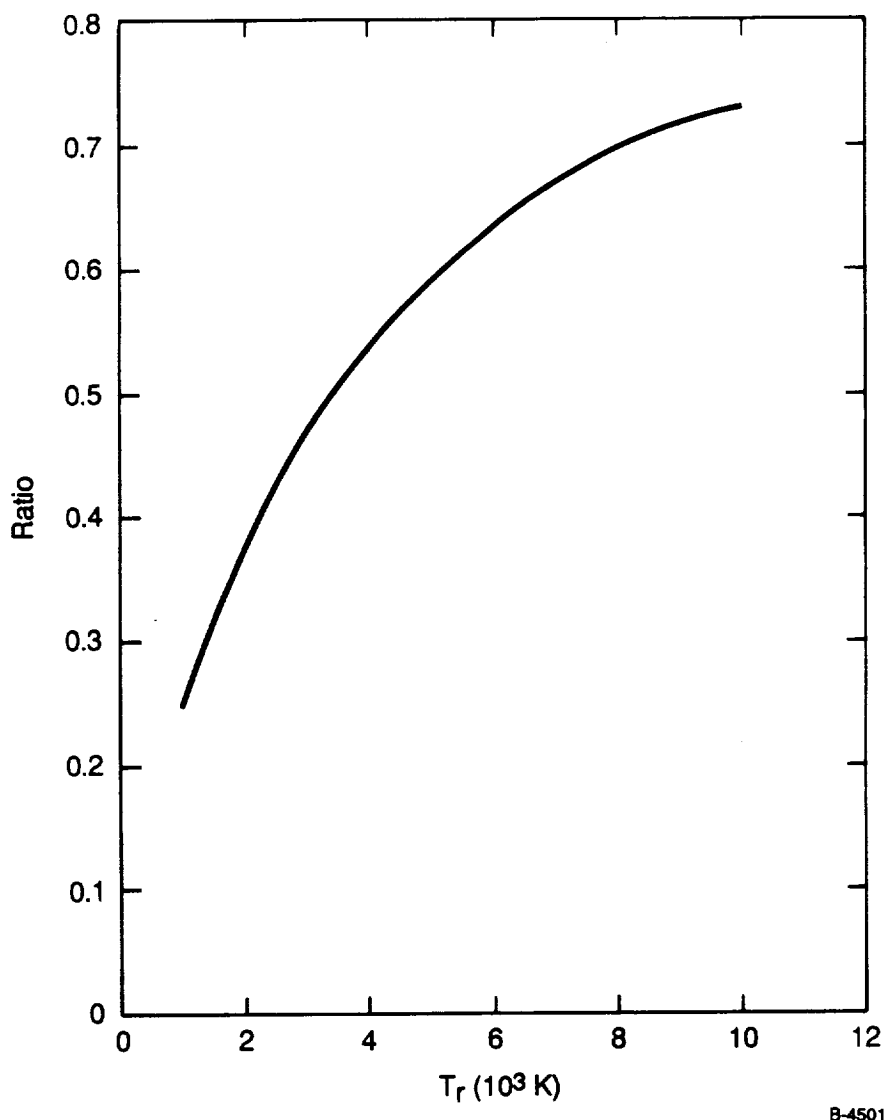


Figure 12. - N_2^+ (B) rotational temperature measurement ratio: 467.5 nm/470. nm at bandpass.

The configuration of the radiometer system is shown in Figure 13. A unique feature of the diagnostic configuration is the use of a six-way fiberoptic splitter to distribute light to the various radiometer detectors. This system allows the same point in space to be viewed by all of the radiometers simultaneously with the use of only one port in the shock tube. Calibration of the radiometers is simple, since a calibration standard can be placed at the opposite window of the tube and signals from each channel can be recorded simultaneously.

An array of six computer controlled high speed (20 MHz) transient digitizers fed by 12 MHz amplifiers is used to record the signals from the six photomultiplier tubes used in the radiometers. The temporal resolution of the radiometers is determined by the projection of their field of view into the center of the shock tube. A 1 mm wide field is required to obtain adequate signal levels. At shock speeds of 10 km s^{-1} ($10 \text{ mm}/\mu\text{s}$) the ultimate temporal resolution is approximately $0.1 \mu\text{s}$. The detection electronics are specified to be consistent with this temporal resolution. Optical diagnostics were calibrated to allow data reduction in absolute units. This section contains the details of these calibration procedures and resultant calibration factors.

2.6 Radiometer Calibration Procedure

The six radiometers have been absolutely calibrated with a quartz halogen irradiance standard (Optronics 245-C). Figure 14 depicts the calibration configuration. The quartz halogen lamp is placed at a distance, r , from the slit defining aperture in the bottom window of the test section. The standard lamp irradiates an area with a known power density at a given distance. These reported values of spectral irradiance in units of microwatts $\text{cm}^{-2} \text{ nm}^{-1}$ are given for the lamp at $r = 50 \text{ cm}$. the irradiance is proportional to $1/r^2$, so irradiance can be calculated at any known distance.

In the calibration experiment, the slit is irradiated and signals from the radiometers are recorded on the eight-channel digital storage oscilloscope acquisition system. The measured voltage is converted to the photomultiplier tube anode current based on input impedance to the amplifiers and signal amplification. Each radiometer's signal is related to the absolute irradiance via a calibration factor which is the ratio of the power through the slit to PMT output. Specifically, the calibration factors, F , are calculated as follows:

$$F = \frac{(\text{irradiance}(\mu\text{Wcm}^{-2}\text{nm}^{-1})(\text{spectral bandwidth (nm)})(\text{slit area (cm}^2)))(T)}{\text{anode current}}$$

where T equals a transmission factor of 0.92 which accounts for the lamp's power loss through the top window of the test section.

Table 2 compiles the values needed in calculation of the power throughput each radiometer will detect. Calibration factors for each radiometer were determined versus PMT voltage (Tables 3 through 8). Figures 15 through 20 are plots of these calibration factors versus PMT voltage.

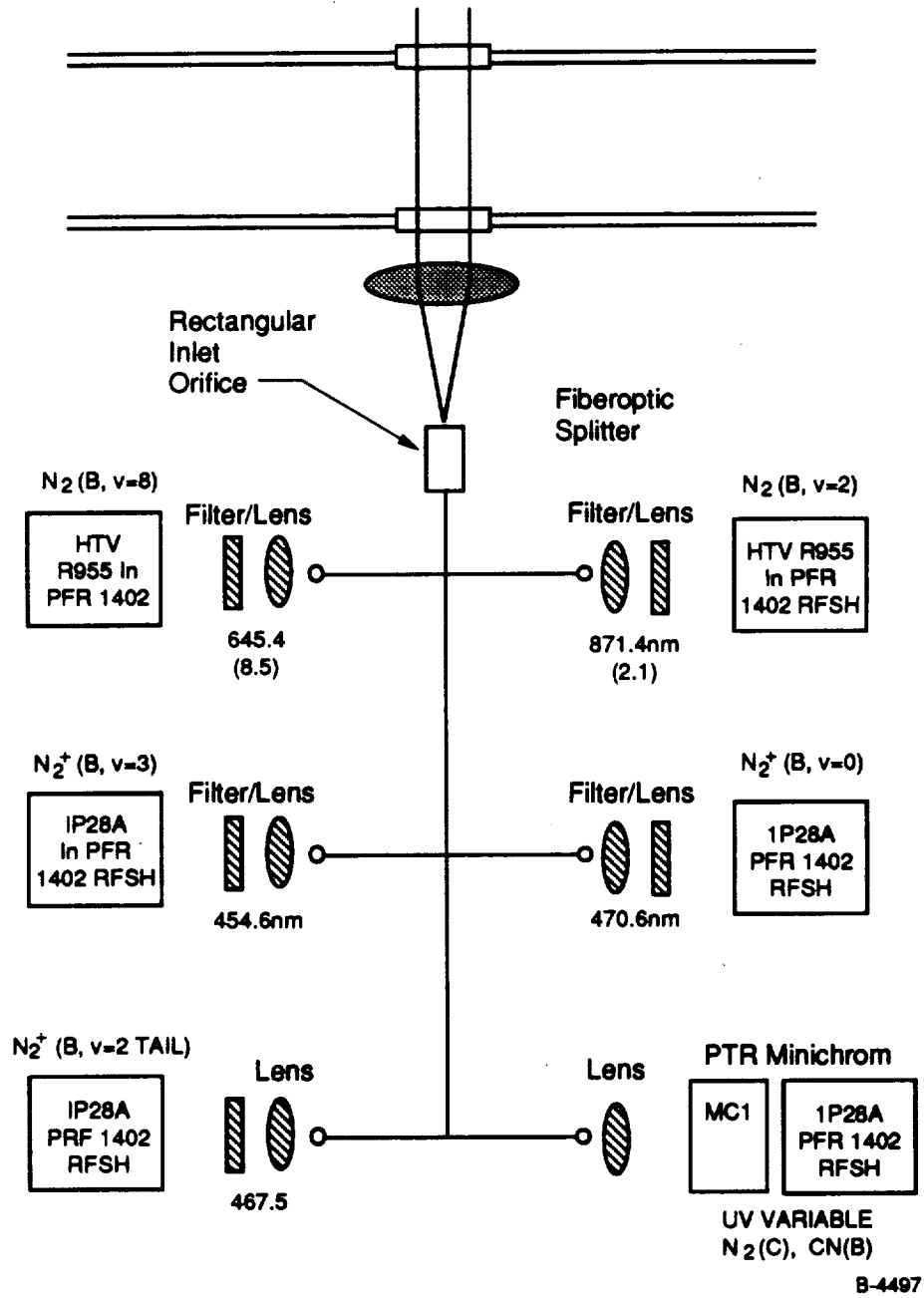
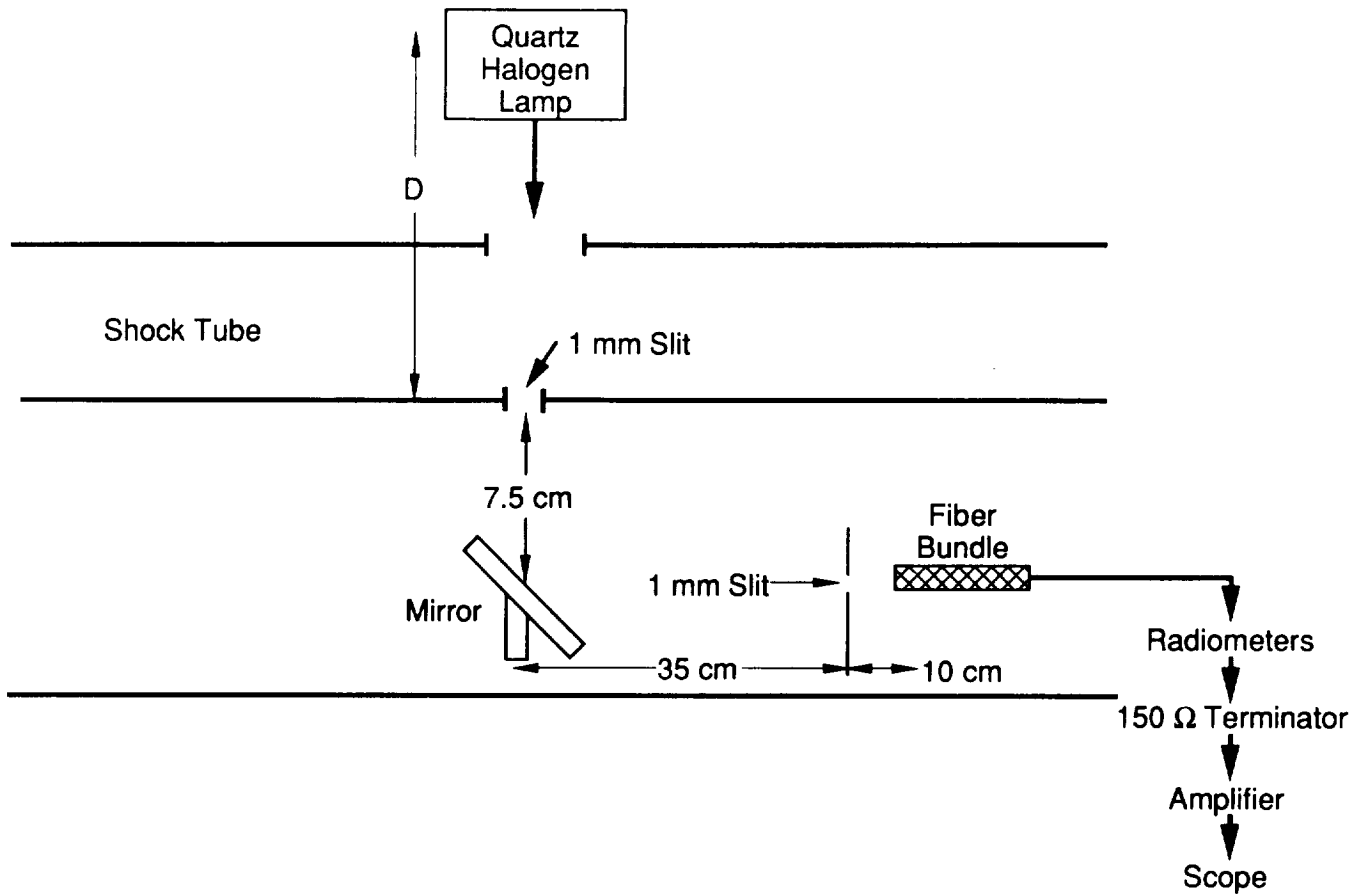


Figure 13. - Radiometer configuration.



B-6684

Figure 14. - Radiometer calibration setup.

TABLE 2. RADIOMETER CALIBRATION SPECIFICATIONS

Radiometer	Serial Number	Filter Wavelength (nm)	Filter Bandwidth (nm)	Reported Irradiance at 50 cm ($\mu\text{w}/\text{cm}^2/\text{nm}$)	Distance r (cm)	Slit Area (cm^2)	Detected Power Through Slit (μw)
1	16914-90-4	871.4	9.4	0.971	61.25	0.25	1.713
2	16914-90-1	645	2.73	0.56	61.25	0.25	0.2994
3	16914-90-5	470.5	1.159	0.20	47.5	0.25	0.0641
4	16914-90-6	469.0	3.05	0.1969	47.5	0.25	0.1663
5	16914-90-3	467.5	0.933	0.1934	47.5	0.25	0.0494
6	16914-90-2	454.6	0.839	0.1621	47.5	0.25	0.0375

TABLE 3. CALIBRATION DATA FOR RADIOMETER 1;
SERIAL #16914-90-4; FILTER $\lambda=871.4$ NM

PMT (volts)	Current (amps)	$\mu\omega/\text{amp}$	Photons $\text{s}^{-1} \text{A}^{-1}$
400	3.02E-08	5.67E+06	2.2E+20
500	1.81E-07	9.45E+06	3.7E+19
600	7.55E-07	2.27E+06	8.8E+18
700	3.43E-06	4.99E+05	1.9E+18
800	5.50E-06	3.11E+05	1.2E+18
900	1.38E-05	1.24E+05	4.8E+17

TABLE 4. CALIBRATION DATA FOR RADIOMETER 2; SERIAL #16914-1;
FILTER $\lambda=645$ NM

PMT (volts)	Current (amps)	$\mu\omega/\text{amp}$	Photons $\text{s}^{-1} \text{A}^{-1}$
400	3.33×10^{-7}	8.26×10^5	2.68×10^{18}
500	1.67×10^{-6}	1.65×10^5	5.36×10^{17}
600	6.67×10^{-6}	4.13×10^4	1.34×10^{17}
700	2.08×10^{-5}	1.32×10^4	4.29×10^{16}
800	5.00×10^{-5}	5.51×10^3	1.79×10^{16}
900	1.50×10^{-4}	1.84×10^3	5.96×10^{15}
1000	2.92×10^{-4}	1.49×10^2	4.04×10^{14}

TABLE 5. CALIBRATION DATA FOR RADIOMETER 3; SERIAL #16914-90-5;
 FILTER $\lambda=470.5$ NM

PMT (volts)	Current (amps)	$\mu\omega/\text{amp}$	Photons $\text{s}^{-1} \text{A}^{-1}$
500	2.08×10^{-7}	2.83×10^5	6.70×10^{17}
550	8.19×10^{-7}	4.20×10^4	1.7×10^{17}
600	1.26×10^{-6}	4.67×10^4	1.1×10^{17}
650	2.32×10^{-6}	2.54×10^4	6.02×10^{16}
700	5.04×10^{-6}	1.17×10^4	2.77×10^{16}
750	6.04×10^{-6}	9.76×10^3	2.31×10^{16}
800	1.11×10^{-5}	5.31×10^3	1.26×10^{16}
850	1.72×10^{-5}	3.43×10^3	8.11×10^{15}
900	2.69×10^{-5}	2.19×10^3	5.18×10^{15}
500	3.39×10^{-5}	1.74×10^3	4.12×10^{15}
1000	4.77×10^{-5}	1.24×10^3	2.93×10^{15}

TABLE 6. CALIBRATION DATA FOR RADIOMETER 4; SERIAL #16914-90-6;
 FILTER $\lambda=469$ NM

PMT (volts)	Current (amps)	$\mu\omega/\text{amp}$	Photons $\text{s}^{-1} \text{A}^{-1}$
500	5.53×10^{-7}	2.77×10^5	6.53×10^{17}
550	1.80×10^{-6}	8.49×10^4	2.00×10^{17}
600	2.91×10^{-6}	5.25×10^4	1.24×10^{17}
650	5.97×10^{-6}	2.56×10^4	6.05×10^{16}
700	1.07×10^{-5}	1.43×10^4	3.38×10^{16}
750	1.04×10^{-5}	8.30×10^3	1.96×10^{16}
800	2.04×10^{-5}	5.30×10^3	1.27×10^{16}
850	4.09×10^{-5}	3.74×10^3	8.82×10^{15}
900	6.07×10^{-5}	2.23×10^3	5.25×10^{15}
950	9.51×10^{-5}	1.61×10^3	3.79×10^{15}
1000	1.30×10^{-4}	1.18×10^3	2.78×10^{15}

TABLE 7. CALIBRATION DATA FOR RADIOMETER 5; SERIAL #16914-90-3;
 FILTER $\lambda=467.5$ NM

PMT (volts)	Current (amps)	$\mu\omega/\text{amp}$	Photons $\text{s}^{-1} \text{A}^{-1}$
500	8.33×10^{-8}	5.45×10^5	1.28×10^{18}
550	2.77×10^{-7}	1.64×10^5	3.85×10^{17}
600	5.56×10^{-7}	8.18×10^4	1.92×10^{17}
650	1.39×10^{-6}	3.27×10^4	7.69×10^{16}
700	2.22×10^{-6}	2.04×10^4	4.81×10^{16}
750	3.09×10^{-6}	1.17×10^4	2.75×10^{16}
800	5.28×10^{-6}	8.61×10^3	2.03×10^{16}
850	9.72×10^{-6}	4.67×10^3	1.10×10^{16}
900	1.36×10^{-5}	3.34×10^3	7.85×10^{15}
950	1.81×10^{-5}	2.52×10^3	5.92×10^{15}
1000	2.22×10^{-5}	2.04×10^3	4.81×10^{15}

TABLE 8. CALIBRATION DATA FOR RADIOMETER 6; SERIAL #16914-90-2;
 FILTER $\lambda=454.6$ NM

PMT (volts)	Current (amps)	$\mu\omega/\text{amp}$	Photons $\text{s}^{-1} \text{A}^{-1}$
600	2.77×10^{-7}	1.24×10^5	2.04×10^{17}
650	1.11×10^{-6}	3.11×10^4	7.10×10^{16}
700	1.67×10^{-6}	2.07×10^4	4.73×10^{16}
750	3.33×10^{-6}	1.04×10^4	2.37×10^{16}
800	3.09×10^{-6}	8.87×10^3	2.03×10^{16}
850	6.67×10^{-6}	5.18×10^3	1.18×10^{16}
900	1.03×10^{-5}	3.37×10^3	7.70×10^{15}
950	1.50×10^{-5}	2.18×10^3	4.98×10^{15}
1000	1.94×10^{-5}	1.78×10^3	4.06×10^{15}

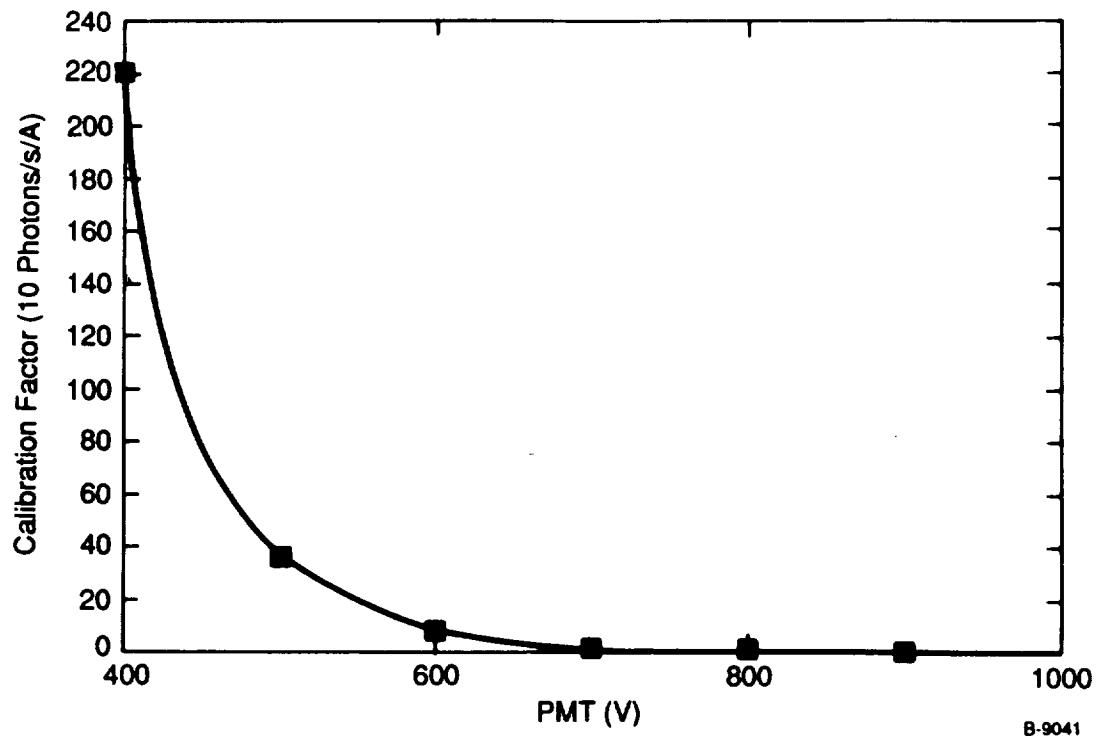


Figure 15. - 871.4 nm radiometer-calibration factor vs PMT voltage.

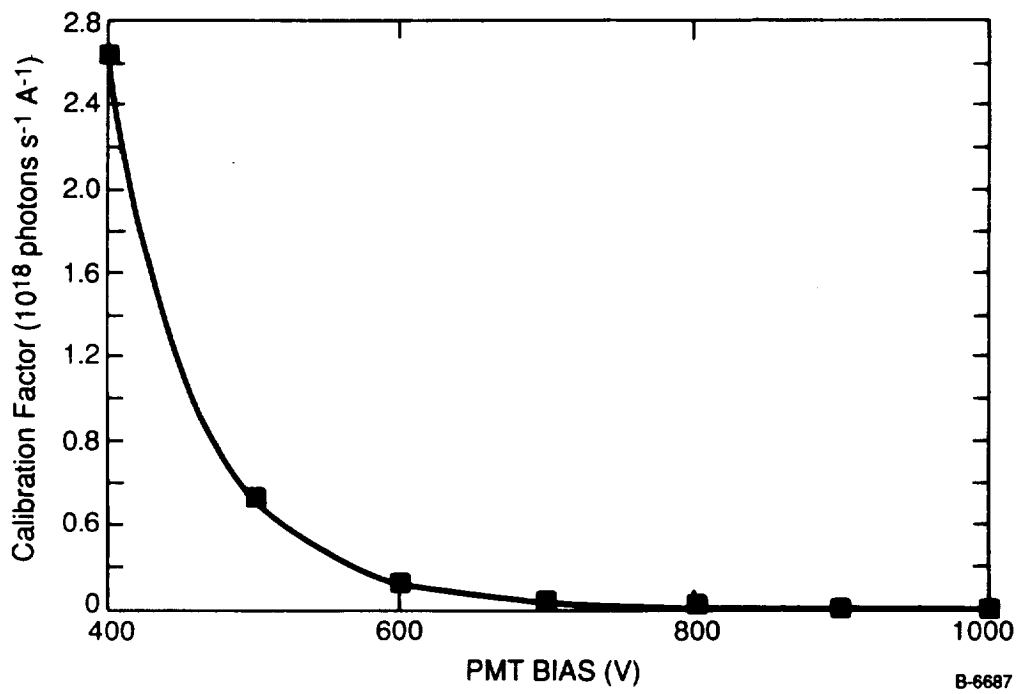


Figure 16. - 645 nm Radiometer - Calibration Factor versus PMT Voltage

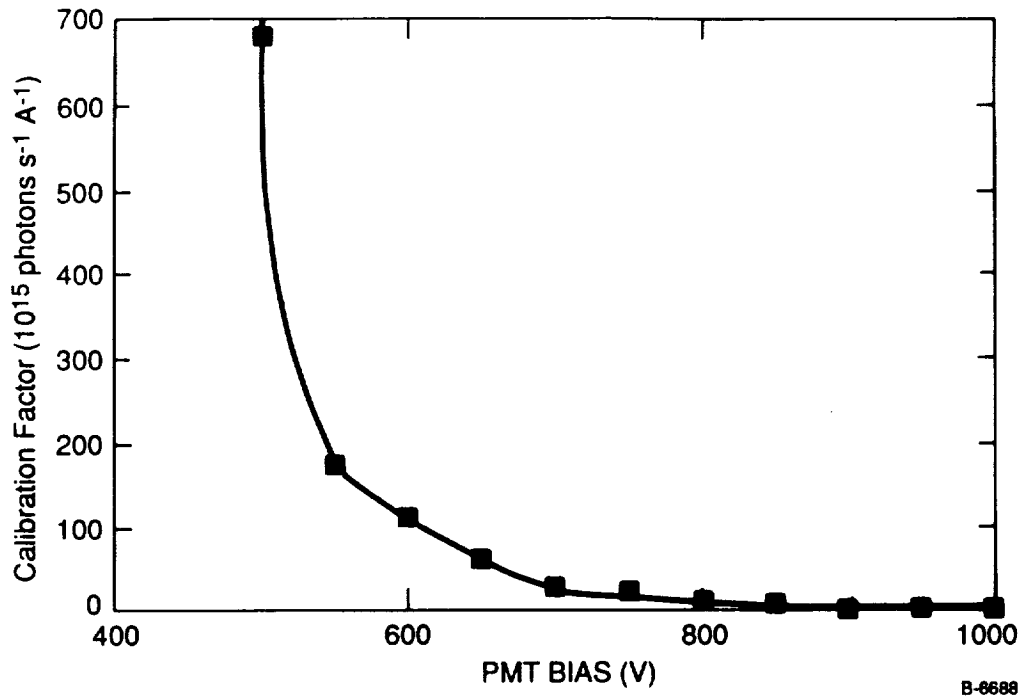


Figure 17. - 470.5 nm Radiometer - Calibration Factor versus PMT Voltage

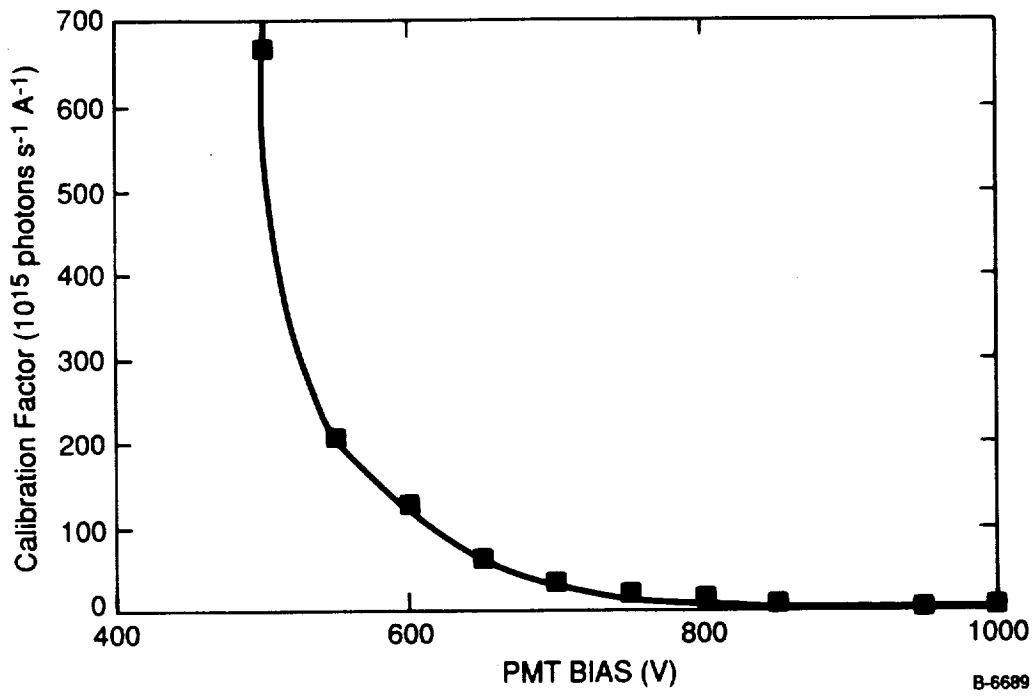


Figure 18. - 469.0 nm Radiometer - Calibration Factor versus PMT Voltage

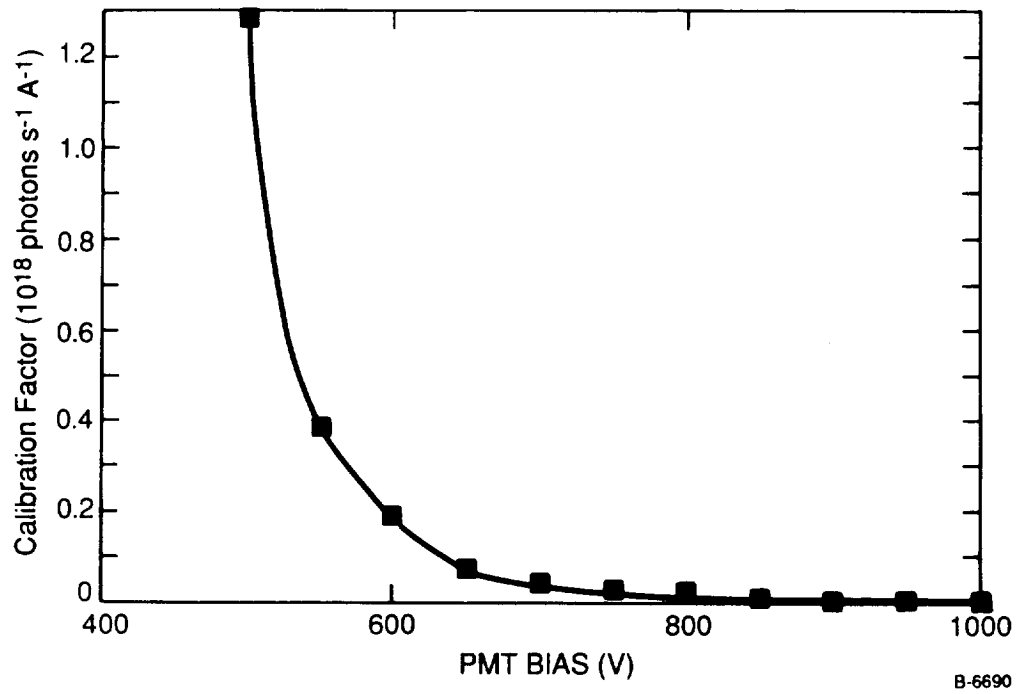


Figure 19. - 467.5 nm Radiometer - Calibration Factor versus PMT Voltage

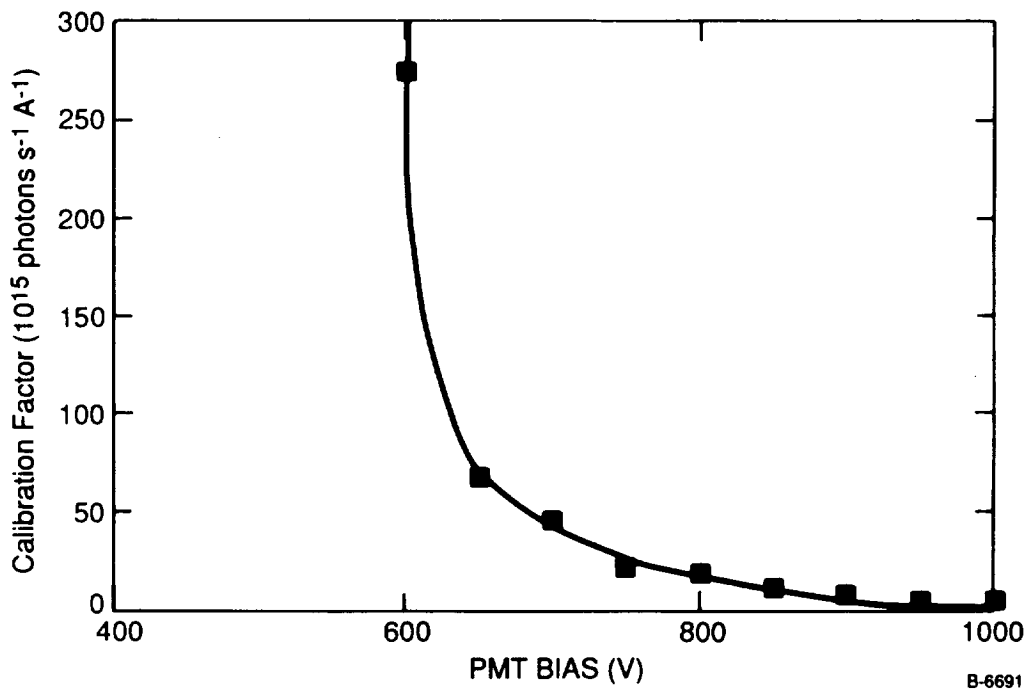


Figure 20. - 454.6 nm Radiometer - Calibration Factor versus PMT Voltage

2.7 OMA Calibration Procedure

The configuration used in calibrating both OMAs is shown in Figure 21. The two OMA diagnostics differ only in monochromator grating and relevant wavelength dispersion on the diode array. Table 9 gives the specifics of the two monochromator/OMA configurations. Wavelength calibration was accomplished with commercially available pen ray lamps which give characteristic atomic line transitions.

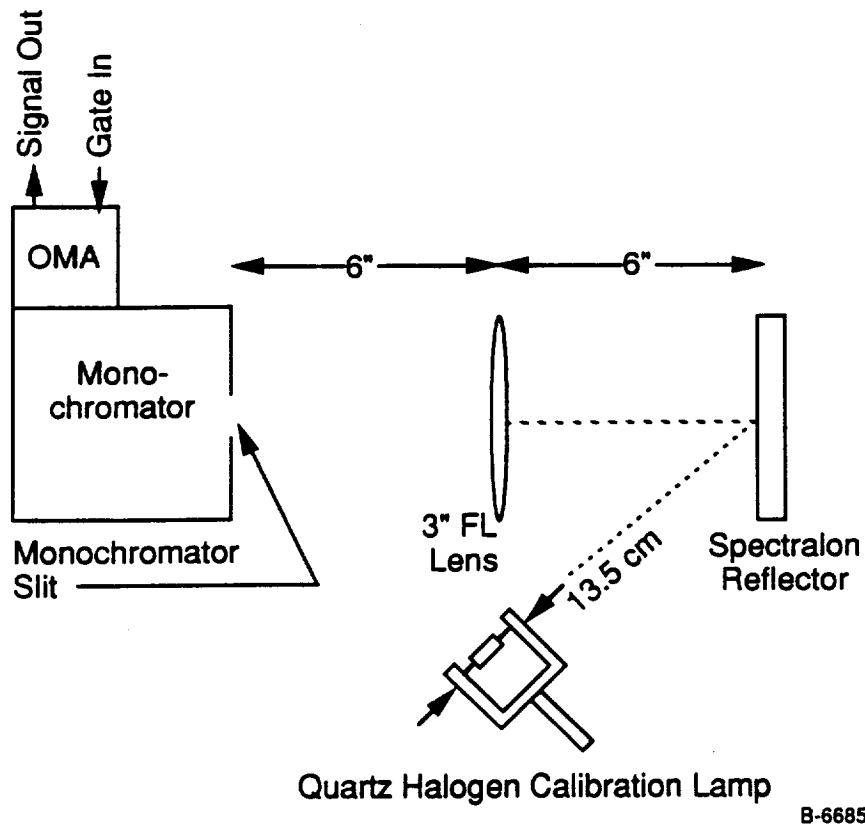


Figure 21. Experimental Configuration for OMA Calibration

Table 9. OMA Diagnostic Specifications

	Grating	Center λ (nm)	Spectral Range (nm)
Broad band OMA	150 g/mm	490.0	297-683
Narrow band OMA	300 g/mm	393.0	309-477

A quartz halogen irradiance standard is used in the absolute calibration of the OMAs. It is positioned 13.5 cm from a Lambertian reflector (Spectralon). The lamp irradiates a spot on the reflector at an incident angle of 45 deg. The reflection of the spot is imaged through a 3-in. focal length lens onto the monochromator slit. The gated OMA head detects the signal and the OMA controller records and saves the lamp spectrum. A known power reflected off the Spectralon reflector results in a specific number of detected counts for a given monochromator slit width, gate time and at a given wavelength. A calibration spectrum can then be synthesized relating the absolute power reflected off the Spectralon to the signal detected by the OMAs.

To determine the reflected irradiance of the quartz halogen lamp, we need to adjust reported irradiance values to accommodate the geometry of this experiment. The irradiance of the lamp at a given distance is calculable since it falls off as $1/r^2$. The reflection and angle requirements are incorporated by Lambert's cosine law. The reflected intensity $I_r = I_o \cos\theta$ where θ is the angle to the surface normal. It is also necessary to take into account the distribution of reflected light. The reflected irradiance will be distributed spherically and equally in all directions. The fraction we collect is the ratio of the lens area to the surface area of half of a sphere whose radius equals the distance from the reflector to the lens. Since the Spectralon is an imperfect reflector we incorporate a reflectance factor of 0.99 as well.

The equation used to make these adjustments is:

$$I_c = I_o \left[\frac{r_0^2}{r_1^2} \right] \left[\frac{\pi d^2/4}{4\pi s^2/2} \right] (0.99)(\cos(\theta))$$

where

- I_o = reported irradiance at 50 cm ($\mu\text{w cm}^{-2} \text{ nm}^{-1}$)
- d = lens diameter
- s = distance from reflector to lens
- r_0 = distance at which irradiance is known
- r_1 = distance from lamp to reflector
- θ = angle of lamp with respect to reflector normal.

Table 10 lists the adjusted irradiance values from 400 to 900 nm in 50 nm increments.

The calibration factors are calculated from the ratio of the experimentally determined signal levels of the lamp spectrum, in counts per second, to the adjusted irradiance values. Since each diode on the array requires a calibration factor, we interpolate between the known irradiance values of Table 10 to cover the entire spectrum. A window loss factor of 0.92 is applied to the calibration factors as well to account for the quartz window transmission loss we experience in the shock tube experiment.

TABLE 10. ADJUSTED IRRADIANCE VALUES

Wavelength	Reported Irradiance ($\mu\text{w cm}^{-2} \text{ nm}^{-1}$)	Adjusted Irradiance ($\mu\text{w cm}^{-2} \text{ nm}^{-1}$)
400	0.0727	0.0436
450	0.154	0.0923
500	0.266	0.1595
550	0.396	0.2375
600	0.53	0.3179
650	0.66	0.3959
700	0.770	0.4667
750	0.066	0.5195
800	0.929	0.5573
900	0.909	0.5933

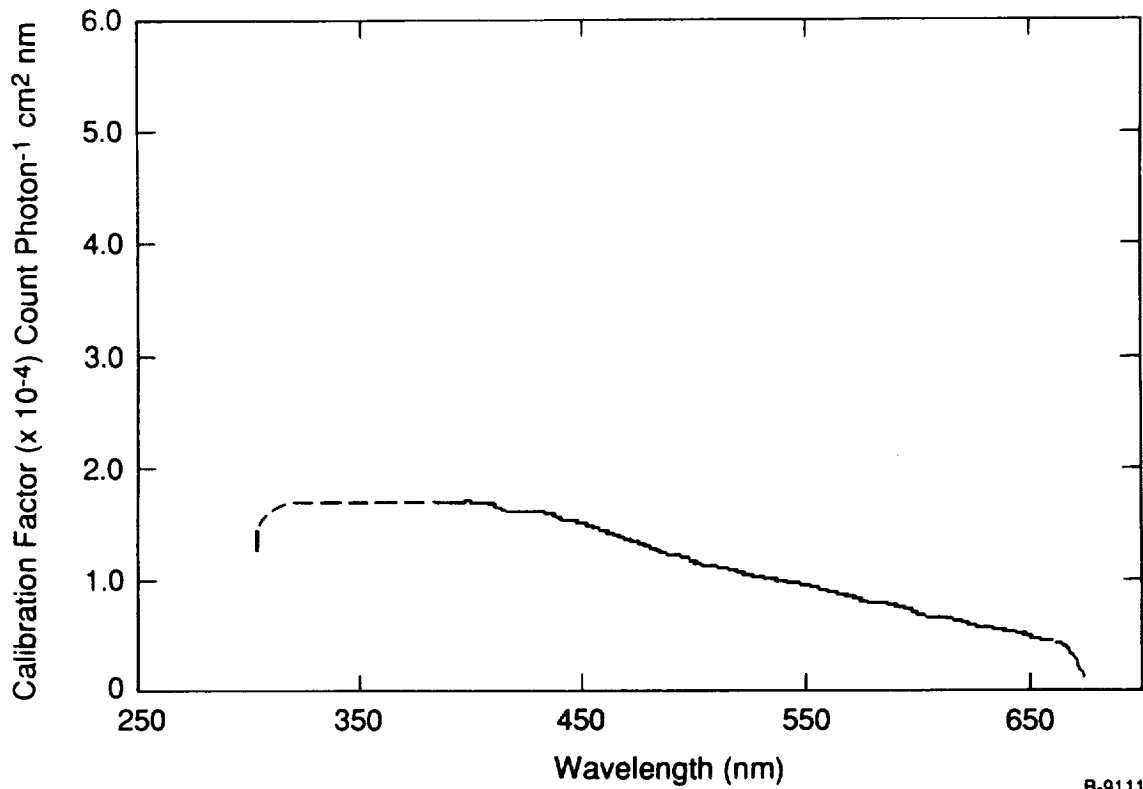
The calibration factors have units of count photon⁻¹ cm² nm. They are linearly related to resolution (slit width) and the gate width of the experiment. Figure 22 shows the calibration spectrum for the broad band OMA with a 500 μ monochromator slit (10 nm resolution) and gate width of 5 μ s. The narrow band OMA calibration spectrum, shown in Figure 23 is for a 1 mm slit width (1 deg resolution) and 1 ms gate width.

These calibration factors are further manipulated for use in our spectral fitting codes. A volume emission rate per count in absolute units is required to convert observed intensities to number densities in molecules cm⁻³. A calibration factor, C₁ determined under the same conditions of slit width and gate time, is easily converted to the appropriate units of photons s⁻¹ cm⁻³ count⁻¹ via:

$$\frac{(\text{volume emission rate})}{ct} = \left[\frac{1}{C_1} \right] \Delta\lambda a V^{-1} t^{-1}$$

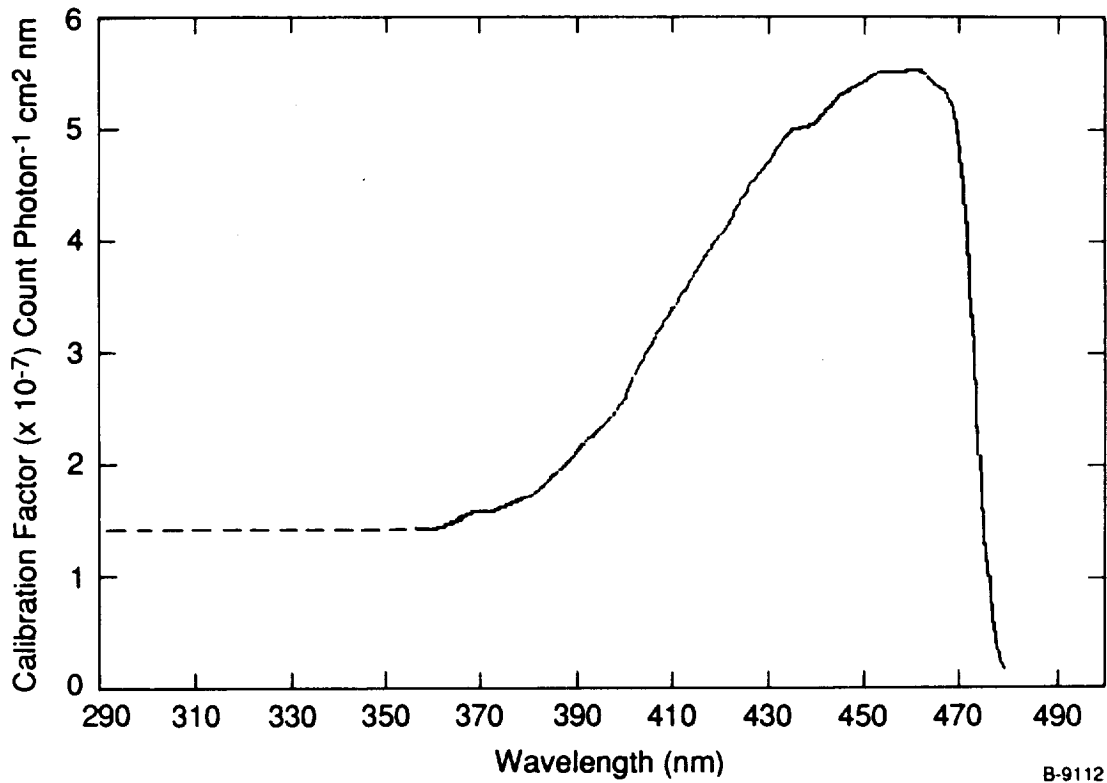
where:

- C₁ = calibration factor in count/(photon/cm²/nm)
- $\Delta\lambda$ = resolution (nm)
- a = slit area (cm²)
- V = collection volume (cm³)
- t = gate time (s).



B-9111

Figure 22. - Calibration spectrum.



B-9112

Figure 23. - Calibration spectrum narrow band OMA.

3. DATA OVERVIEW AND INTERPRETATION

We realized a total of eight shots which provided useful data at velocities ≥ 5.8 km/s. A summary of the data base is provided in Table 11. The OMA's were generally gated so that one viewed the non-equilibrium portion of the shock while the other viewed the equilibrium region. It will be noted from Table 11 however that the spectral coverage and resolution was varied from time to time over the shot sequence.

It should be made clear that numerous other shocks were fired providing experience on gating sequence and integration times. We had only one equipment failure over the testing period. This occurred for a procedural reason which has now been corrected and we believe that the tube shakedown and operational procedures are now complete.

As can be seen from Table 11, the tests conditions span the velocity range from 5.8 to 12.1 km/s and are mostly for a pressure of 0.1 torr in nitrogen although there are two runs at 1.0 torr and two runs in air. This range of conditions covers a wide variation in gas thermochemical/thermodynamic state. For example, Figure 24 provides a comparison between frozen and equilibrium temperatures behind the shock front vs shock velocity for nitrogen at $P_1=0.1$ torr. We see, for example, that at 6 km/s the temperature directly behind the shock is ~ 12000 K and relaxes to less than 6000 K as the gas approaches equilibrium. It is not surprising that large variations are observed between non-equilibrium and equilibrium radiative signatures. Figures 25 and 26 show the variation in equilibrium temperature and density vs shock velocity in N_2 at incident shock pressures of 0.1, 1 and 10 torr. Note that between 6 and 12 km/s, the range of the present experiments, even the equilibrium temperature doubles. The equilibrium species concentrations vs velocity for these three pressures are shown in Figure 27 through 29. As can be seen between 6 and 12 km/s, the gas goes from being partially dissociated and slightly ionized to largely dissociated and highly ionized. A similar set of predictions are provided for air in Figures 30 through 34. As can be seen the trends are similar to that observed in N_2 although the species distribution is much richer in air. Figure 32 shows that the equilibrium molecular and ionic concentrations are both of order 1 percent at 9 km/s, $P_1=0.1$ torr, the approximate conditions of the present measurements in air.

We conclude that the dominant radiation to be seen in the present data base will be electronic transitions of N_2 , N_2^+ , N, O, and bremsstrahlung continuum. The dominant transitions of NO and O_2 fall at wavelengths below 300 nm, and were not investigated in the present study.

TABLE 11. SUMMARY OF SHOCK TEST CONDITIONS

Fill Gas	Fill Pressure (torr)	Speed	Narrow band OMA		Broad Band OMA		Radiometer λ (nm)
			λ range, (nm)	gate width	λ range, (nm)	gate width	
N ₂	1.0	6.15	377-395	2 μ s non-equilib.	340-726	10 μ s equilib.	645.0
				470.5			
				454.6			
				391.4			
N ₂	0.1	9.1	377-395	3 μ s equilib.	297-683	1.0 μ s non-equilib.	870.0
				645.0			
				470.5			
				391.4			
air	0.1	9.0	377-395	3 μ s equilib.	297-683	1.0 μ s non-equilib.	870.0
				645.0			
				470.5			
				391.4			
air	0.1	9.4	309-477	1 μ s non-equilib.	297-683	3.35 μ s equilib.	870
				645.0			
				469.0			
				391.0			
N ₂	1.0	5.8	309-477	1 μ s non-equilib.	297-683	3.35 μ s equilib.	870
				645.0			
				470.5			
				391.4			
N ₂	0.1	7.4	309-477	1 μ s non-equilib.	297-683	3.35 μ s equilib.	870
				645			
				470			
				469			
N ₂	0.1	11.81	309-477	1 μ s non-equilib.	297-683	3.35 μ s equilib.	no data
				391.4			
N ₂	0.1	12.1	309-477	1 μ s non-equilib.	297-683	3.35 μ s equilib.	870
				645			
				470			
				409			
							391.4

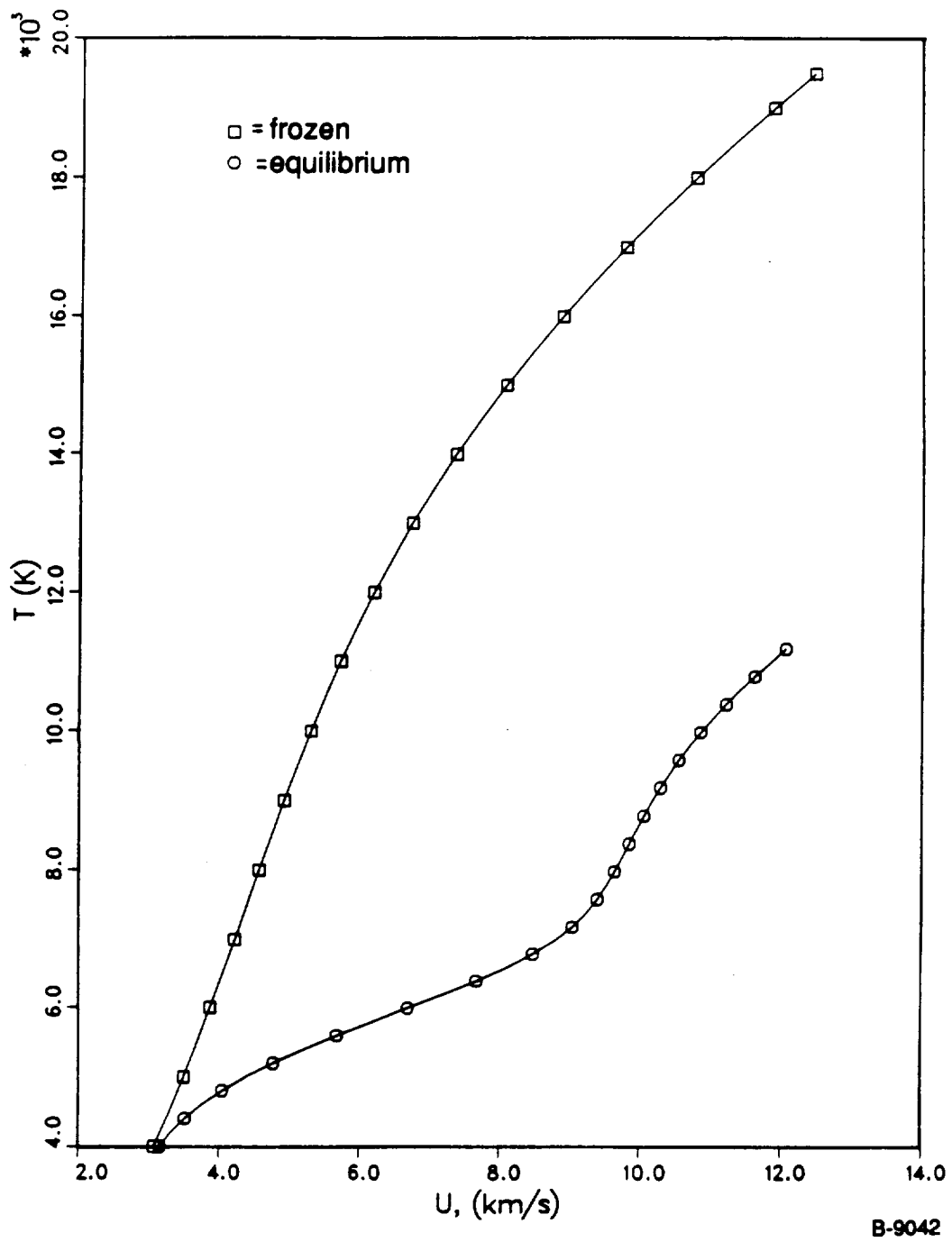


Figure 24. - Contrast between frozen and equilibrium temperatures behind normal shocks. Pure nitrogen, P=0.1 torr

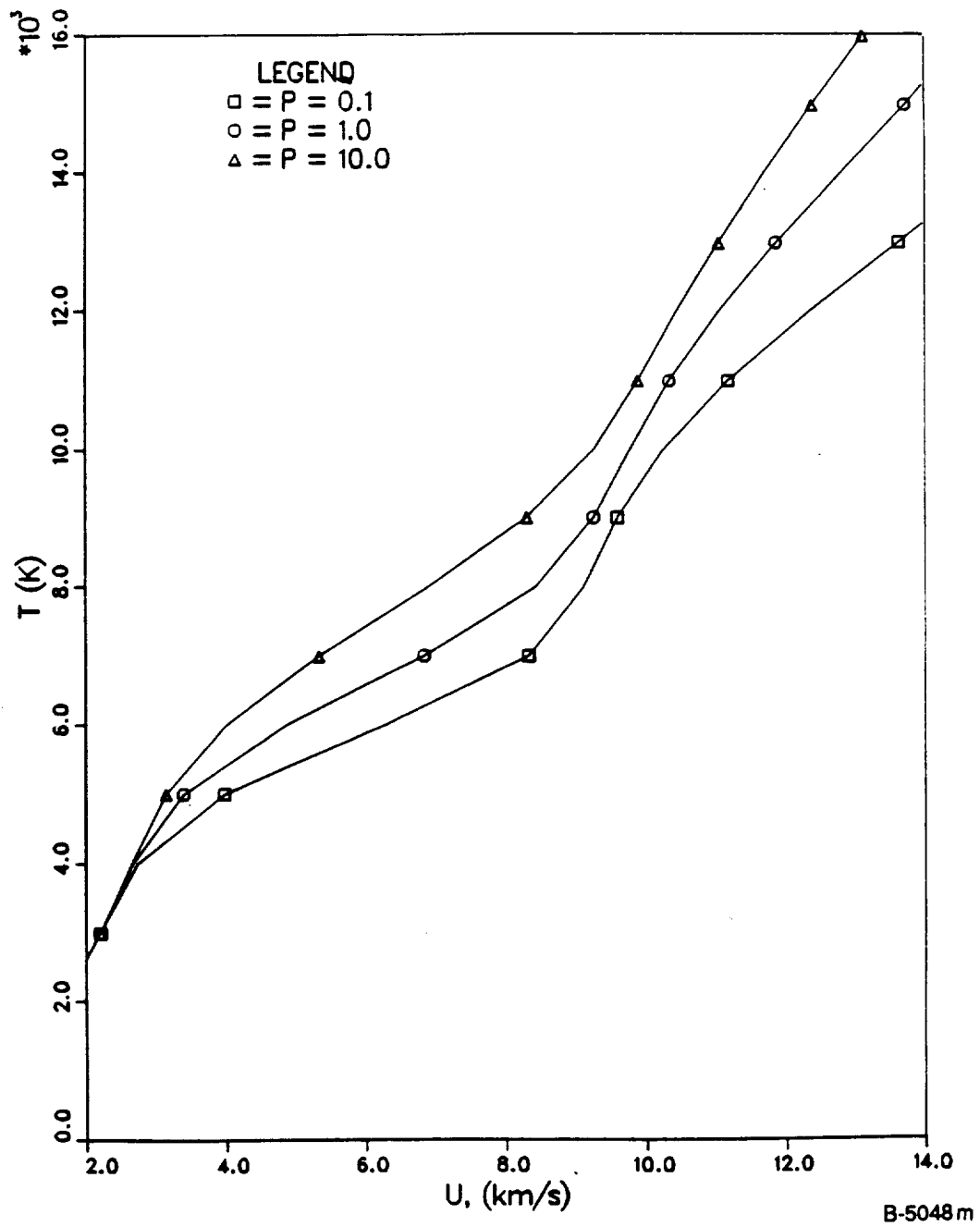


Figure 25. - Pure N_2 equilibrium temperature behind a normal shock vs shock velocity

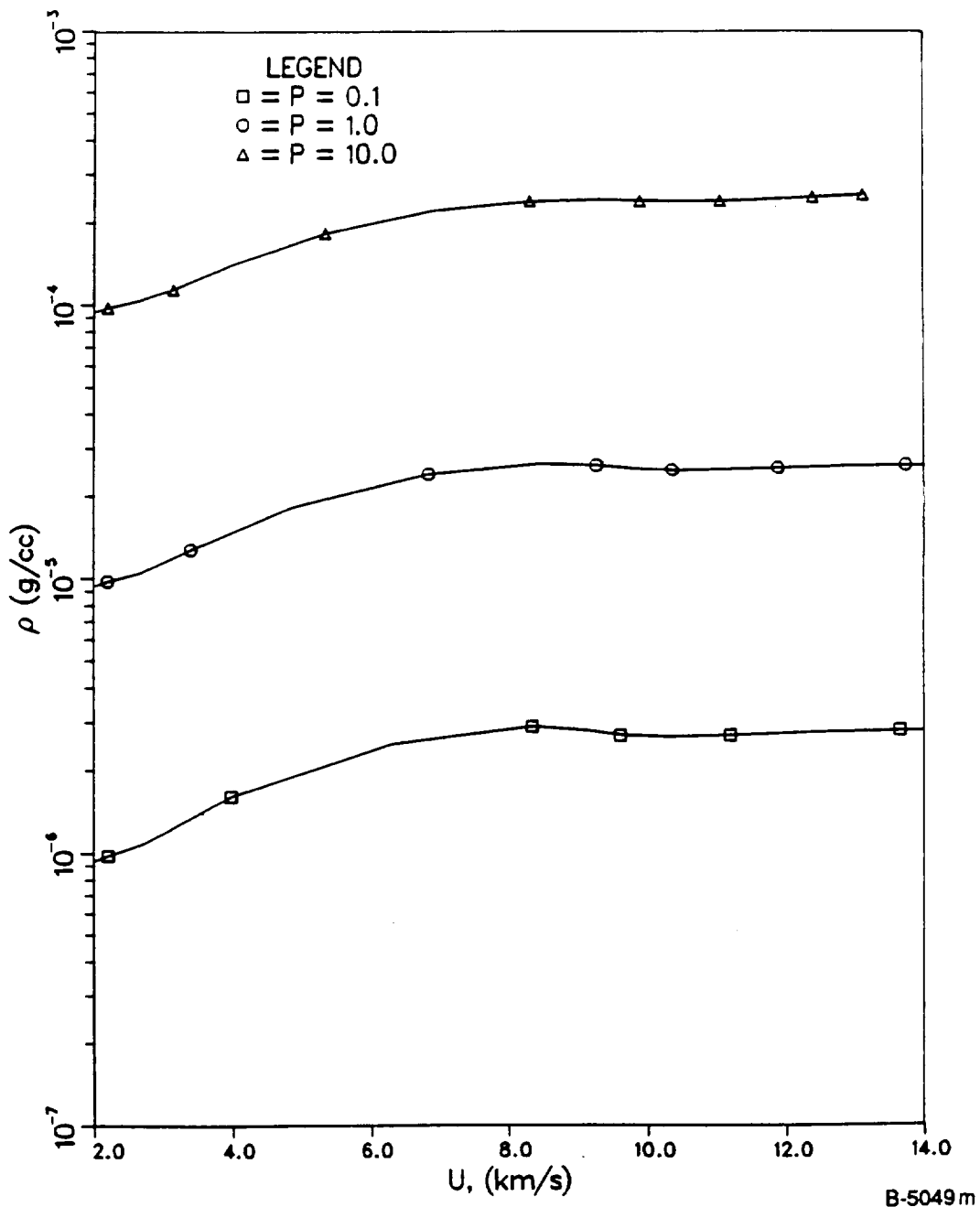


Figure 26. - Pure N₂ equilibrium density

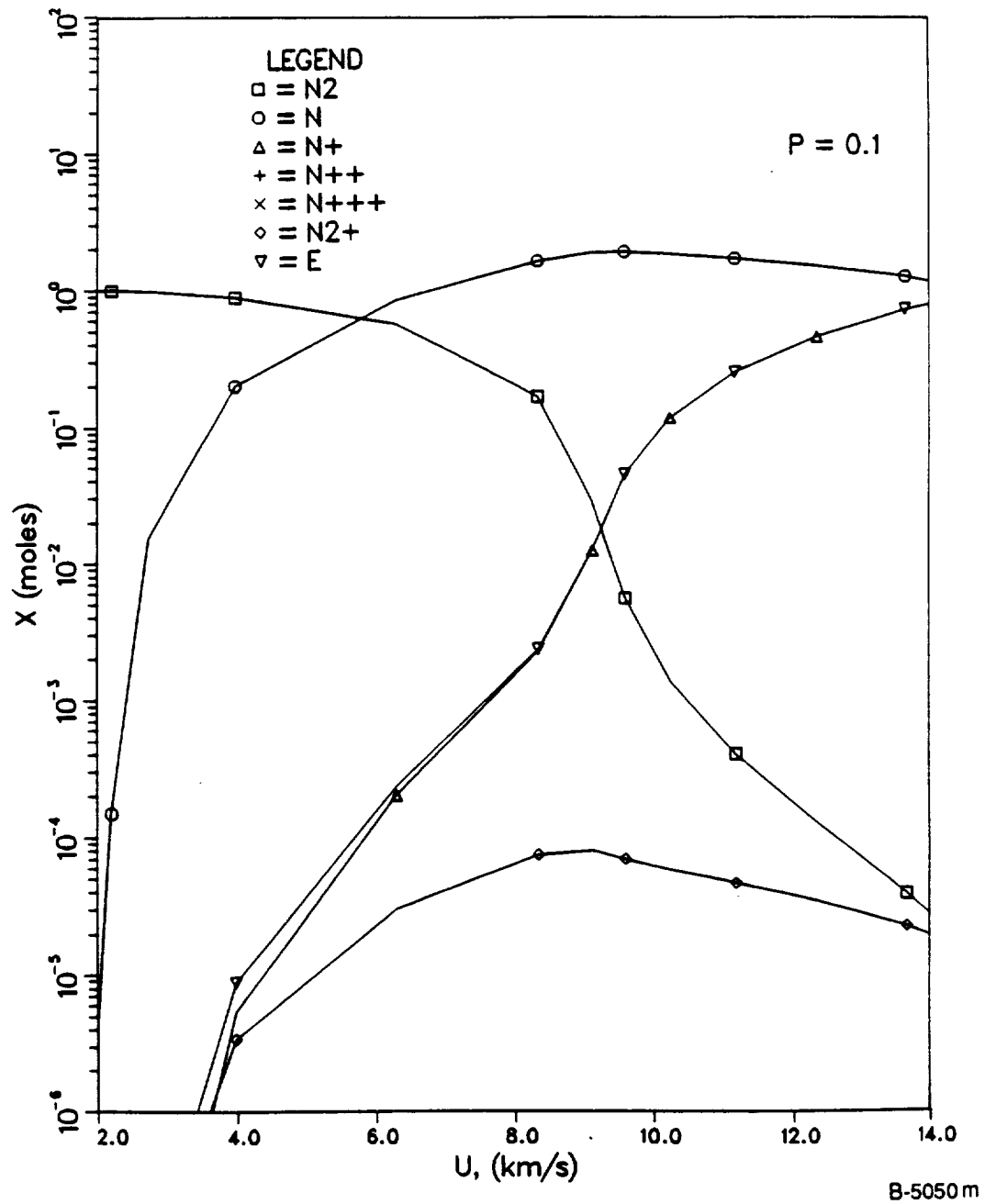


Figure 27 - Pure N₂ equilibrium species concentration vs shock velocity, P = 0.1 torr.

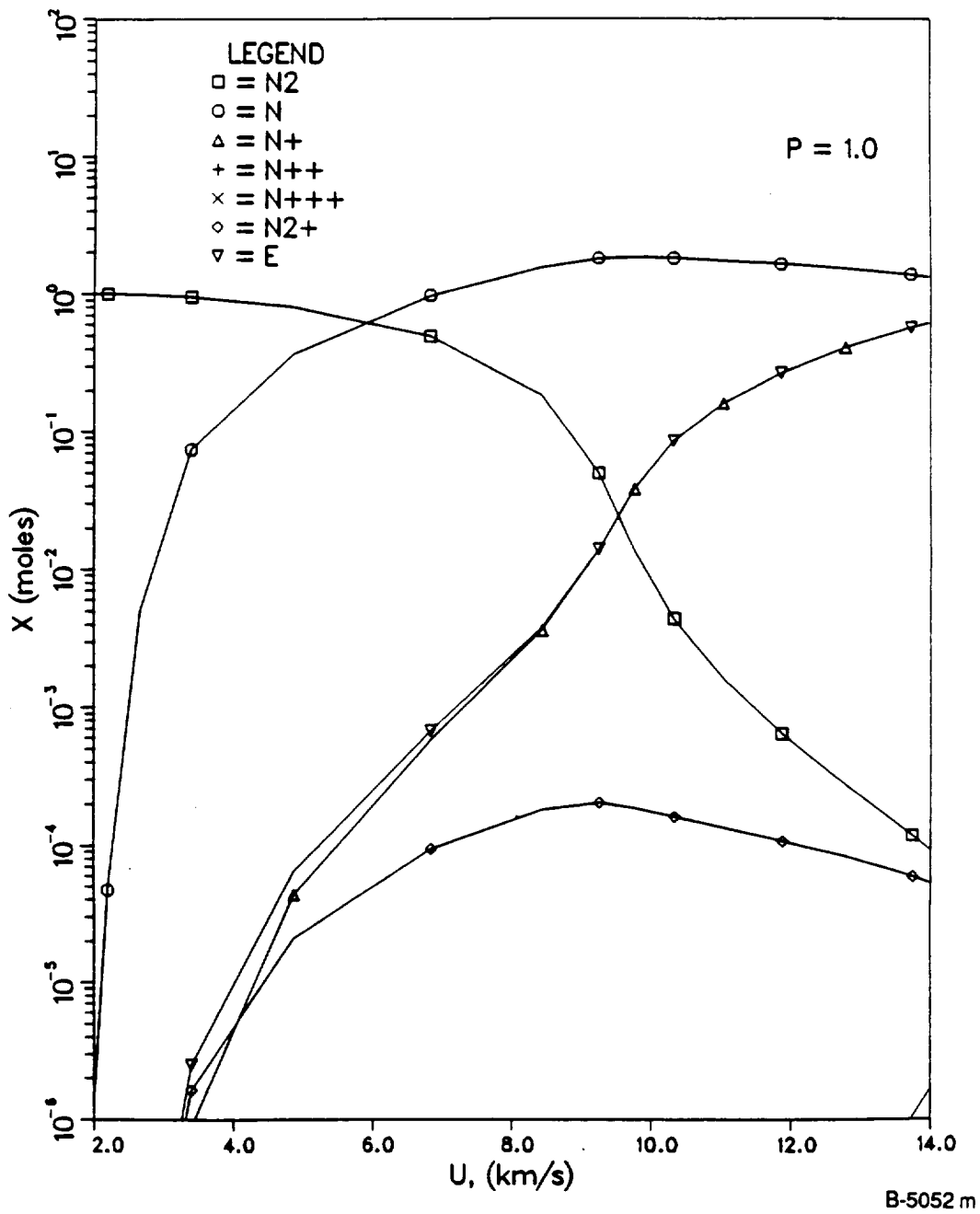


Figure 28. - Pure N_2 equilibrium species concentration vs shock velocity, $P = 1$ torr.

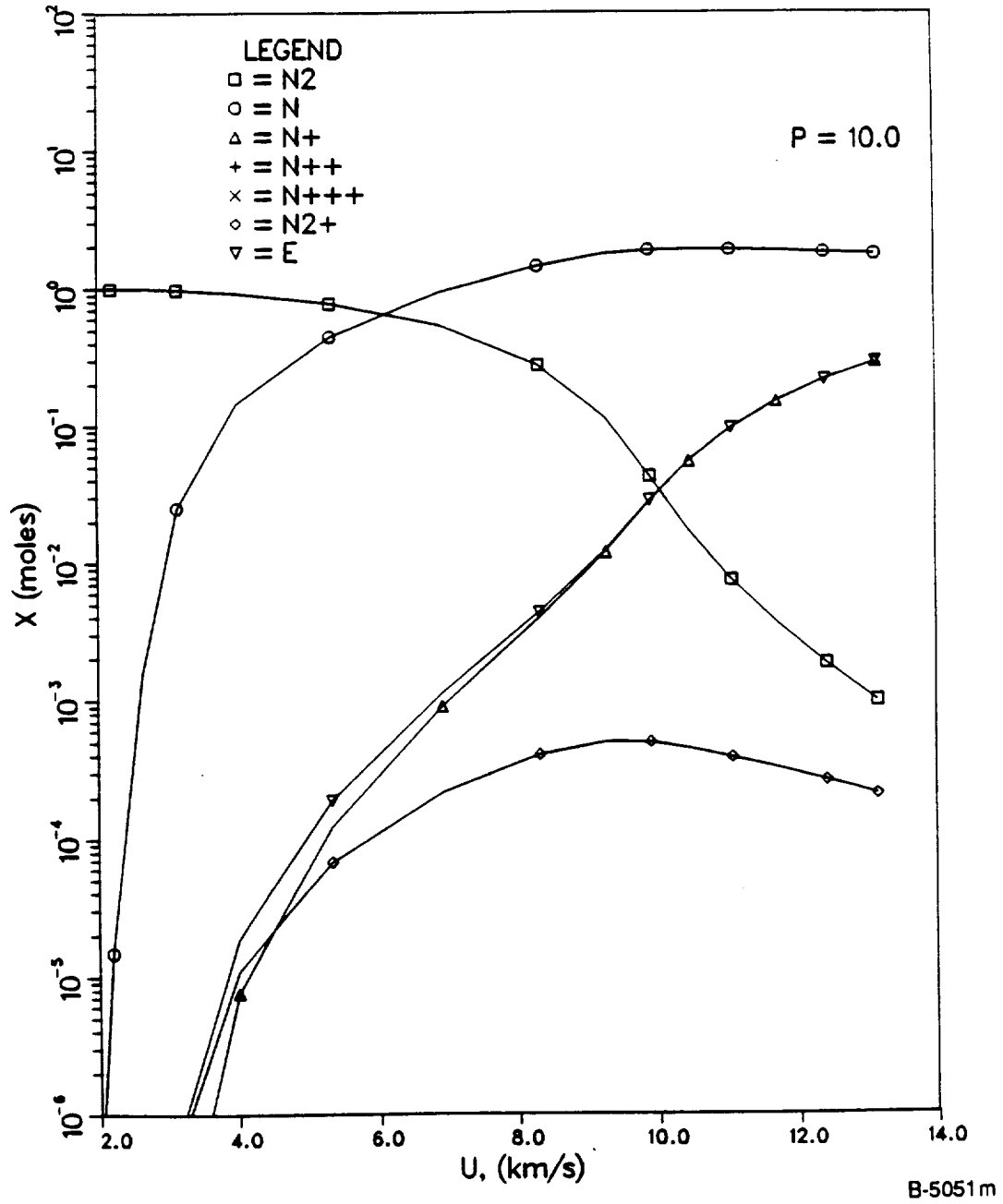


Figure 29. - Pure N₂ equilibrium species concentration vs shock velocity, P = 10 torr.

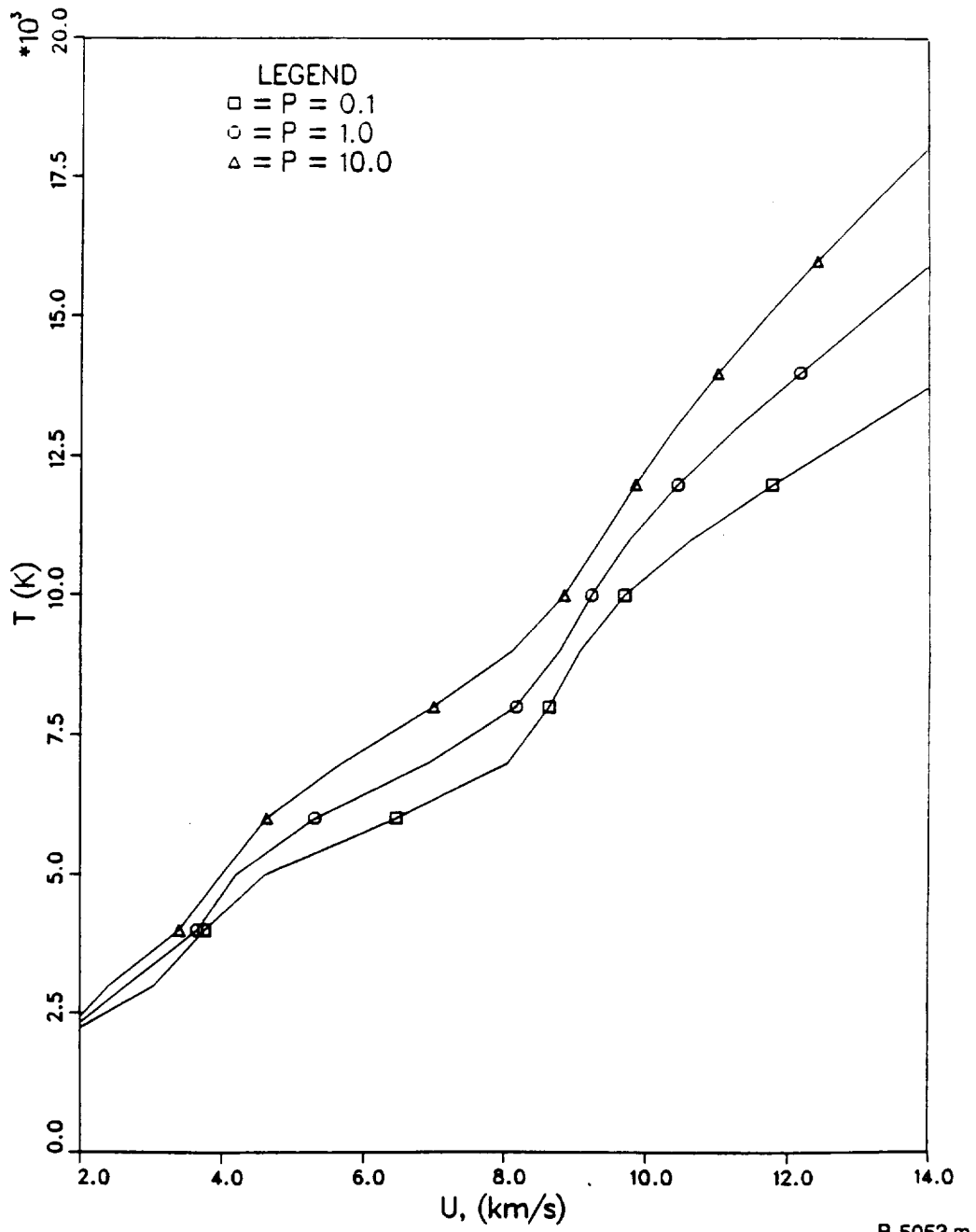


Figure 30. - Equilibrium air temperature vs shock velocity.

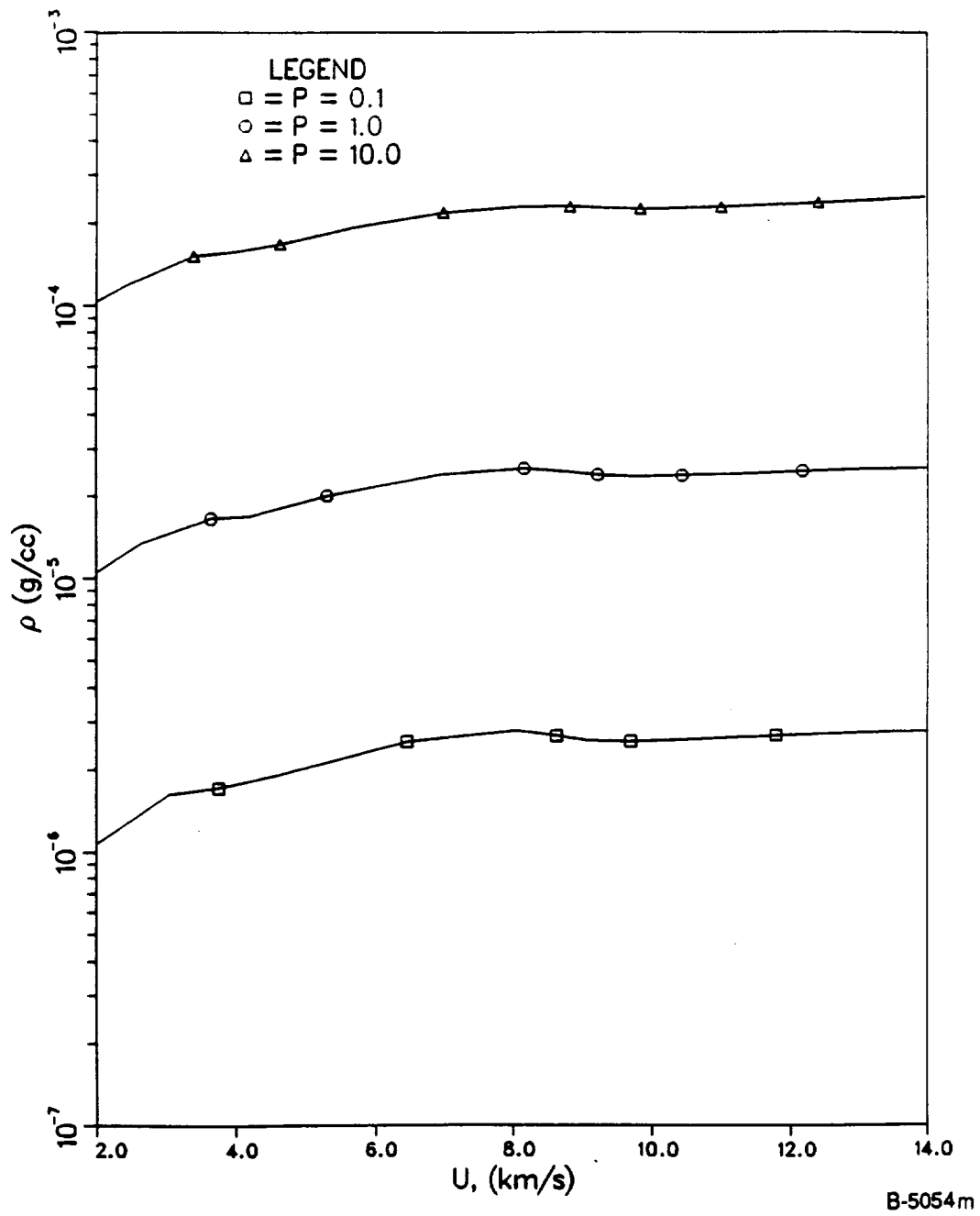


Figure 31. - Equilibrium air density vs shock velocity.

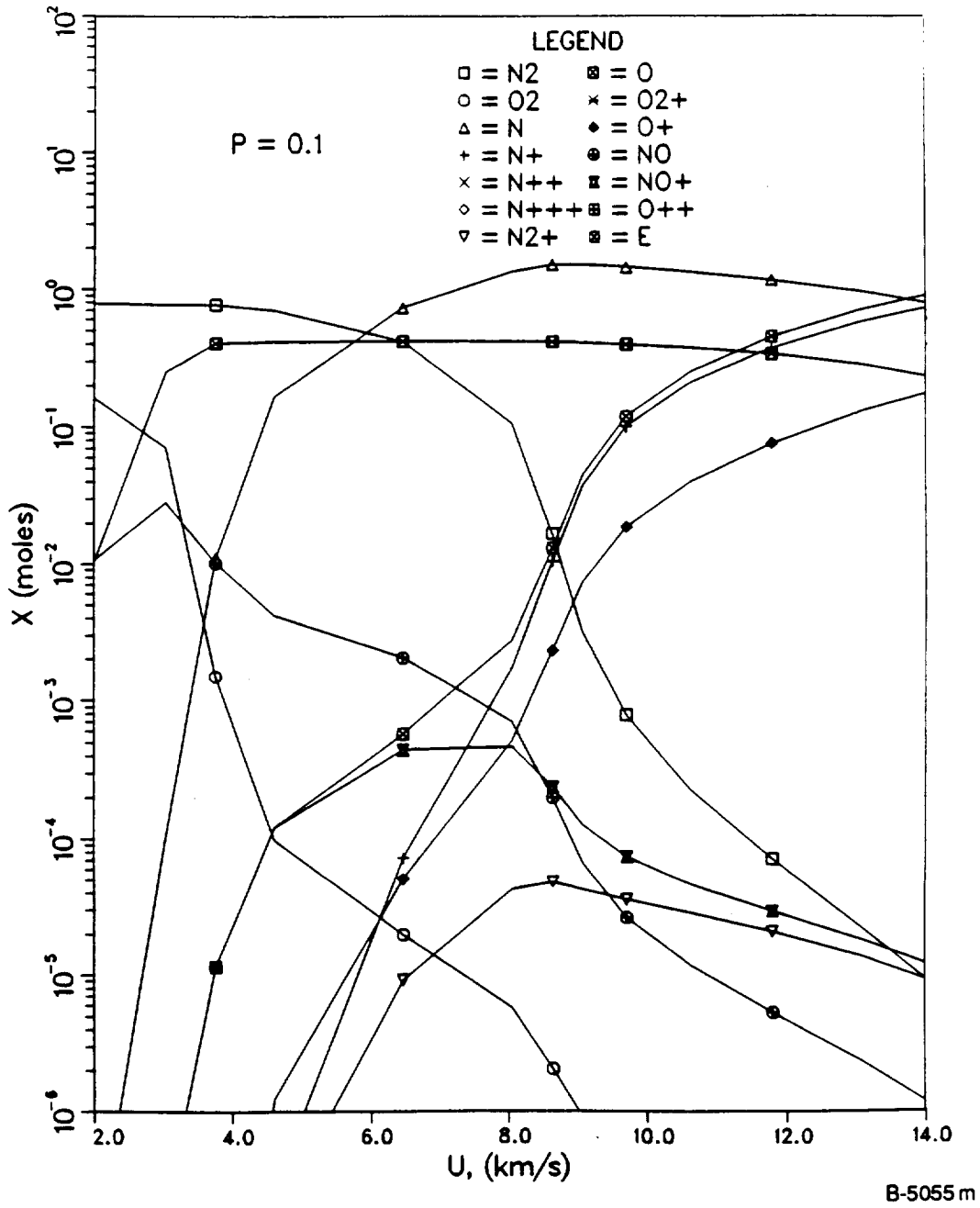


Figure 32. - Equilibrium air species vs shock velocity, P = 0.1 torr.

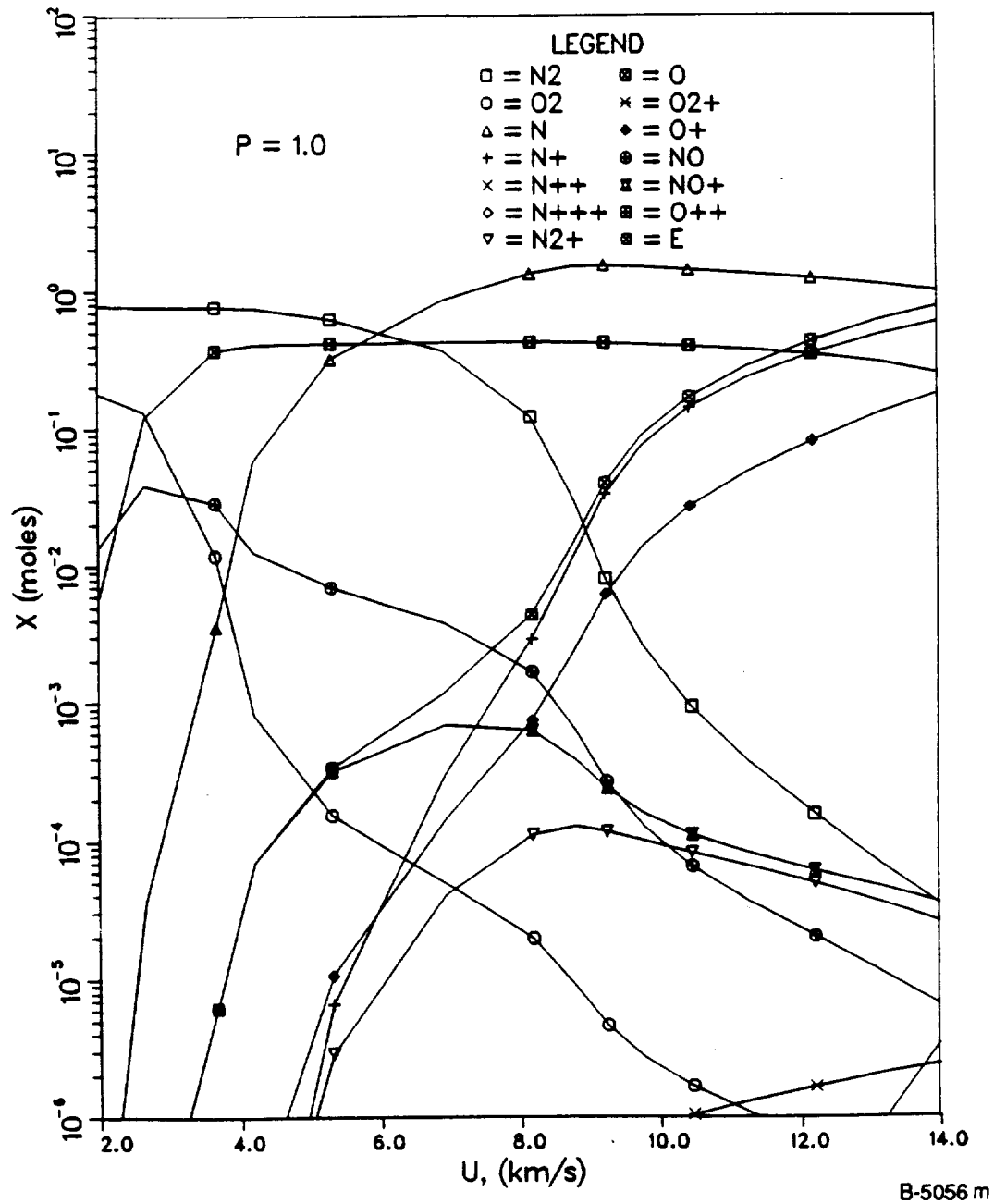


Figure 33. - Equilibrium air species vs shock velocity, P = 1 torr.

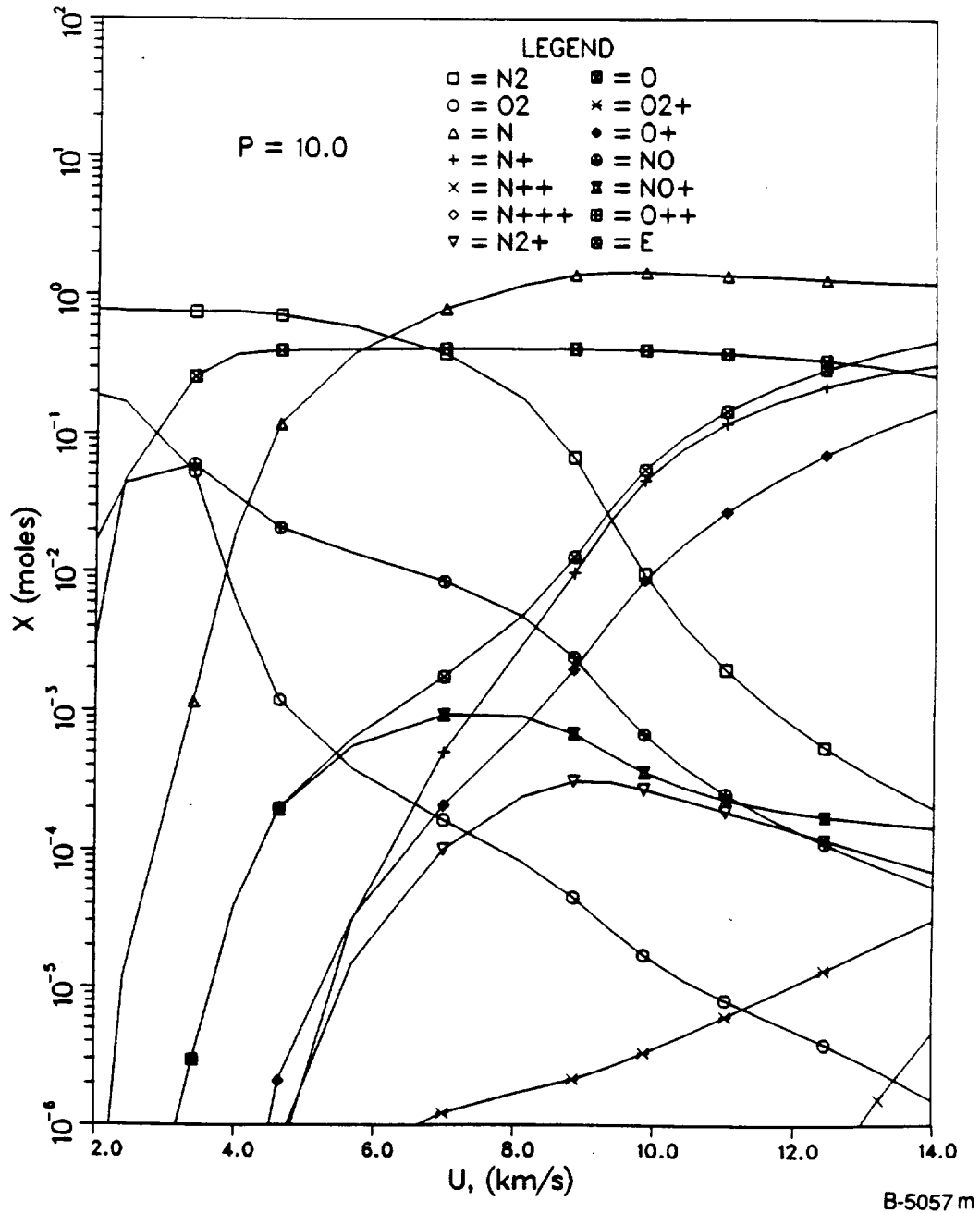


Figure 34. - Equilibrium air species vs shock velocity, P - 10 torr.

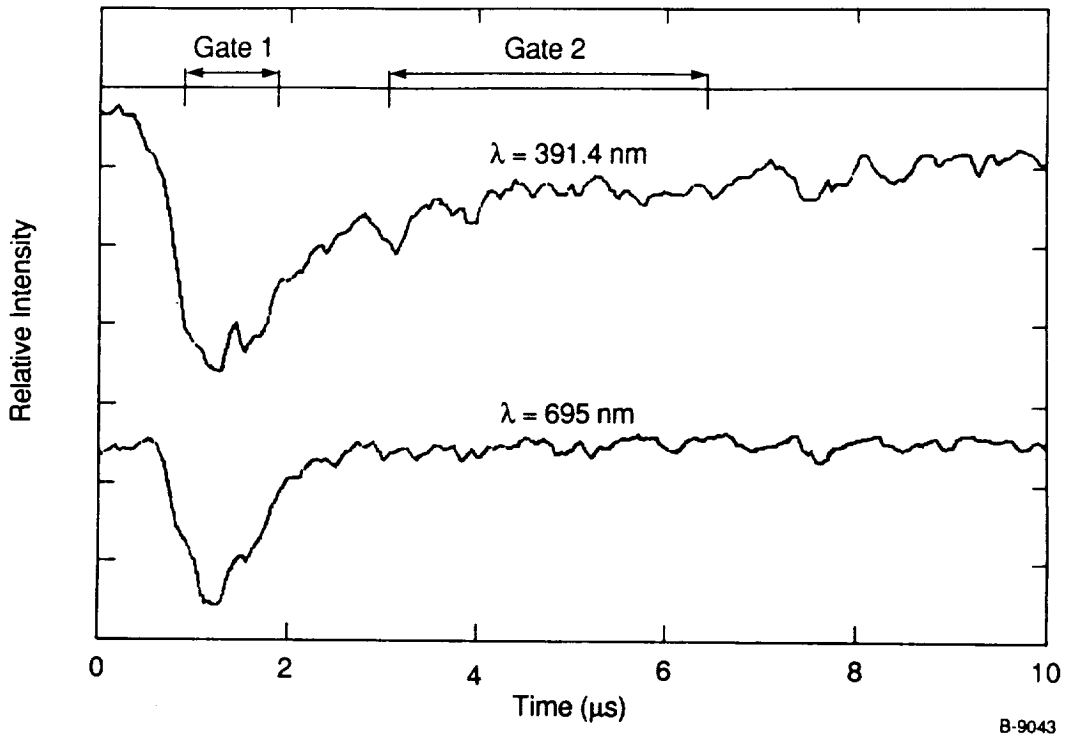
3.1 Radiometer Analysis

The radiometer data base has provided mixed results. It had been hoped that the narrowband radiometers could be used to back out N_2 rotational and vibrational temperature histories. This was not the case because of signal to noise (S/N) limitations. Although the equilibrium and non-equilibrium regions were generally identifiable on each trace several of the radiometer bandpasses exhibited S/N or 2-4. In particular the 470.5 and 453.6 nm radiometers, which were to be used to deduce rotational temperature, had low S/N, as did the 870 nm radiometer. These data were of some value in characterizing the characteristic kinetic times of the non-equilibrium region, but useless for deducing temperatures. Nonetheless, these radiometers could prove useful in the future if their collection efficiency is greatly improved.

The best S/N was observed with the broadband 391.4 nm and narrowband 645 nm radiometers. The former monitors both the N_2^+ (B-X) first negative system and the CN violet bands. As will be seen in the discussion of the OMA data, the impurity CN dominated that of N_2^+ in all the data. The 645 nm radiometer monitored the N_2 (B-A) first positive system. No OMA data is available for this spectral region.

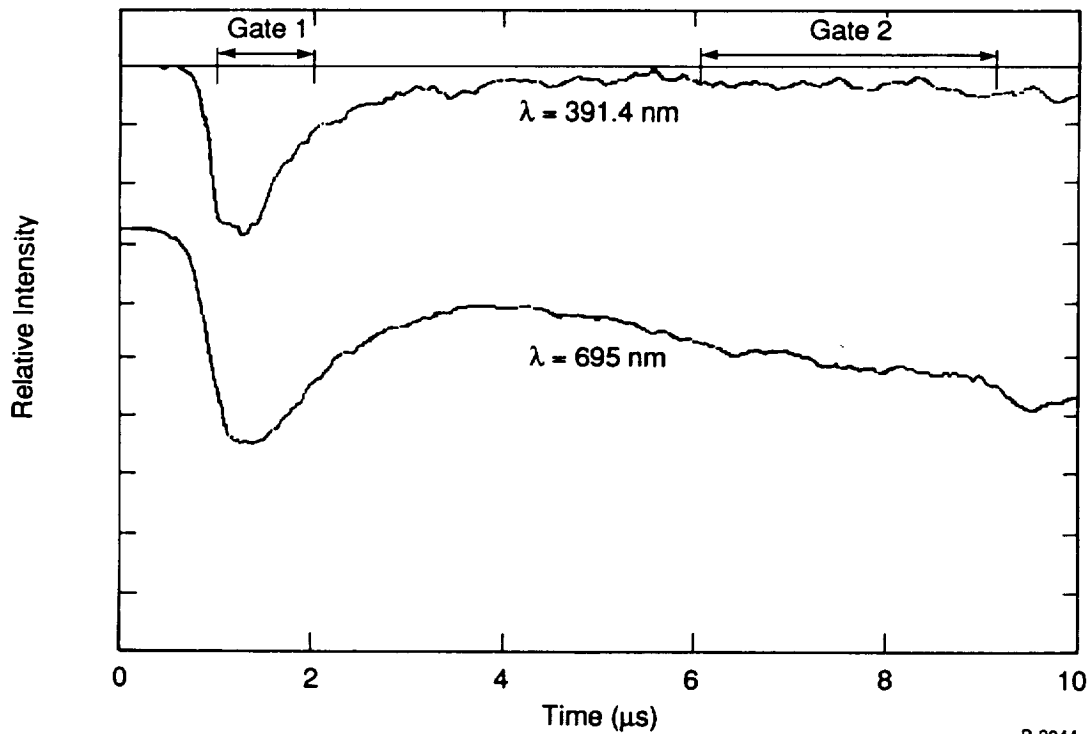
For purposes of illustration we will highlight the data taken for $P=0.1$ torr in N_2 at velocities of 7.4, 9.1 and 12.1 km/s. The radiometer traces at 391.4 and 645 nm are contrasted for these three velocities in Figures 35 through 37. As can be seen each trace shows a clearly delineated non-equilibrium region in the first few micro-seconds behind the shock front, followed by a plateau region which characterizes the equilibrium gas. Note that test times for these shots are all $\geq 8 \mu s$ in agreement with the AERL observations.⁴ It can be seen that the S/N of the 645 nm radiometer is much lower than that of the 391.4 nm radiometer, reflecting both intensity levels and bandwidths. Yet the generic shapes are similar. It is interesting to note that the ratio of peak non-equilibrium intensity to equilibrium intensity, I_p/I_e , is quite distinct for the two bandpasses. This is exemplified in Table 12 which displays this ratio versus velocity for the two bands. For the 391.4 band the ratio is relatively insensitive to velocity and the difference between non-equilibrium and equilibrium regions is only ~ 2.5 to 3.0. We note that CN is a trace species and its band intensity per molecule is a relatively weak function of temperature.

The situation is quite distinct at 645 nm. Here the non-equilibrium region is presumably dominated by N_2 (B \rightarrow A) radiation. At these velocities the N_2 dissociates as the gas drives toward equilibrium and the equilibrium concentration is quite low, see Figure 23. This coupled with the lower equilibrium temperature is most likely the cause for the high values of I_p/I_e at velocities of 7.4 and 9.1 km/s. We note that the value of I_p/I_e of ~ 10 at $U_s = 9.1$ km/s is in good agreement with that deduced by AERL at $P = 0.1$ torr air and 10 km/s. Indeed the values deduced for air in the present study are reasonably close to those for N_2 in these bandpasses.



B-9043

Figure 35. - Radiometers signal vs time for the 391.4 and 645 nm bands. Timing of OMA gates are shown. $P=0.1$ torr N_2 , U_s 7.4 km/s.



B-9044

Figure 36. - Radiometers signal vs time for the 391.4 and 645 nm bands. Timing of OMA gates are shown. $P=0.1$ torr N_2 , U_s 9.1 km/s.

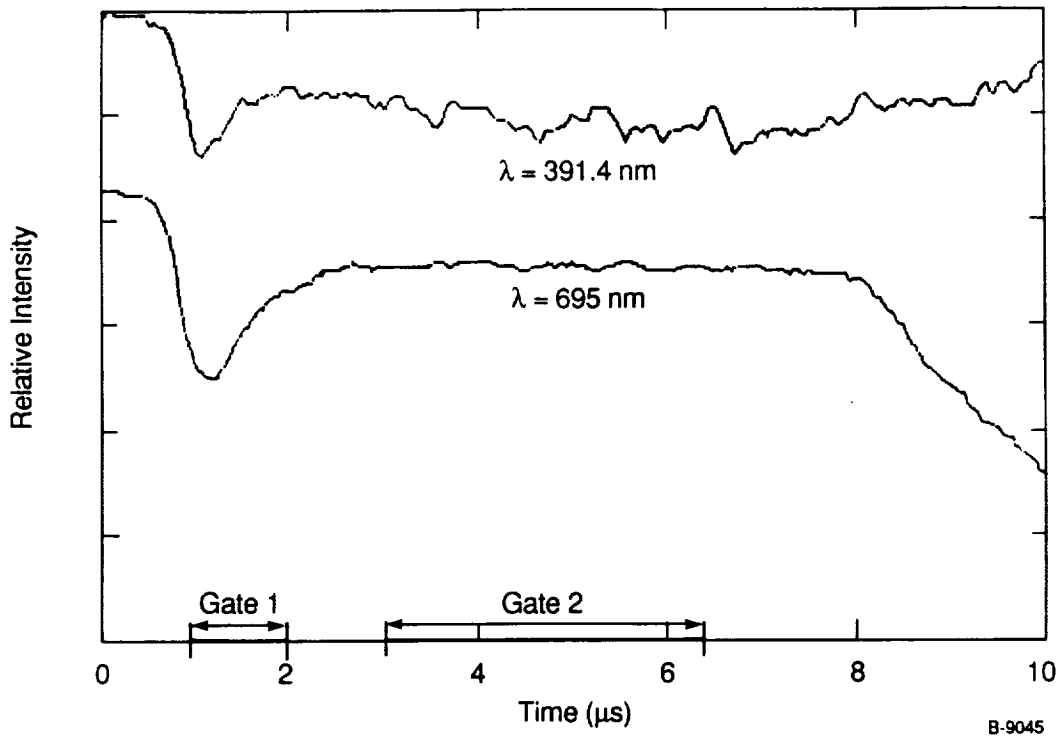


Figure 37. - Radiometers signal vs time for the 391.4 and 645 nm bands. Timing of OMA gates are shown. $P=0.1$ torr N_2 , U_s 12.1 km/s.

TABLE 12. RATIO OF PEAK NON-EQUILIBRIUM TO EQUILIBRIUM INTENSITIES.
 $P=0.1$ torr N_2

km/s	I_p/I_e , 391.4 nm	I_p/I_e , 645 nm
7.4	3.1	> 10
9.1	2.6	13
12.1	2.5	1.7

Lastly, it can be seen from the data at 12.1 km/s shown in Figure 37 that the 645 nm intensities in the non-equilibrium and equilibrium regions are quite close to each other, unlike the observations at lower velocities. This presumably results from the fact that a different radiation source, Kramers radiation or electron-ion bremsstrahlung, dominates the 645 nm radiation at these high velocities. This effect is seen in the variations of 645 nm intensity vs velocity as tabulated in Table 13. Here it is noted that although the peak non-equilibrium intensity flattens out with increasing velocity, the equilibrium intensity continues to rise. A similar analysis on the 391.4 nm radiation is not useful since the CN is a contaminant whose concentration can vary from run to run.

TABLE 13. RELATIVE INTENSITIES I_p, I_e AT 645 nm VS VELOCITY. $P=0.1$ torr N_2

U_s km/s	$I_p, \times 10^{-12}$ Photons/s	$I_e, \times 10^{-12}$ Photons/s
7.4	0.4	~0.0
9.1	1.3	0.1
12.1	1.4	0.8

One last point on Figures 35 through 37. The trigger points and gates for the OMA's are shown at the top of each figure. This provides a clear relationship between the radiometric traces and the OMA's which provide spectral information, time integrated over the gate width. As can be seen our triggering system worked well allowing us to clearly delineate between the equilibrium and non-equilibrium portions of the shocked gas history. The OMA data are described in the next section.

There are two interesting parameters of the non-equilibrium shock radiation which have previously been used by AERL to quantify the characteristic times for the non-equilibrium chemistry. These parameters are t_p , the measured time between passage of the shock front and the peak of the radiation signal, and $t_{0.1}$, which is the observed time between passage of the shock front and when the intensity approaches 1.1 times its equilibrium value. These definitions are shown as an inset in Figure 38. It should be remembered that these are laboratory times and much shorter than the particle times under which the gasses are being shock processed. This is because the gasses move behind the shock front and thus have a large velocity relative to the observation station. These laboratory times can be converted to particle times for kinetic analysis through standard techniques.

The earlier AERL evaluation of these parameters was apparently performed using wideband radiometers. We have evaluated these characteristic times using our full radiometric data base and find small variations from wavelength to wavelength. It appears in many cases that the times evaluated from the 391.4 nm radiometer are slightly larger than those evaluated from the other radiometers, perhaps reflecting kinetic differences. The characteristic times observed in the present data base are compared with the AERL data in Figure 38. The agreement is reasonable given the scatter in both data bases. One interesting feature is that the characteristic times do not continue to decrease with velocity out to 12 km/s as implied in the AERL analysis. Indeed the differences between the PSI data at 9.1 and 12 km/s are not large and certainly within the experimental scatter. Note that most of PSI's data is for N_2 while the AERL data base is for air. The observed difference in kinetic times for these two gasses does not appear to be significant. However, it must be remembered that these observations are primarily for visible radiation and the phenomenology could be quite different in the ultraviolet.

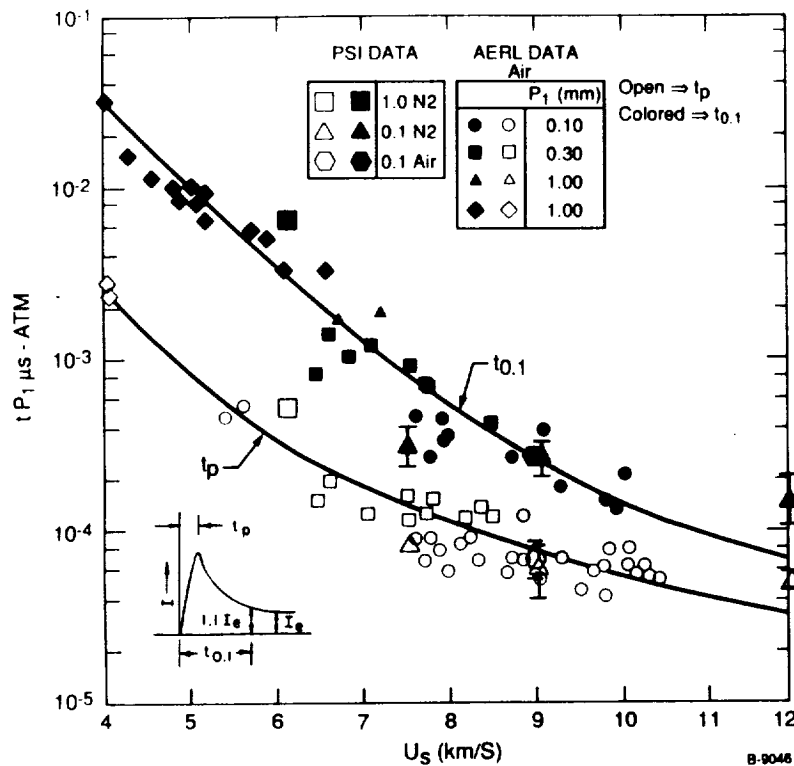


Figure 38. - Observed values of t_p and $t_{0.1}$ from the present measurements contrasted with the earlier AERL data. Original figure from ref. 4.

3.2 OMA Spectral Analysis

We have generated a total of sixteen OMA spectra, corresponding to the equilibrium and non-equilibrium regimes of eight shock tests. The test conditions are summarized in Table 11 and the full data base is presented with comments in Appendix C. A total of six spectra have been analyzed in some detail and the results of that analysis are presented below.

The analysis of the spectral data was accomplished using the PSI spectral fitting codes, which are now installed at NASA Johnson Space Center. These codes generate high resolution emission spectra for each emitting state at a specified rotational temperature. These spectra are then convolved with the spectrometer spectral resolution function and fit to the spectral data, using a multiple linear regression routine. The data is response corrected within the routine using calibrations obtained from standard lamp spectra. We discuss the analysis of individual spectra below in order of increasing shock velocity.

3.2.1 Case A

Conditions: N₂, 1 torr, 5.8 km s⁻¹, non-equilibrium. This is a high resolution spectrum comprised of CN(B-X) and N₂⁺(B-X) $\Delta v = 0$ sequence bands (Figure 39). Also included in the fit is emission from the N⁺ 4s³P - 3p³P (designated NII41) transition at

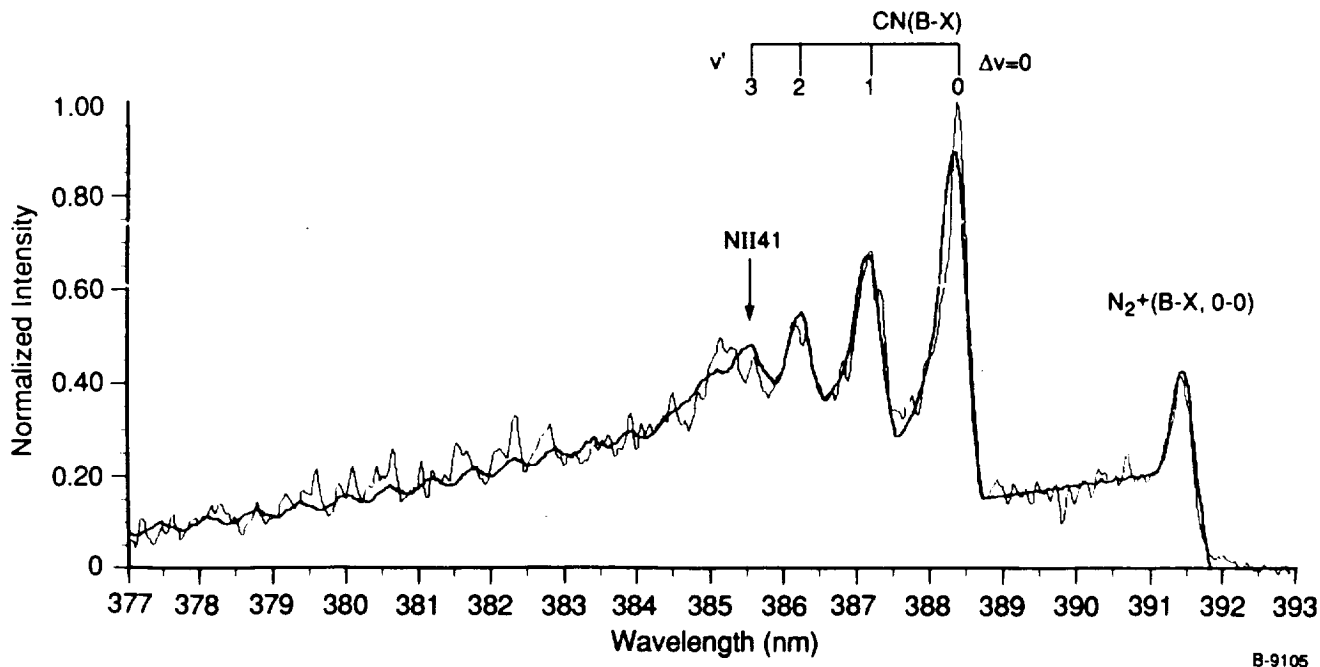


Figure 39. - Case A shock data and spectral fit.

385.1 nm. This transition is observed but not noted in the 6 km s^{-1} N_2 shock data of Sharma and Gillespie⁶. The relative populations of these states are $\text{N}_2^+(\text{B}):\text{CN}(\text{B}):\text{NII41} = 1.0:1.33:2.1 \times 10^{-3}$.

3.2.2 Case B

Conditions: N_2 , 1 torr, 6.1 km s^{-1} , non-equilibrium. This spectrum covers a broader range than Case A (Figure 40). In addition to CN and N_2^+ there are additional features from several N-atom transitions: N $2p^3p^2D - 2p^23s^2P$ at 410.68 nm (NI26), N $2p^24p^4P - 2p^23s^4P$ at 422.2 nm (NI29) and the N $2p^24p^4S - 2p^23s^4P$ at 414.6 nm (NI30). These lines were not observed by Sharma and Gillespie⁶ in their 6 km s^{-1} data but were seen by Sharma et al⁷ in their 10.2 km s^{-1} air data. Relative populations are $\text{N}_2^+(\text{B}):\text{CN}(\text{B}):\text{NI26}:\text{NI29}:\text{NI30} = 1.0:2.14:3.4 \times 10^{-2}:1.2 \times 10^{-2}:0.16$.

3.2.3 Case C

Conditions: N_2 , 0.1 torr, 7.4 km s^{-1} , non-equilibrium (Figure 41). This spectrum shows features attributable to the CN and N_2^+ (B-X) transitions as well as the NI26, NI29, and NI30 atomic lines. The strong feature at 337 nm is unambiguously assigned to the NH(A-X) transition and not the $\text{N}_2(\text{C-B})$ transition also found in this region. Relative populations are $\text{N}_2^+(\text{B}):\text{CN}(\text{B}):\text{NH}(\text{A}):\text{NI26}:\text{NI29}:\text{NI30} = 1.0:1.73:7.9:0.08:1.3 \times 10^{-2}:0.2$.

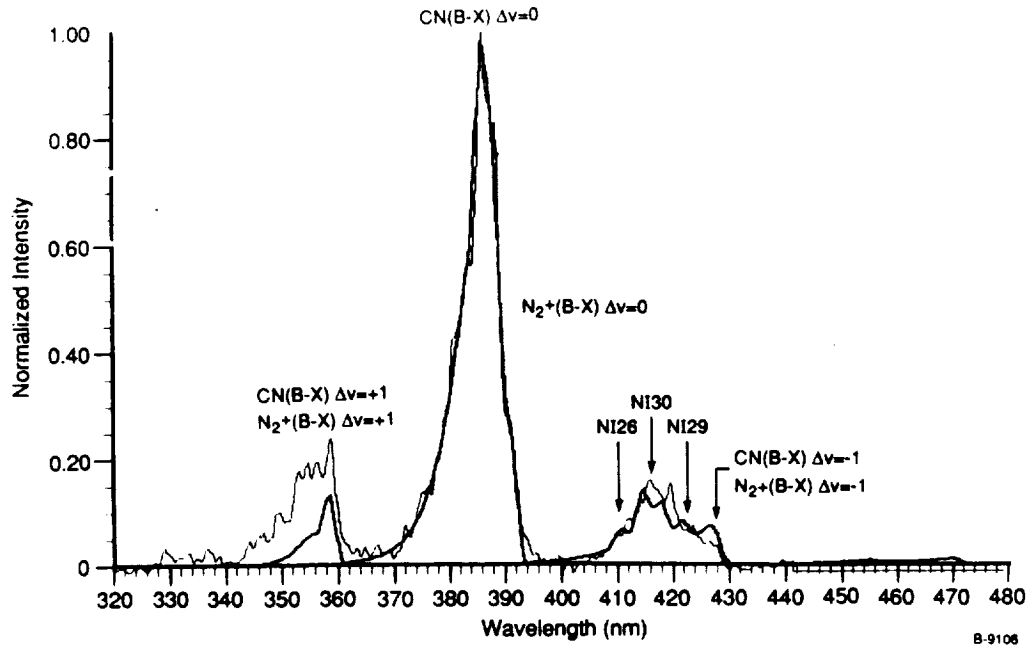


Figure 40. - Case B shock data and spectral fit.

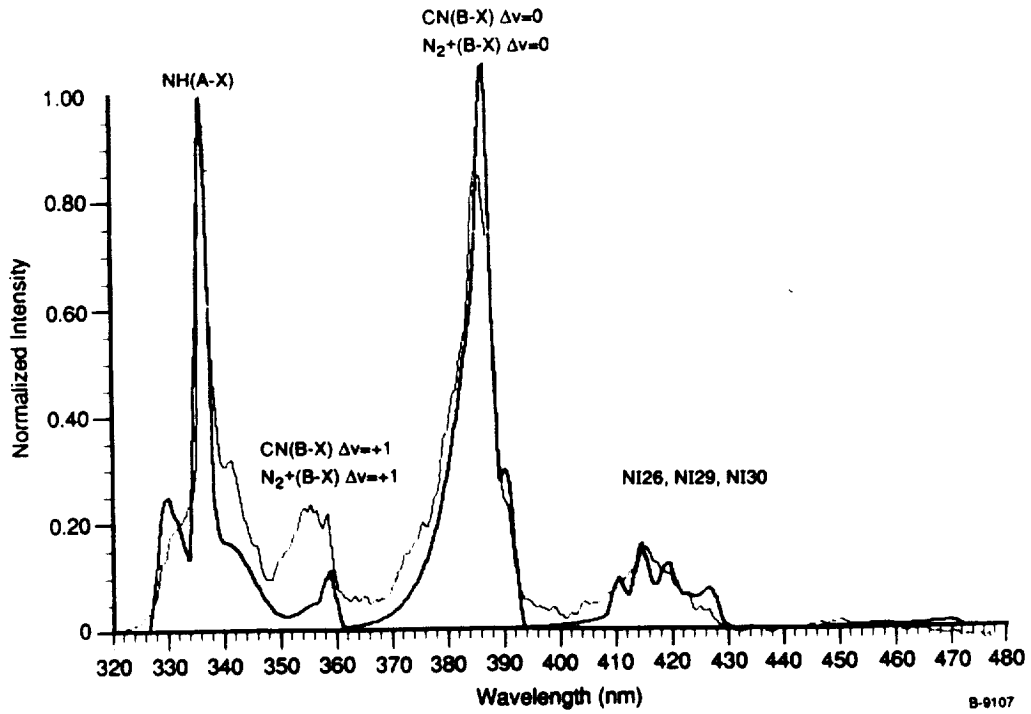


Figure 41. - Case C shock data and spectral fit.

3.2.4 Case D

Conditions: N_2 , 0.1 torr, 9.1 km s^{-1} , equilibrium (Figure 42). Spectrum is quite similar to Case A data with inclusion of doublet atomic lines near 393.5 nm. These are tentatively assigned to transitions in iron or cobalt and are from the tube walls. Relative populations for this spectrum are $N_2^+(B):CN(B):NII41 = 1.0:8.1:1.3 \times 10^{-3}$.

3.2.5 Case E

Conditions: Air, 0.1 torr, 9.4 km s^{-1} , non-equilibrium (Figure 43). Data shows features previously noted in above spectra with inclusion of atomic oxygen emission at 393 and 397 nm and a small feature at 337 nm which could be either $N_2(C-B)$ or $NH(A-X)$ emission features. These features were also observed by Sharma et al.⁷ in air at 10.2 km s^{-1} but not assigned. $N_2^+(B):CN(B):N_2(C-B) = 1.0:3.3:0.2$.

3.2.6 Case F

Conditions: N_2 , 0.1 torr, 12 km s^{-1} , non-equilibrium (Figure 44). All species previously observed in lower velocity shocks are present in the data. At this velocity underlying free-bound radiation is observed in the data. This component of the emission is removed empirically to enable fitting the molecular and atomic emission features cited. Relative populations are $N_2^+(B):CN(B):N_2(C):NI26:NI29:NI30 = 1.0:1.37:0.18:0.33:7.9 \times 10^{-3}:0.22$.

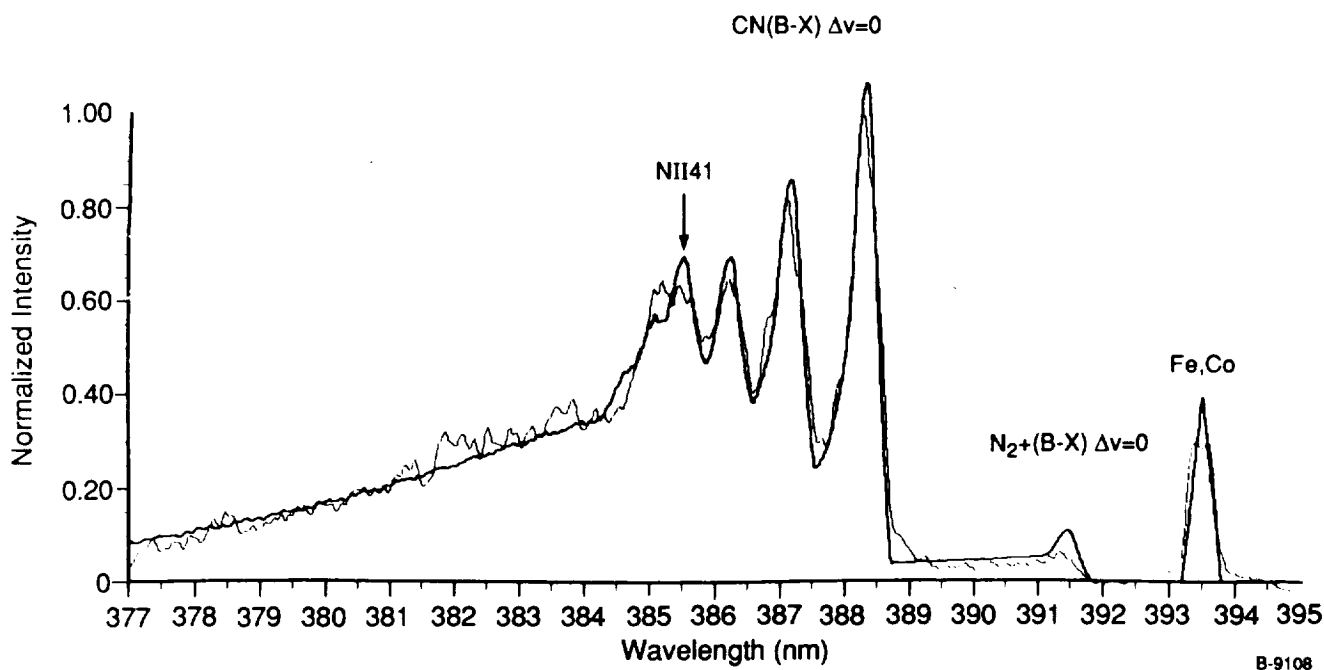


Figure 42. - Case D shock data and spectral fit.

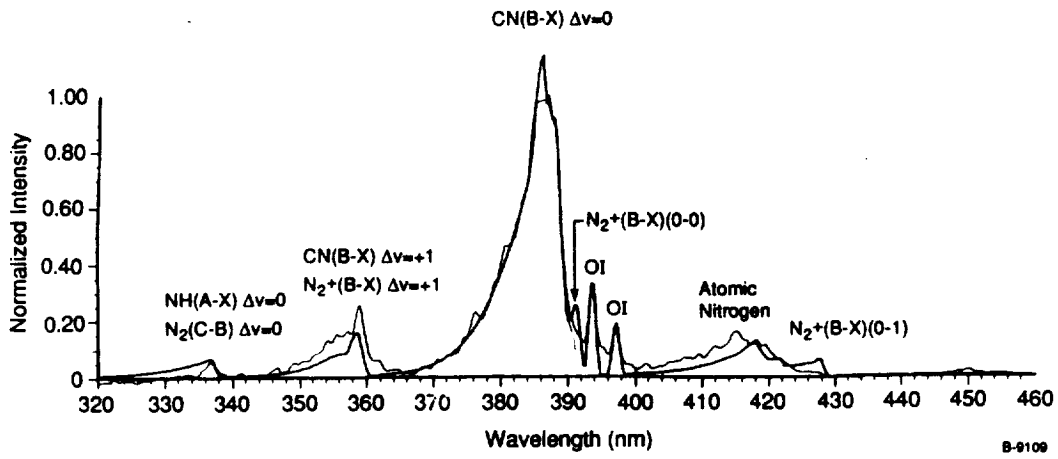


Figure 43. - Case E shock data and spectral fit.

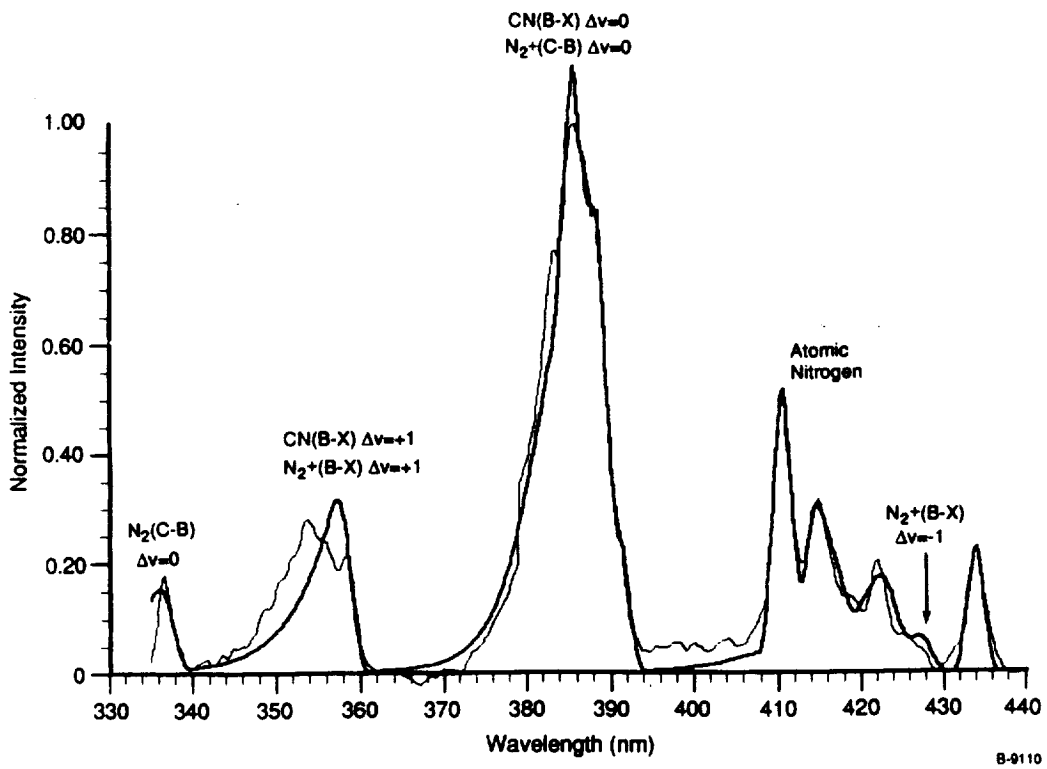


Figure 44. - Case F shock data and spectral fit.

4. SUMMARY

We have built and made operational a 6 in. electric arc driven shock tube which allows us to study the non-equilibrium radiation and kinetics of low pressure (0.1 to 1 torr) gasses processed by 6 to 12 km/s shock waves. The diagnostic system allows simultaneous monitoring of shock radiation temporal histories by a bank of up to six radiometers, and spectral histories with two optical multi-channel analyzers.

A data set of eight shots was assembled, comprising shocks in N_2 and air at pressures between 0.1 and 1 torr and velocities of 6 to 12 km/s. Spectrally resolved data was taken in both the non-equilibrium and equilibrium shock regions on all shots. The AERL data base extended only to velocities of 10.5 km/s. The present data appear to be the first spectrally resolved shock radiation measurements in N_2 performed at 12 km/s. The data base has been partially analyzed with salient features identified.

The shock tube facility is presently operational although contamination levels require improvement. It should prove a useful tool to study this elusive experimental regime.

5. REFERENCES

1. Allen, R.A., Camm, J.C., and Keck, J.C., "Radiation from Hot Nitrogen," AVCO Everett Research Lab., Everett, MA, Research Report 102, April 1961.
2. Allen, R.A., Camm, J.C., and Keck, J.C., "Non-Equilibrium Radiation from Shock heated Nitrogen and a Determination of the Recombination Rate," AVCO Everett Research Lab., Everett, MA, Research Report 110, June 1961.
3. Allen, R.A., "Non-Equilibrium Shock Front Rotational, Vibrational, and Electronic temperature Measurements," AVCO Everett Research Lab., Everett, MA, Research Report 186, August 1964.
4. Allen, R.A., Rose, P.H., and Camm, J.C., "Non-Equilibrium and Equilibrium Radiation at Super-Satellite Reentry Velocities," AERL RR156, 1962.
5. Caledonia, G.E., Krech, R.H., Woodward, A., Foutter, R., and Rawlins, W.T., "Aerothermodynamic Radiation Studies-Final Report, PSI TR-851, August 1988.
6. Sharma, S. and Gillespie, W., "Non-equilibrium Shock Front Radiation Measurements," AIAA-90-0139, 28th Aerospace Sciences Meeting,, Reno, Nevada (1990).
7. Sharma, S., Gillespie, W., and Meyer S.A., "Shock Front Radiation Measurements in Air," AIAA-91-0573, 29th Aerospace Sciences Meeting,, Reno, Nevada (1991).
8. Dannenberg, R.E. and Silva, A.F., "Arc Driver for Either Efficient Energy Transfer or High Current Generation," AIAA J.10(12), 1563-4 (1972).
9. Dannenberg, R.E., "A Conical Air Driver for High Energy Test Facilities," AIAA J.10(12), 1692-4 (1972).
10. Dannenberg, R.E. and Slapnicar, P.I., "Development of Dynamic Discharge Arc Driver with Computer Aided Circuit Simulation," AIAA J.14(9), 1183-8 (1976).
11. Sharma, S. and Park, C., "Operating Characteristics of a 60 and 10 cm Electric Air-Driven Shock Tube - Part 1: The Driver," J. Thermophys. 4 3 (1990).

APPENDIX A Driver Testing Procedures

The following procedure was followed during assembly and testing of the electric arc driver system.

A.1 Vacuum/Pressure Integrity

The first step is to assemble the drive chamber more-or-less completely, either in its final position on the face of the capacitor bank or on the bench (complete assembly will require some blocking of the hot electrode if it is conducted without benefit of the current delivery plates). A vacuum should be pulled on the system and both vacuum level and holding time after the pumps are turned off should be measured.

Next, gas pressure should be valved into the chamber up to 2 bars (absolute). The pressure source should be cut off and gas holding integrity should be checked. If possible, this test should be run with helium since it is the most difficult gas to contain. After the chamber has passed the pressure test, gas pressure may be increased slowly until the diaphragm ruptures. Pressure required to rupture the diaphragm should be checked against computed values. The chamber should then be disassembled carefully and the remaining severed diaphragm annulus should be examined to be sure the diaphragm broke properly. If all these tests are successful, the vacuum/gas/diaphragm integrity of the driver has been demonstrated.

Of course the driver was separately hydrostatically tested to ensure safe operation at peak operating pressure.

A.2 Hi-Pot Test

The driver chamber assembly should be reassembled in its final position on the face of the capacitor bank and it should be aligned carefully with the shock tube. The collection plates for the capacitor bank should be installed in their final configuration with insulators in place, but the copper discs connecting the capacitors to the hot plate should not be installed. Instead, the capacitor grounding system should be installed in its entirety. A new diaphragm should be installed at the face of the driver chamber and the chamber should be charged to approximately 2 bars (absolute) with whatever driver gas is to be used for early experiments (helium). Personnel should be cleared from the area of the room containing the capacitor bank. The charging circuit for the bank should be engaged and the bank should be charged by applying electrical power to its hot plate. Voltage should be allowed to raise on the hot plate to the lesser of 25 KV or to the highest voltage available. Once 25 KV has been reached, lights in the room should be turned off except for a dim residual that allows people with dark adapted eyes to just see the bank clearly. The bank (with full voltage applied) should be inspected from all sides to note where light-emitting corona discharges are most intense. Should any of these points be immediately adjacent to insulation, their positions must be noted before the bank is shorted to ground. Under no circumstances should the hot

plate be left charged for over 30 min. After the bank has been shut-down and safely shorted to ground, the points where bright blue light was observed adjacent insulators should be examined. Sharp edges should be sanded smooth and round, and the fillings should be removed carefully. The charging process should be repeated for as many times as is necessary to eliminate corona immediately adjacent the insulation. The voltage integrity of the capacitor hot plates and the shock tube driver assembly are verified once this test has been conducted successfully.

A.3 Capacitor Discharge Parameters

The front face of the driver chamber should be opened after gas is vented from it and the triggering assembly should be removed from the center of the hot electrode. A thin, stiff wire should be passed through the hole in the central copper electrode from the chamber to the electrode cavity. A length of nylon thread (medium to heavy diameter) should be tied between the end of the wire and the front face of the trigger assembly. The strings should be 4 to 6 in. long. The trigger assembly may now be reinstalled in the hot electrode while the wire is withdrawn forward through the hot electrode face. Be sure to maintain gentle tension on the string during the entire probe insertion process. The string should stick out into the chamber somewhat more than 2.5 in. when the plunger of the air cylinder is in its forward position. The wire should be wrapped around a segment of 0.5-in. wide ground braid so that the end of the ground braid is approximately 2.25 in. from the forward end of the hot electrode. The ground braid should be rooted against the side of the teflon sleeve at about midpoint within the chamber with enough slack available to allow the firing solenoid to draw the end of the braid conveniently against the hot electrode. The other end of the braid should be led along the cylinder wall to the contact point where a few strands of it are fixed to the ground contact. The chamber may now be reassembled without a diaphragm in place. All of the copper discs used to connect the hot posts of the capacitors to the hot plate should now be installed after the capacitor grounding system has been removed. The capacitor bank charging and discharging system should now be disconnected from the hot plate. A source of approximately 10V DC should be connected between the hot plate and the ground plate through a 10.0 K ohm resistor. This resistor will charge the bank to +10 V with a time constant of 6.4s. An oscilloscope capable of observing single sweep traces at rates up to 10 ms/cm should be connected between the hot plate and ground plates. The oscilloscope should be set to observe frequencies between 14 and 40 KHz (10 ms per centimeter should be used if a conventional CRT scope is chosen). Vertical sensitivity of 5 V per centimeter is appropriate. A plastic rod should be affixed to the "loose end" of the ground braid so that it may be brought into contact with the hot electrode by hand.

The oscilloscope should observe the "ring down" of the bank when the charged bank is discharged with the copper braid. This experiment can be repeated after the shorting braid has been disconnected for at least 30s (4-3/4 time constants). The resulting oscillogram should be measured to determine the period of the oscillations if the bank oscillates freely (ratio of adjacent oscillation amplitudes is greater than 0.5. The angular frequency of the oscillation, ω , may be calculated using Eq. (A-1).

$$W = 1/2\Pi P \quad (A-1)$$

where P = bank ringing period. The internal inductance of the capacitor bank and the driving circuit may now be estimated using Eq. (A-2)

$$L = W^2/C \quad (A-2)$$

where C = bank capacitance = 624 uf. The critical damping resistance, R_c , for the discharge circuit may not be calculated through use of Eq. (A-3)

$$R_c = 2\sqrt{L/C} \quad (A-3)$$

We anticipate that the total resistance of the discharge circuit will be near $R_{tot} = 6 \times 10^{-3}$ ohm. This value should be used with R_c to calculate the critical discharge damping factor, n, as presented in Eq. (A-4)

$$n = R_{tot}/R_c \quad (A-4)$$

A fictitious maximum I_{omax} may now be calculated for the discharge circuit using Eq. (A-5)

$$I_{omax} = V\sqrt{C/L} \quad (A-5)$$

where V = bank charging voltage. I_{omax} is the current that would be achieved if a discharge were accomplished with zero electrical resistance in the discharge circuit. Equation (A-5) is derived by equating the energy stored electrostatically in the capacitors with the energy stored magnetically when current is following through the discharge circuit inductance.

The maximum current to be anticipated during an actual firing is determined by reference to Figure A-1 which is a plot of the ratio I_{max}/I_{omax} versus m for a damped harmonic oscillator.

Completion of this series of three tests and the accompanying analysis is sufficient for commissioning the facility for full-up operation.

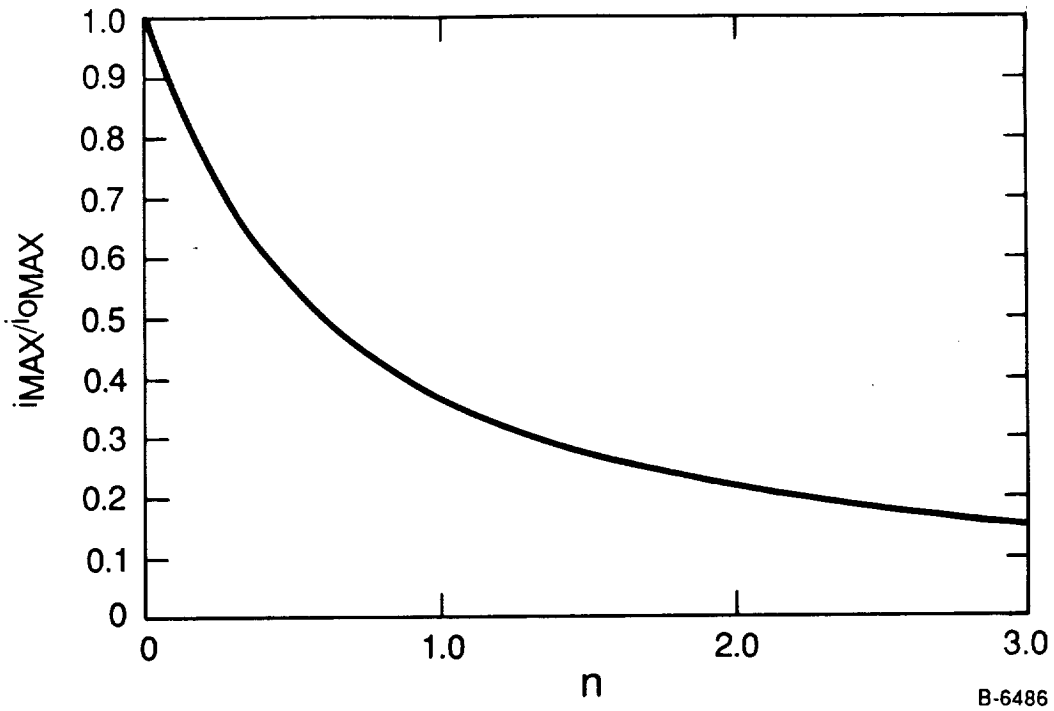


Figure A-1. - Ratio of the first current maximum (for arbitrary n) to the first current maximum (for $n = 0$) versus n .

APPENDIX B

Boundary Layer Estimates

Since our goal is to make absolute, quantitative emission measurements, it is desirable that the radiation we measure be emitted by gas in a well-defined and uniform state. Among other requirements, this means that the measurements must not be obfuscated by the presence of a large boundary layer. In this experiment we must consider two boundary layers, one growing unsteadily in the tube side wall and one steady on the surface of the boundary layer stripper plates in the tube test section. This stripper is used specifically to avoid data inaccuracies caused by the potentially large, unsteady boundary layer in the tube side wall. It consists of a 3-in. square frame supported in the test section on wedge-shaped supports. The windows are mounted flush with the interior surface of the stripper with their outer surfaces open to the room through cylindrical passages inside the supporting wedges. The leading edge of the stripper is sharp and the windows are 3-in. from the leading edge.

Let us deal just with the steady, compressible, cold-wall, constant edge condition boundary layer on the boundary layer stripper. Using the test conditions shown in Table B-1, which corresponds to the highest shock velocities we envision operating at, we have made estimates of the boundary layer characteristics using the high temperature viscosity data of Yos¹ and the boundary layer methodology of Dahm, et al.². The results are shown in Table B-2. Note that the calculated laminar momentum thickness Reynolds numbers are above the transition values given by both the venerable correlations Re_{θ} (at transition)/M = 150 and the transition correlation quoted by Dahm et al.³

Thus we have calculated the turbulent momentum and boundary layer thicknesses as shown in Table B-2. In all cases the momentum thickness is small with respect to the test section half height of 1.5 in., as in the boundary layer thickness except at the lowest pressure. The energy thickness, the best measure of thermal non-informities, lies between the momentum and boundary layer thickness and is generally much closer to the former. Thus it appears that perturbation due to the boundary layer on the stripper are small.

Turning to the issue of the growth of the unsteady boundary layer in the driven section wall, we again use the conditions shown in Table 1 and the results of Mirels.² For the given shock Mach numbers, we can compute for all conditions an upper bound in the boundary layer thickness of 0.6 in. Since the thermal boundary layer cannot be larger than the boundary layer, we conclude that all of the tube wall viscous effects are confined to a region outside the boundary layer stripper, as was intended, and cannot influence our radiation measurements.

TABLE B-1. CALCULATED SHOCK TUBE PERFORMANCE: INITIAL PRESSURE, 1 torr

	T(K)	P(atm)	ρ (g/cc)	H(erg/g)	Z (mole)	US, USR (cm/s)	US, U3 (cm/S)	pd (atm)
	2.700E+04	6.283E+00	2.434E-05	2.259E+12	3.265E+12	2.128e=06	1.997E+06	6.989E+02
MOL	N ₂ 2.611E-06	N 8.550E-01	N+ 1.025E+00	N++ 1.191E-01	N+++ 1.036E-06	N ₂ + 2.221E-06	E 1.265E+02	
M.F.	7.999E-07	2.619E-01	3.14E-01	3.664E-02	3.173E-07	6.802E-07	3.874E-01	
AMA	5.058E-08	1.665E-02	1.997E-02	2.329E-03	2.017E-08	4.324E-08	2.462E-02	

	T(K)	P(atm)	ρ (g/cc)	H(erg/g)	Z (mole)	US, USR (cm/s)	US, U3 (cm/S)	pd (atm)
	2.888E+04	6.283E+00	2.434e-05	2.259E+12	3.265E+12	2.128e=06	1.997E+06	6.989E+02
MOL	N ₂ 2.663E-08	N 2.293E-01	N+ 6.401E-01	N++ 1.130E+01	N+++ 1.898E-04	N ₂ + 3.898E-08	E 2.901E+00	
M.F.	5.433E-09	4.679E-02	1.306E-01	2.306E-01	3.872E-05	7.952E-09	5.920E-00	
AMA	5.058E-08	4.310E-04	1.203E-03	2.125E-03	3.567E-07	7.326E-11	5.454E-03	
	5.005E-11							

TABLE B-2. BOUNDARY LAYER IN STRIPPER PLATE AT WINDOW LOCATION

Initial Pressure (torr)	10	1	0.1
Laminar momentum thickness Reynolds Nos.	770	760	620
Turbulent momentum thickness (in.)	0.0065	0.0081	0.095
Turbulent boundary layer thickness (in.)	0.041	0.051	0.060

References

1. Yos, J., "Transport Properties of Nitrogen, Hydrogen, Oxygen, and Air to 30,000 K," Technical Memorandum RAD-TM-63-7, Avco Corporation, Wilmington, MA, March 1963.
2. Mirels, H., "Boundary Layer Growth Effects in Shock Tubes," Shock Tube Research, Proceedings of the Eighth International Shock Tube Symposium (Chapman and Hall, London, July 1971).
3. Dahm, T., Cooper, L., Rafinejad, S., Youngblood, S., and Kelly, J., "Passive Noretip Technology (PANT II) Program, Vol. I. Inviscid Flow and Heat Transfer Modeling for Reentry Noretips," SAMSO-TR-77-11, Acurex Corporation, Aerothermo Division, Mountain View, CA, October 1976.

APPENDIX C OMA Data Base

The OMA data base is presented in Figures C-1 through C-16. Data are shown in order of increasing velocity with both a non-equilibrium and equilibrium spectrum for each shock. It will be noted that there are several changes in spectral resolution, spectral region and OMA gate time throughout the data set. A selection of these spectra have been analyzed and discussed in the main text. Some general comments are provided below.

The first observation is that the CN violet bands centered at ~ 385 and ~ 355 nm are persistent contaminants at all velocities. This is commonly seen and we believe that the relative contribution of this system will decrease with continuing operation. Test results at the lowest velocity, ~ 6 km/s are shown in Figures C1-C4. Other spectral features seen are the N_2^+ (1-) system and perhaps the $N_2(2^+)$ system and some N/N^+ lines. Higher spectral resolution will be required to truly delineate these latter band systems. The high resolution data shown in Figure C-3 clearly evince features identifiable with both the N_2^+ (1-) and perhaps the $N_2(2^+)$ systems nested about the CN violet band. This data looks very similar to that reported by Sharma and Gillespie¹.

There is only one set of data at 7.4 km/s seen in Figures C5 and C6. Although the spectral features are generally similar to that seen at 6 km/s, a new band does appear at ~ 3360 . Although this is in the region of the $N_2(2^+)$ band we believe it is more likely impurity radiation due to NH. This particular structure only appears strongly in this data set.

Data for both nitrogen and air are shown for a velocity of ~ 9 km/s in Figures C-7 through C-12. Clearly the CN bands dominate the broad spectral surveys of Figures C-7 through C-9. Only the higher resolution data shows the underlying rich spectral features. Note that the high resolution equilibrium measurements in N_2 , Figure C-8, and air, Figure C-10, exhibit a high degree of correlation. Clearly, O_2 does not play a significant role in this spectral region. (The unidentified feature at 397 nm does correlate with an O-atom transition but it is unlikely that an oxygen impurity in N_2 would produce the same relative intensity level as the O_2 in air). The higher spectral resolution spectrum for the non-equilibrium region shown in Figure C-11 clearly demonstrates the richness of spectral detail in the data.

The data for the highest velocity studied, ~ 12 km/s, is shown in Figures C-13 through C-16. Here many of the spectral features correspond to atomic rather than molecular transitions. Furthermore, there is now apparent a significant underlying continuum, presumably due to Kramers radiation (bremsstrahlung). Note that these two runs were near repeats of each other. The equilibrium observations correlate favorably, however, the non-equilibrium results differ somewhat. In particular two sharp features seen between 390-400 nm in Figure C-15 are not observed in Figure C-13. These features line up with known oxygen atom transitions and could have resulted from an O_2 impurity in one of the tests.

References

1. Sharma, S.P. and Gillespie, W., "Non-equilibrium and Equilibrium Shock Front Radiation Measurements", AIAA-90-0139, 28th Aerospace Sciences Meeting, Reno, Nevada, 1990.

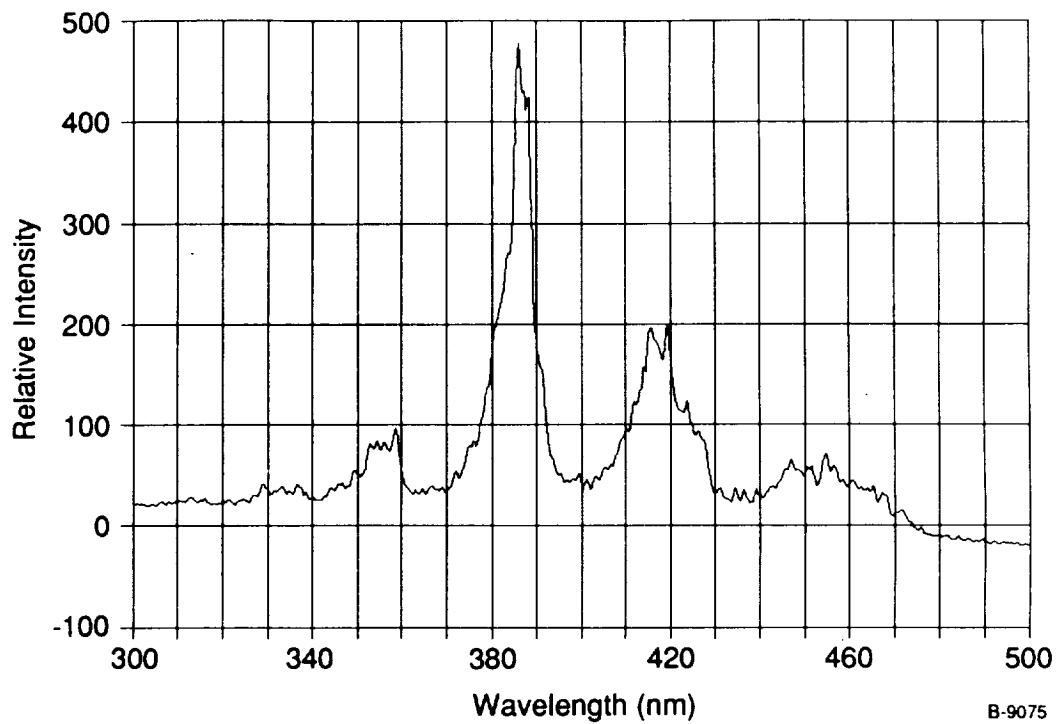


Figure C-1. Non-Equilibrium N_2 , $P_1=1$ torr, $U_s=5.8$ km/s, $1 \mu s$ gate, $\Delta\lambda=1.25$ nm.

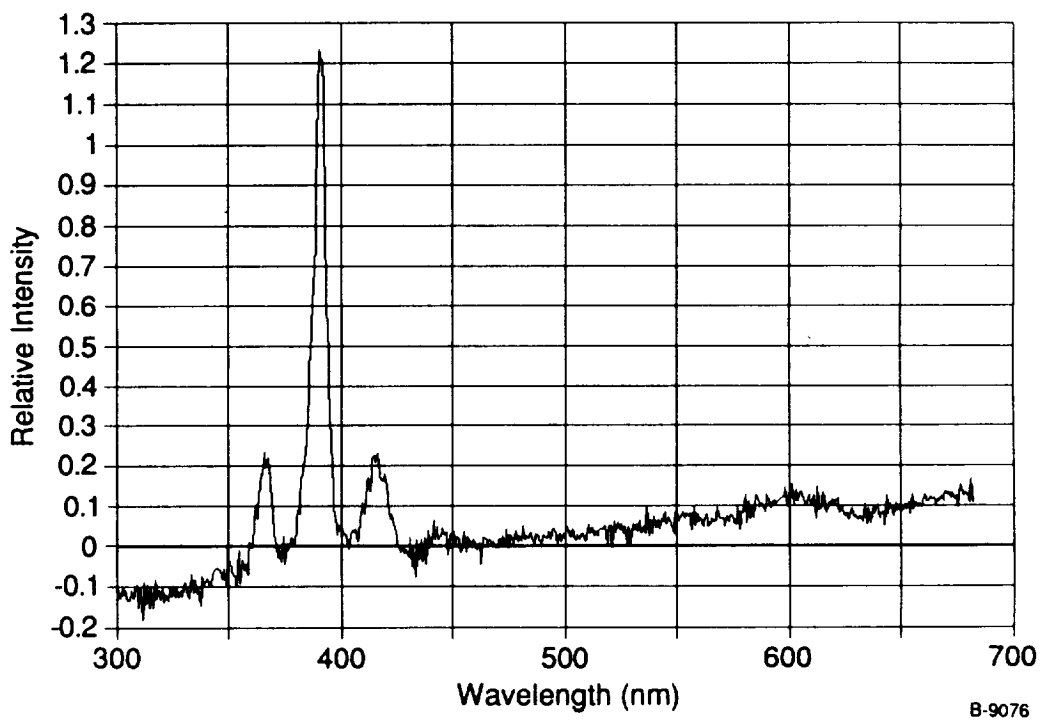


Figure C-2. Equilibrium N_2 , $P_1=1$ torr, $U_s=5.8$ km/s, $3.35 \mu s$ gate, $\Delta\lambda = 2.5$ nm. Apparent baseline problem.

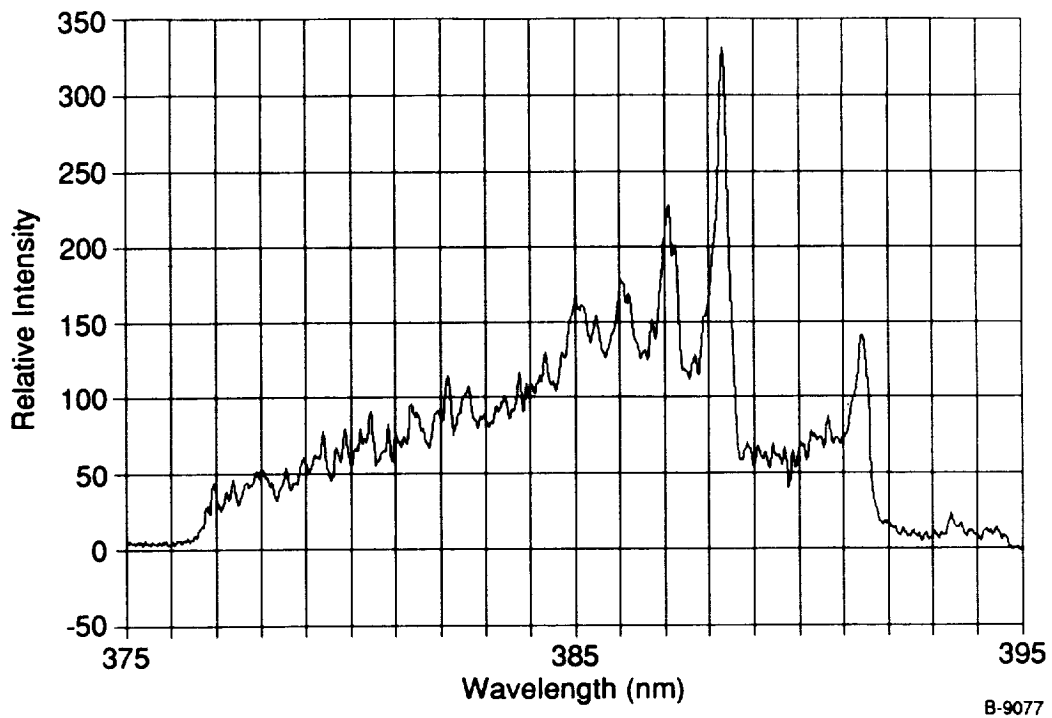


Figure C-3. Non-Equilibrium N_2 , $P_1 = 1$ torr, $U_s = 6.15$ km/s, $2 \mu s$ gate, $\Delta\lambda = 0.3$ nm.

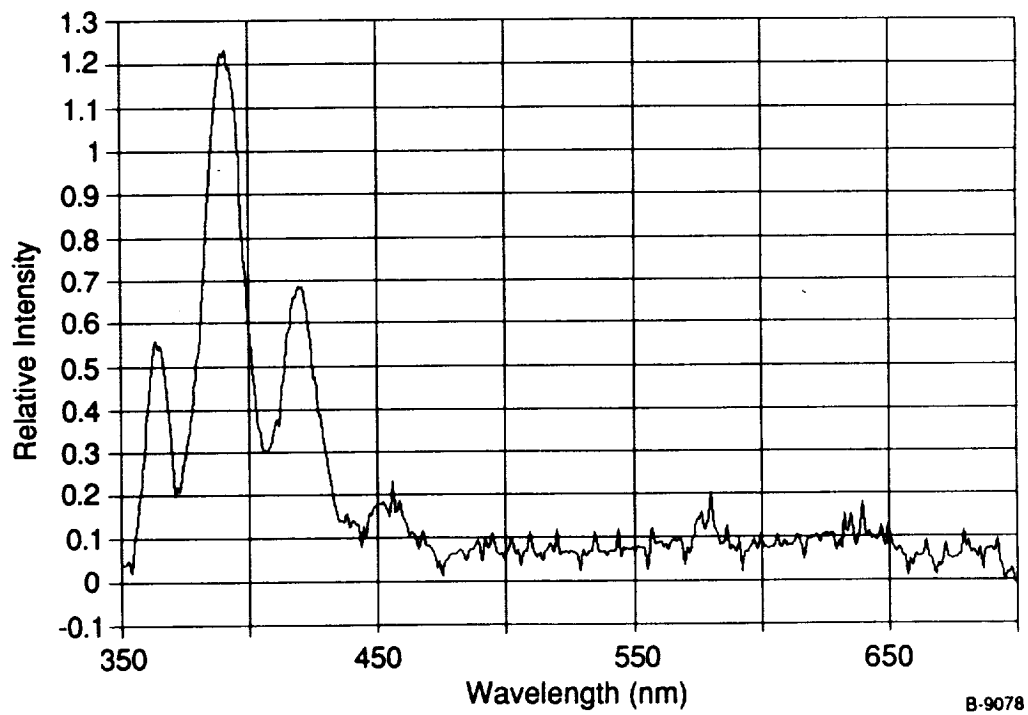
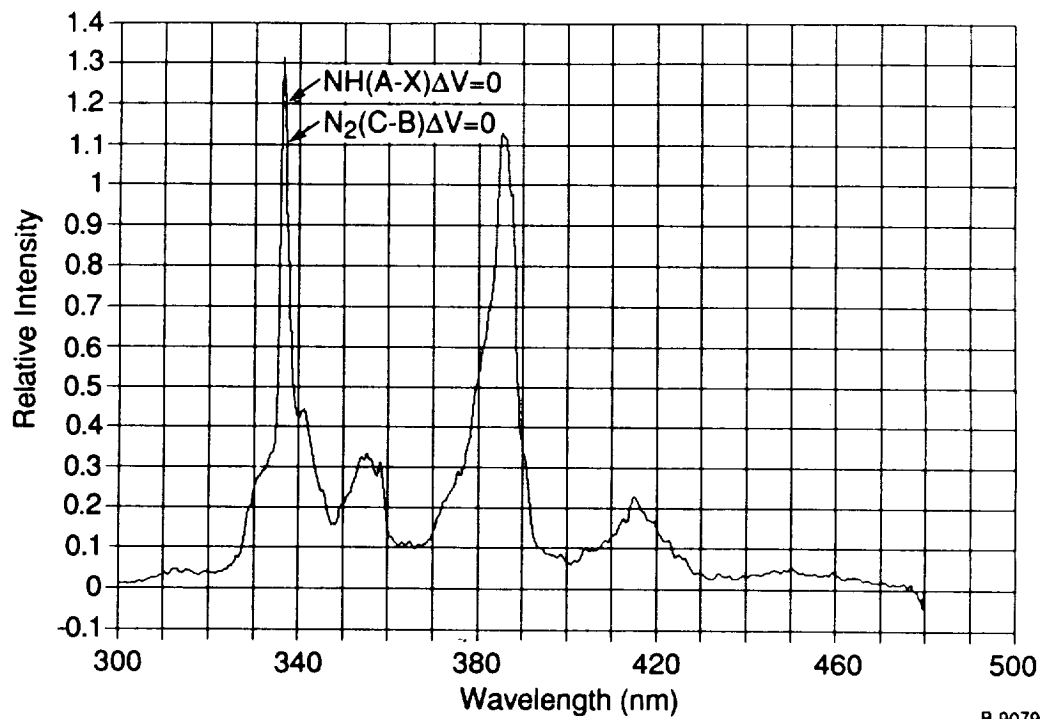
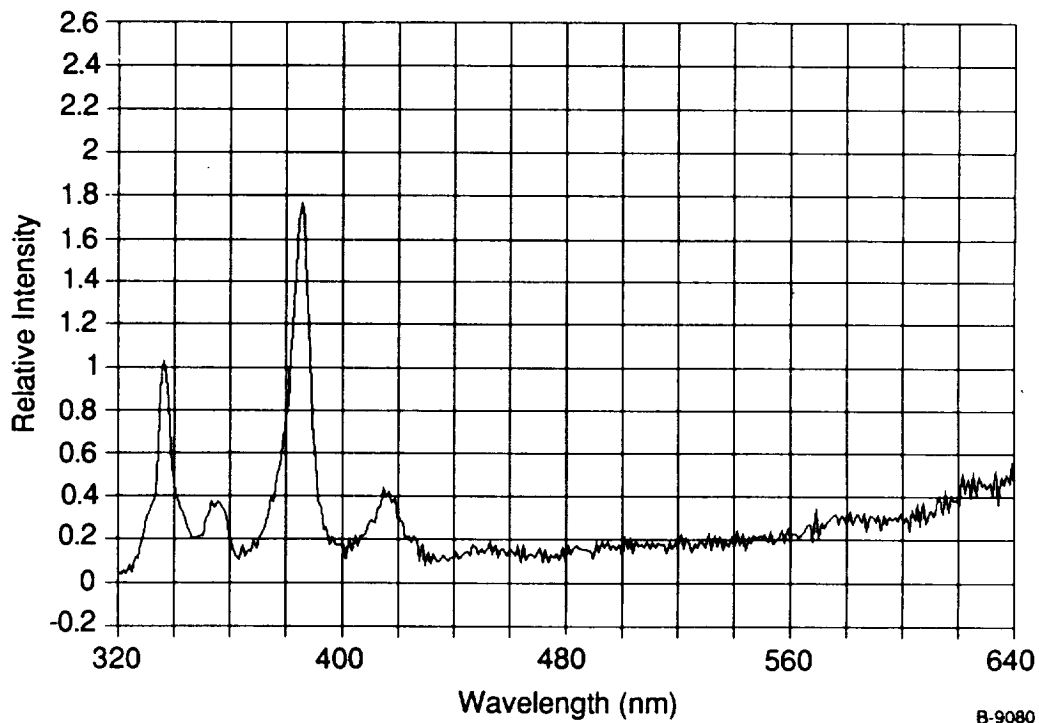


Figure C-4. Equilibrium N_2 , $P_1 = 1$ torr, $U_s = 6.15$ km/s, $10 \mu s$ gate, $\Delta\lambda = 10$ nm.



B-9079

Figure C-5. Non-Equilibrium N_2 , $P_1 = 0.1$ torr, $U_s = 7.4$ km/s, $1 \mu s$ gate $\Delta\lambda = 1.25$ nm.



B-9080

Figure C-6. Equilibrium N_2 , $P_1 = 0.1$ torr, $U_s 7.4$ km/s, $3.35 \mu s$ gate $\Delta\lambda = 2.5$ nm.

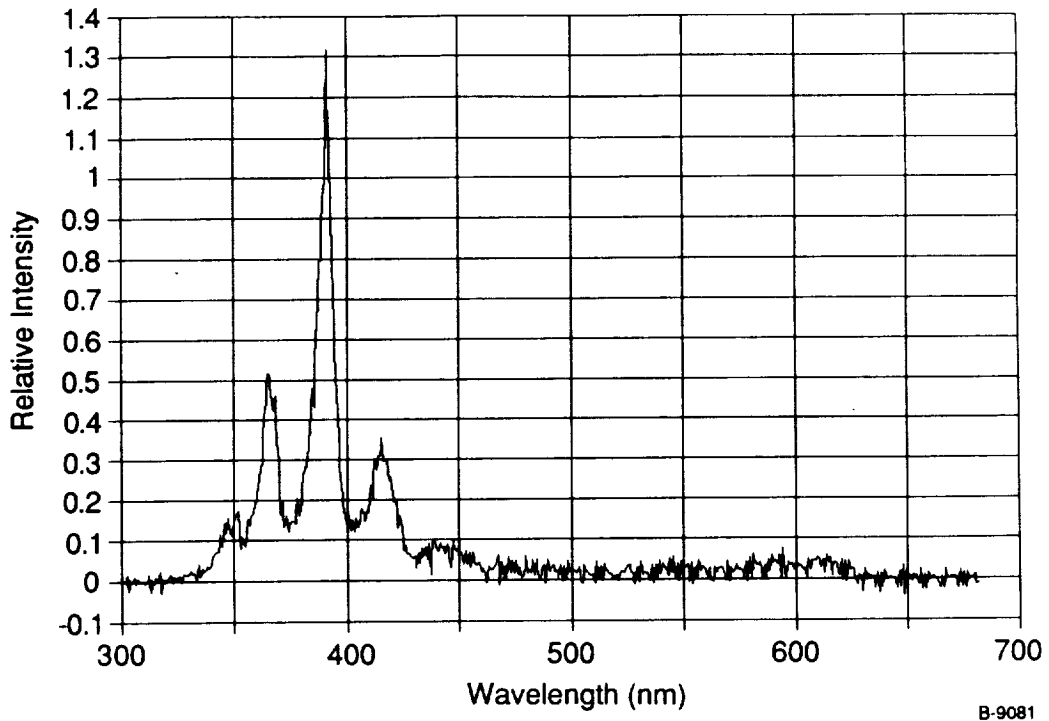


Figure C-7. Non-Equilibrium N_2 , $P_1 = 0.1$ torr, $U_s = 9.1$ km/s, $1 \mu s$ gate $\Delta\lambda = 0.47$ nm.

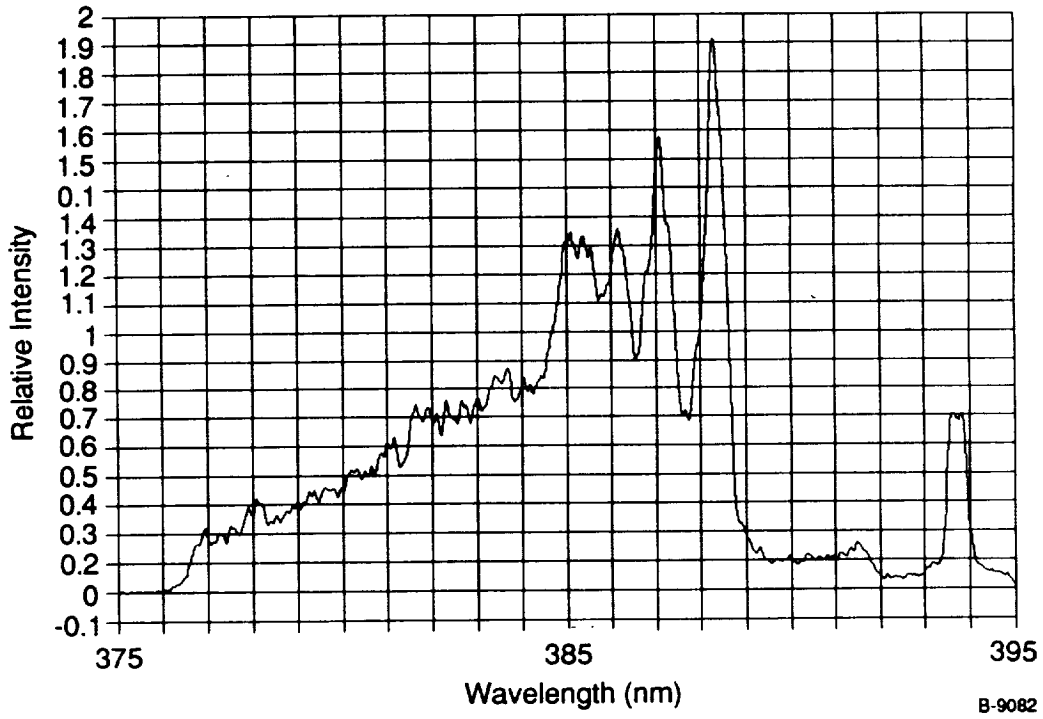


Figure C-8. Equilibrium N_2 , $P_1 = 0.1$ torr, $U_s = 9.1$ km/s, $3 \mu s$ gate, $\Delta\lambda = 1.0$ nm

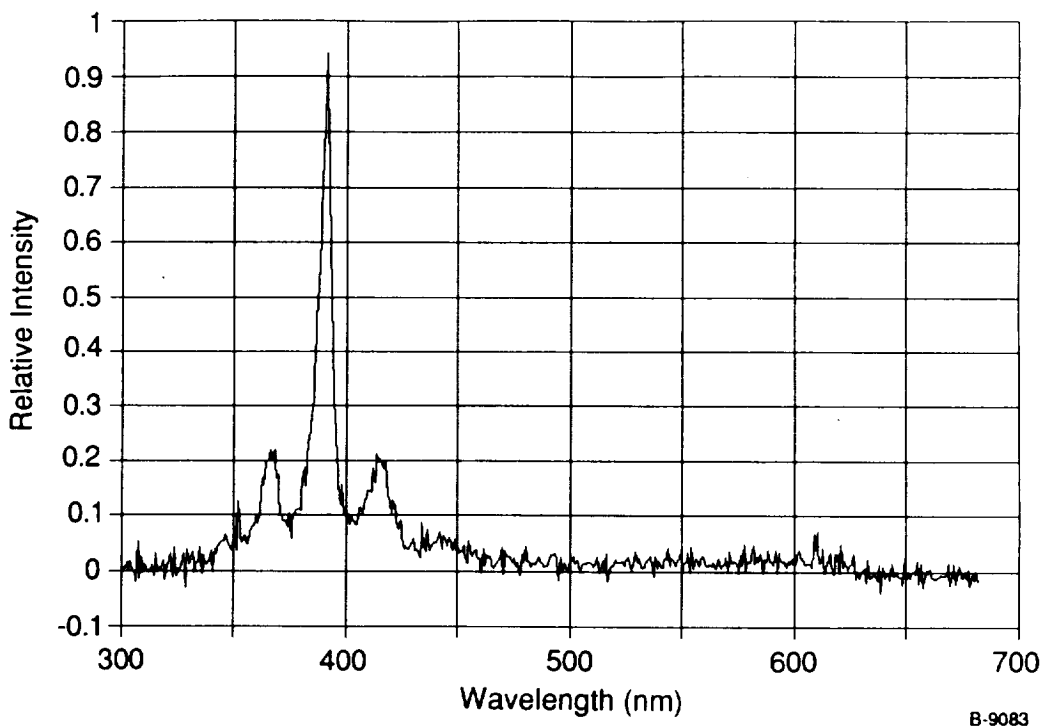


Figure C-9. Non-equilibrium air, $P_1 = 0.1$ torr, $U_s =$ km/s, $1\mu\text{s}$ gate, $\Delta\lambda=0.47$ nm.

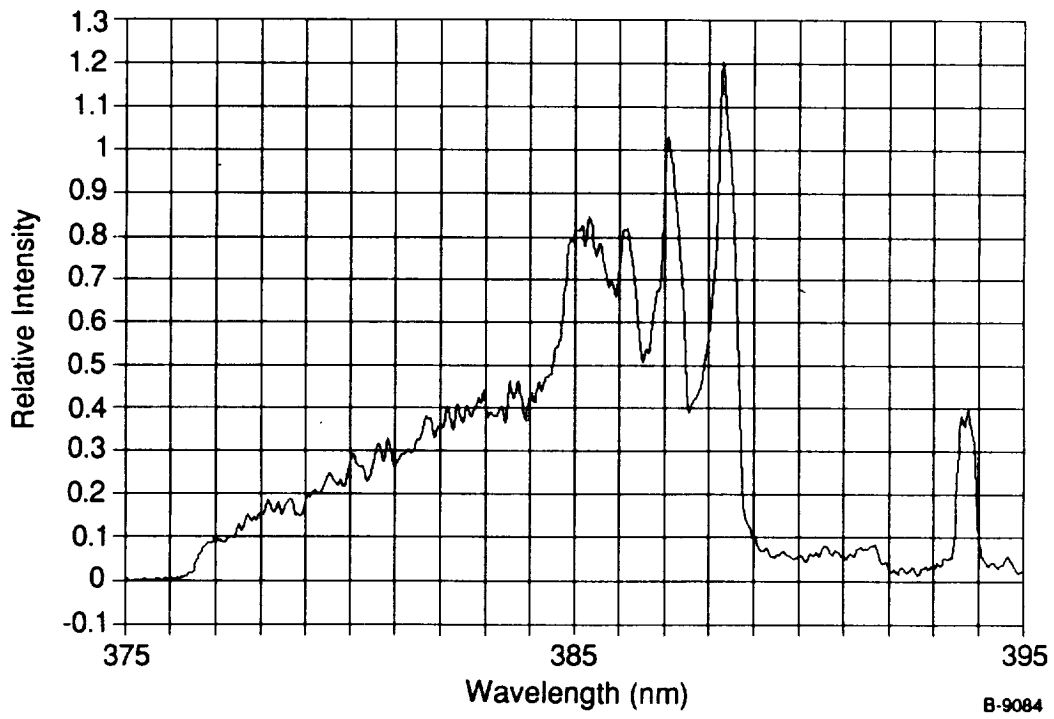


Figure C-10. Equilibrium air, $P_1 = 0.1$ torr, $U_s = 9$ km/s, $3.35\mu\text{s}$ gate, $\Delta\lambda=1.0$ nm.

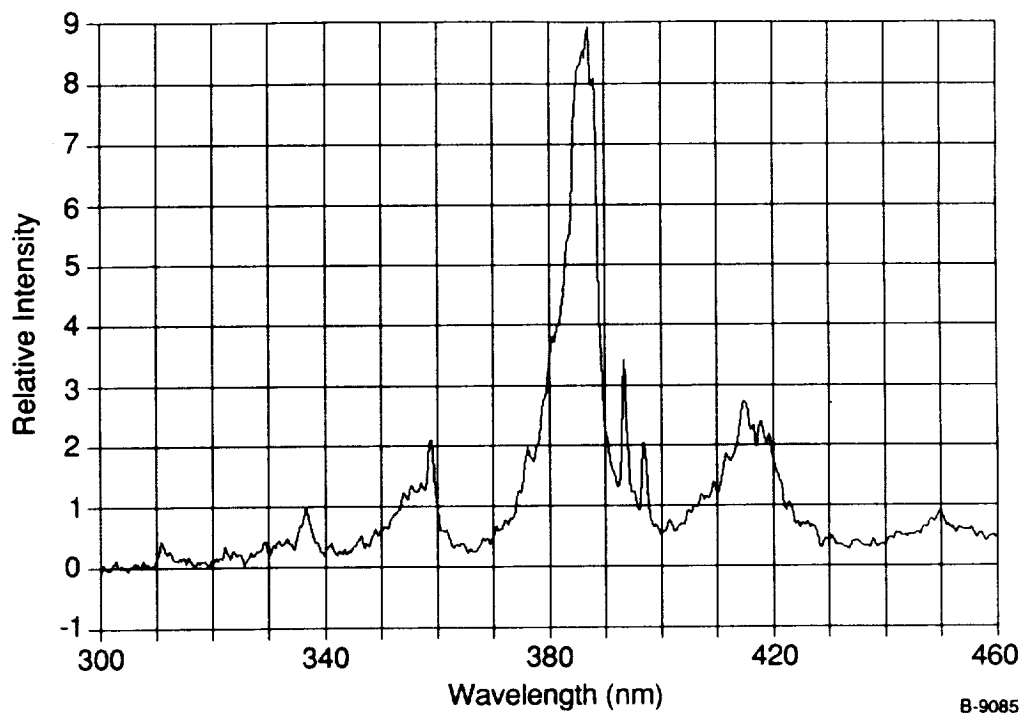


Figure C-11. Non-equilibrium air, $P_1 = 0.1$ torr, $U_s = 0.4$ km/s, $1 \mu\text{s}$ gate, $\Delta\lambda = 0.47$ nm.

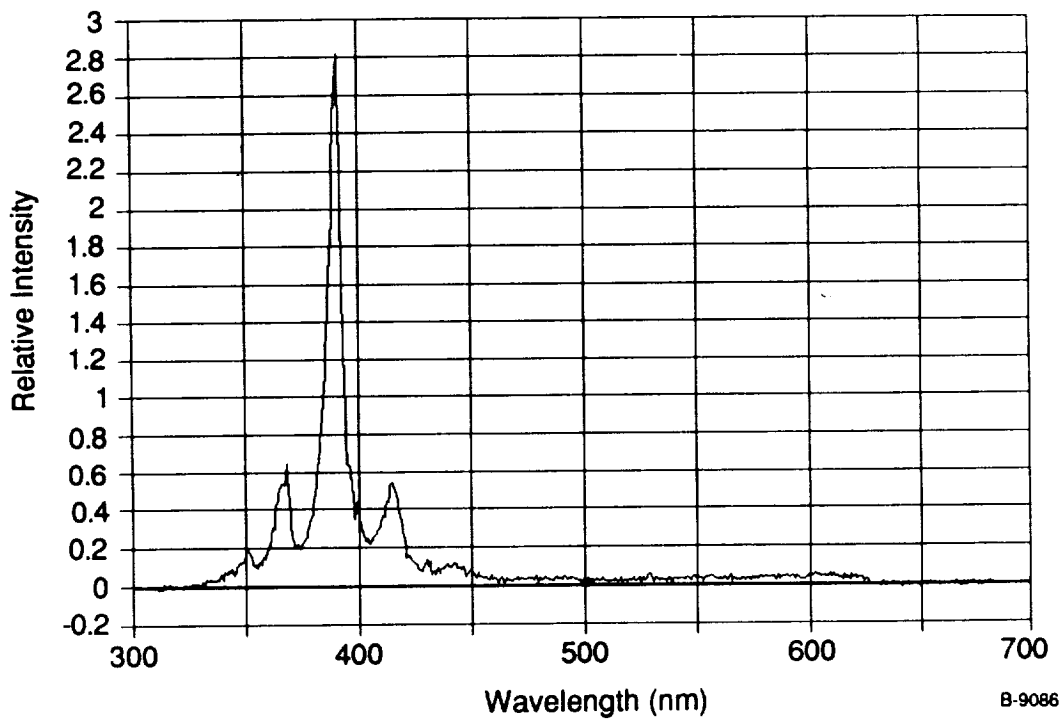


Figure C-12. Equilibrium air, $P_1 = 0.1$ torr, $U_s = 9.4$ km/s, $3.35 \mu\text{s}$ gate, $\Delta\lambda = 1.0$ nm

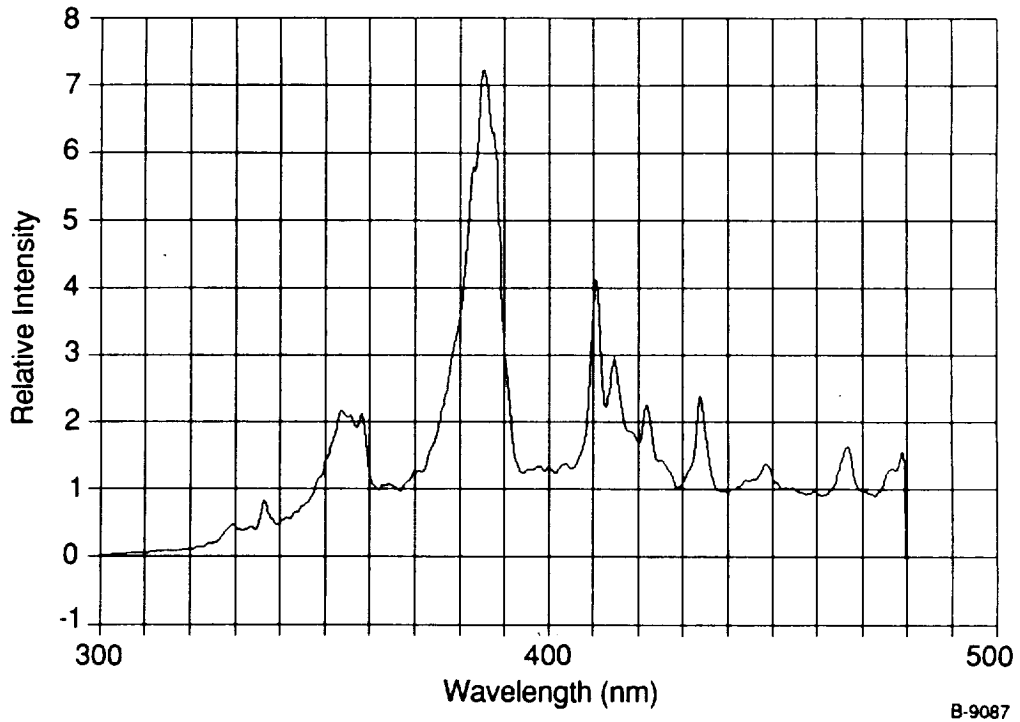


Figure C-13. Non-Equilibrium N_2 , $P_1 = 0.1$ torr, $U_s = 11.8$ km/s $1 \mu s$ gate, $\Delta\lambda = 1.25$ nm.

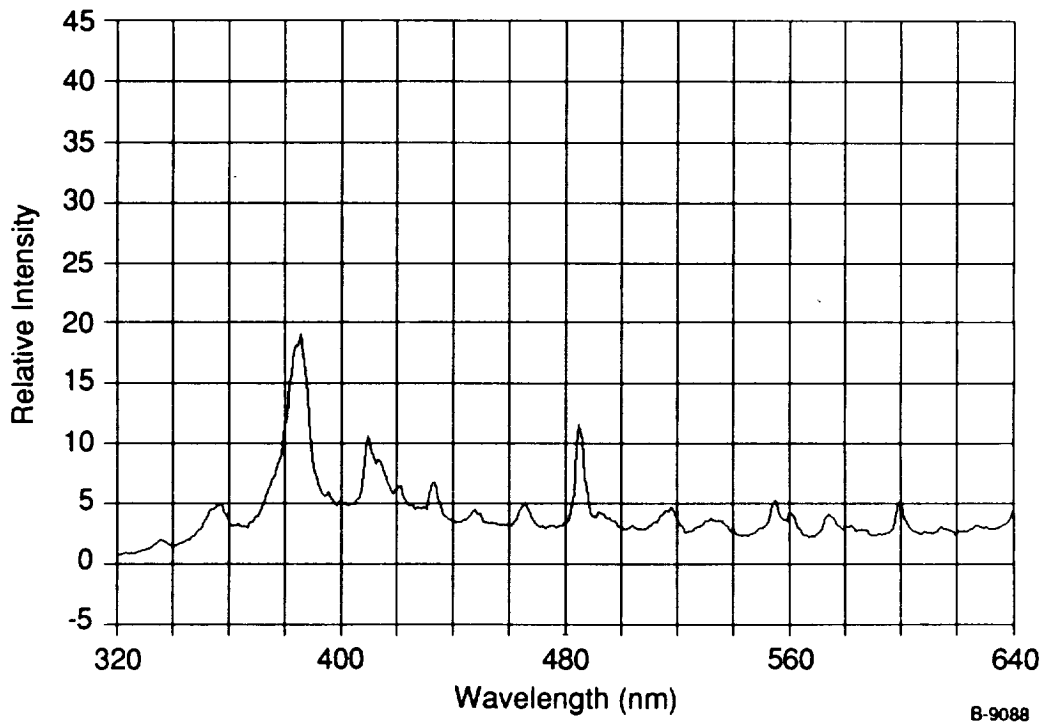


Figure C-14. Equilibrium N_2 , $P_1 = 0.1$ torr, $U_s = 11.8$ km/s, $3.35 \mu s$ gate, $\Delta\lambda = 25$ nm.

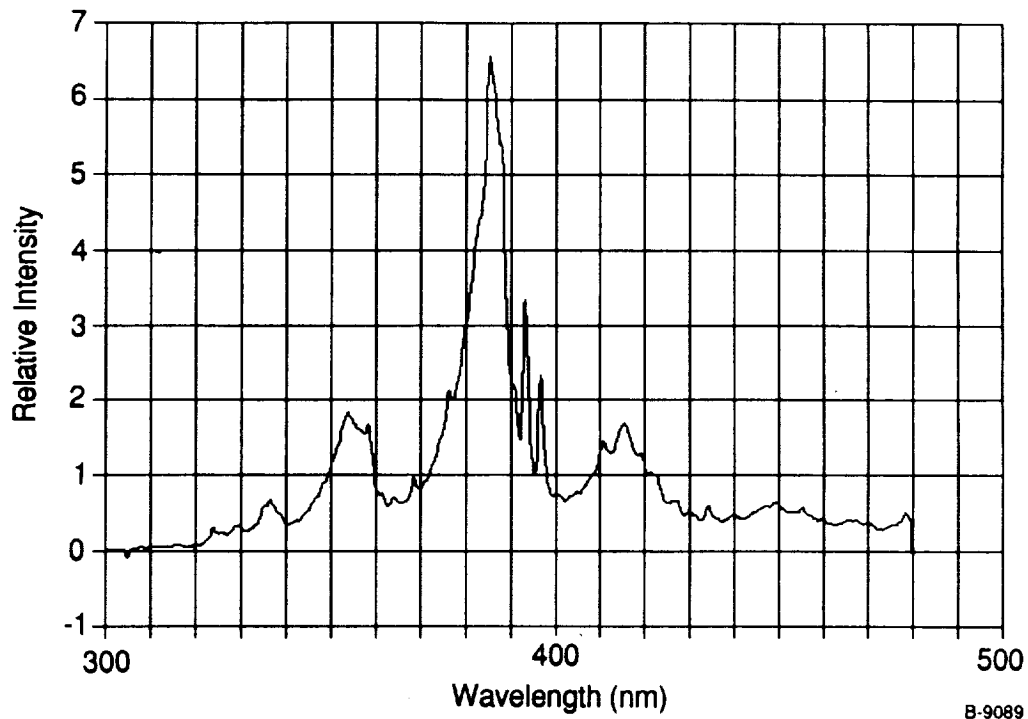


Figure C-15. Non-Equilibrium N_2 , $P_1 = 0.1$ torr, $U_s = 12.1$ km/s $1 \mu s$ gate, $\Delta\lambda = 1.25$ nm.

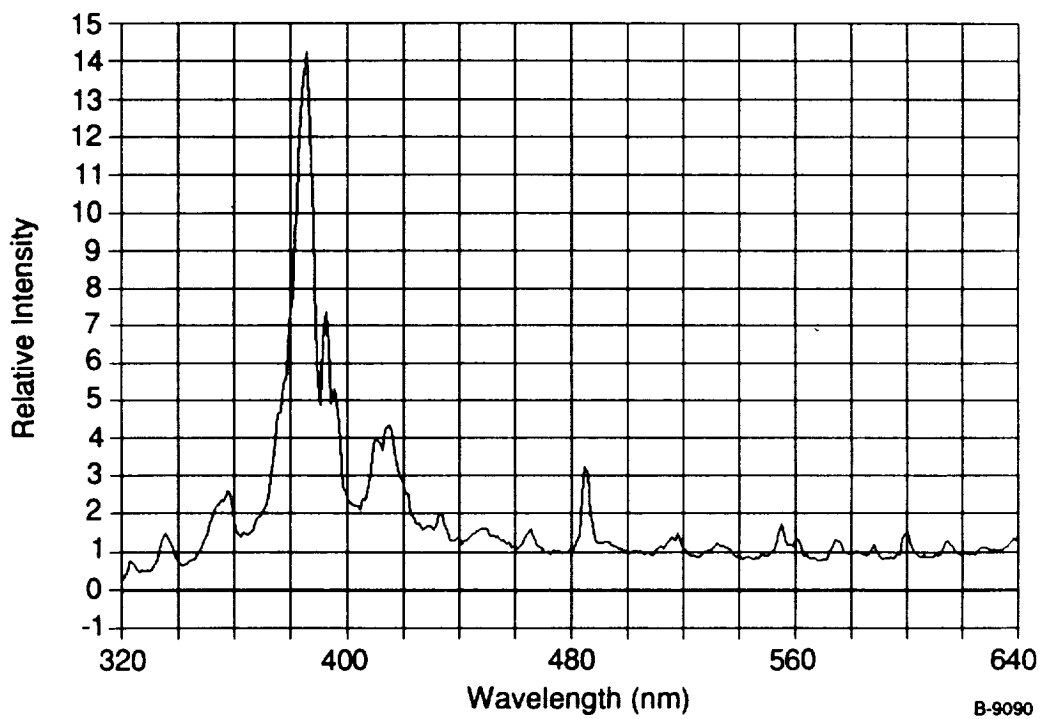


Figure C-16. Equilibrium, N_2 , $P_1 = 0.1$ torr, $U_2 = 12.1$ km/s, $3.35 \mu s$ gate, $\Delta\lambda = 2.5$ nm.